

ANALYTICAL AND NUMERICAL STUDIES OF THE EFFECT OF SHAPE ON
MICROSWIMMER PROPULSION

A THESIS SUBMITTED TO THE GRADUATE DIVISION OF THE
UNIVERSITY OF HAWAI'I AT MĀNOA IN PARTIAL FULFILLMENT
OF THE REQUIREMENTS FOR THE DEGREE OF

PHD

IN

MECHANICAL ENGINEERING

MARCH 2023

By

Ruben Poehnl

Thesis Committee:

Prof. William E. Usual, Chairperson

Prof. John S. Allen

Prof. Monique Chyba

Prof. Sangwoo Shin

Prof. Daisuke Takagi

Keywords: Active matter, active colloids, squirmer, self-phoretic swimmer,
self-diffusiophoretic colloids

ACKNOWLEDGMENTS

Dr. William Uspal, thank you so much for providing with this great opportunity. You gave me a great balance of guidance, to move my research forward, and freedom, to pursue my own ideas. You always had the time to answer questions. Thank you. I also want to thank my committee members, Professors Allen, Chyba, Shin and Takagi, for your help and time in supporting me. Rumen and Viviana, I had a great time working alongside you and always enjoyed our group lunches and discussions. I want to thank the American Chemical Society Petroleum Research Fund for supporting my research. And finally, a big thank you to my family. Without your constant support and love over my whole life I would have never gotten here.

ABSTRACT

The shape of an active colloid has an enormous effect on the motion of the particle and allows for significantly more variation in its design and application. In this thesis, the dynamics of both convex (spheroidal) and concave (helical and toroidal) particles are investigated with analytical and numerical methods. Starting with an individual particle, it is shown that breaking symmetries of the particle shape can enlarge the possibilities for particle motion, both for self-diffusiophoretic microswimmers and within the more general “squirmers model”. These results are then extended to include pair interactions. For interacting spheroids, two types of stable pair configurations can exist: co-moving “head-to-tail” and stationary “head-to-head” pairs. We also consider the interaction of a torus and sphere, with a view towards designing “lock-and-key” interactions.

TABLE OF CONTENTS

Acknowledgments	iii
Abstract	iv
List of Tables	vii
List of Figures	viii
1 Introduction	1
2 Theoretical background	4
2.1 Navier-Stokes equation	4
2.1.1 Reynolds number	4
2.2 Stokes equation	5
2.3 Laplace equation	6
2.4 Self-phoretic particles	6
2.5 Squirmer model	8
2.6 Lorentz reciprocal theorem	8
2.7 Boundary element method	9
2.8 Stresslet	10
2.9 Stokes stream function	11
3 Published work	13
4 Phoretic self-propulsion of helical active particles	14
4.1 Abstract	14
4.2 Introduction	14
4.3 Theory	16
4.3.1 Particle geometry	16
4.3.2 Physical model and governing equations	18
4.3.3 Specification of catalytic activity and surface chemistry	20
4.3.4 Three-dimensional trajectories	21
4.3.5 Numerical method for solution of PDEs	21
4.4 Results	24
4.4.1 Hydrodynamic resistance tensor	24
4.4.2 Lengthwise Janus chemically active particle	27
4.4.3 “z-wise” Janus particle	31
4.4.4 “Inside-outside” Janus particle	33
4.4.5 Slender body theory for helix surface concentration	37
4.5 Conclusions	43
5 Constructing micro-chains:	
a study of self-diffusiophoretic torus-sphere interactions	45
5.1 Introduction	45
5.2 Geometry	46
5.3 Self-phoretic torus-sphere pair	47
5.3.1 Pair interaction	49
5.4 Concentration field	51
5.4.1 Toroidal coordinates	51
5.4.2 Method of reflection	52
5.4.3 Solution in toroidal coordinates	54
5.4.4 Spherical solution	54
5.4.5 Coordinate Transformations	55

5.4.6	Results	55
5.4.7	Designing a lock	57
5.5	Conclusion	57
6	Axisymmetric spheroidal squirmers and self-diffusiophoretic particles	61
6.1	Abstract	61
6.2	Introduction	62
6.3	Model	64
6.4	Hydrodynamic flow and velocity of a prolate squirmer	66
6.4.1	Velocity of the squirmer	67
6.4.2	Stokes stream function and hydrodynamic flow	67
6.5	Squirmer and squirming modes	69
6.5.1	Self-phoretic particle	75
6.6	Summary and conclusion	78
6.7	Appendices	79
6.7.1	Oblate spheroids	79
6.7.2	Gegenbauer functions	80
6.7.3	Decoupling of the even- and odd-index modes in the stream function expansion	80
6.7.4	Example of effects of too strong truncations for the case self-phoretic particles	81
6.7.5	Quantitative comparison to BEM	81
7	Shape-induced pairing of spheroidal squirmers	87
7.1	Arrested-motility states in populations of shape-anisotropic active Janus particles [107]	87
7.2	Introduction	89
7.3	Minimal model	90
7.4	Squirmer model	92
7.5	Head-to-head pairing	94
7.6	Head-to-tail pairs	96
7.7	Conclusions	97
7.8	Appendix	98
7.8.1	Minimal model: Linear stability analysis	98
7.8.2	Head-to-head bound state	99
7.8.3	Head-to-tail bound state	100
7.8.4	A no-cargo theorem for head-to-tail bound states.	101
7.8.5	Velocity and stresslet of axisymmetric spheroidal squirmer	101
7.8.6	Separation distance	102
7.8.7	Induced charge electrophoresis	104
7.8.8	Non-axisymmetric squirmer model	104
8	Conclusion	105
	Bibliography	108

LIST OF TABLES

4.1	Boundary conditions for the auxiliary problem (j).	19
4.2	Experimental measurements from [201], rescaled to be dimensionless for comparison with our BEM results in table 4.4.	26
4.3	Numerical calculations from [47], rescaled to be dimensionless for comparison with our BEM results in table 4.4.	26
4.4	Results of BEM numerical calculations for resistance matrix of a helix. Percent error is calculated with respect to the numerical data of [47]	27

LIST OF FIGURES

2.1	Half-covered self-diffusiophoretic prolate. The lines represent the velocity stream lines and the color indicates the magnitude of the flow field.	6
2.2	Characteristic flow fields created by stokeslet (left), stresslet (middle) and rotlet (right) respectively. The figure has been reprinted from [210] with the permission.	11
2.3	Velocity stream lines around (a) a puller and (b) a pusher spheroidal squirmer particle in free space. The system is chosen such that the particle is at rest (co-moving frame).	12
4.1	Schematic illustration of the particle geometry. The particle consists of a solid “tube” with a helical contour and circular cross-section, plus two solid hemispherical endcaps. Here, we label the contour radius R , the helix pitch λ , the tube radius r_0 , the local tangent vector \hat{t}_h , the local surface normal \hat{n}_h , and the local surface binormal \hat{b}_h . For a given point on the helix centerline, the angle ϕ defines a point on the tube surface. In this example, the particle has a “lengthwise Janus” catalytic activity profile.	17
4.2	Close-up of a meshed interface for a lengthwise Janus particle under conditions of numerical convergence. The red points represent catalytically active nodes of the mesh, while the green points represent inert nodes. The area elements of the mesh are colored by interpolation from the surrounding nodes; blue represents inert and yellow represents active.	24
4.3	(a) Schematic illustration of three helices with different values of pitch λ , but identical contour length $\mathcal{L}/L_0 = 57.5$, contour radius $R/L_0 = 2.5$, and filament radius $r_0/L_0 = 0.265$. (b) Variation of R_{33} , the dimensionless drag coefficient for translational motion along the axis, with λ . Black circles were obtained with the boundary element method, and red circles were obtained by the slender body theory described in [126]. (c) Variation of the translational-rotational coupling coefficient R_{63} with λ . Note that $R_{63} = R_{36}$. (d) Variation of R_{66} , the dimensionless rotational drag coefficient for rotation around the helix axis, as a function of λ	25

- 4.4 (a) Concentration with respect to the tangential position s for $\lambda/L_0 = 5$ and other parameters the same as in figure. 4.3. The shaded grey area shows the range of values that were obtained for c for a given s and various circumferential angles ϕ (individual data points are omitted for clarity). The solid curve is a theoretical expression for the circumferentially averaged concentration obtained with slender body theory. The inset shows the definition of the angle ϕ with respect to the local \hat{n}_h at a position s along the centerline, as well as decomposition of the surface concentration gradient $\nabla_s c$ into tangential and circumferential (i.e., in the plane of the helix cross-section at s) components. (b) Three-dimensional plot of the concentration c on the surface of the particle. (c) Variation of concentration c as a function of circumferential angle ϕ for various values of s . The dashed line indicates $\phi = -\pi/2$. (d) Schematic illustration of the modification of the slender body theory body to obtain the circumferential variation of concentration around the cross-section at s . To obtain the solid curves in (c), it is assumed that the local concentration gradient created by the rest of the particle induces a dipolar variation of concentration on the filament surface with respect to ϕ . In (c), the values of s are as follows: black circles, $s = -0.95$; blue circles, $s = -0.65$; red circles, $s = -0.15$; magenta diamonds, $s = -0.02$; blue diamonds, $s = 0$; magenta crosses, $s = 0.05$; black crosses, $s = 0.15$; red crosses, $s = 0.35$; blue crosses, $s = 0.65$; green crosses, $s = 0.85$ 28
- 4.5 (a) Components of the translational velocity U of a lengthwise Janus particle as a function of pitch λ and parameters r , \mathcal{L} , and R the same as in figure 4.3. In the main figure, the dashed line shows the value of U_z for a spheroidal particle with major axis diameter \mathcal{L} and minor axis diameter $2r$, as determined from [99]. The green curve shows a stretched exponential fit to U_z . In the inset, the dashed lines indicate values of λ for which the number of turns is a half-integer. (b) Components of the angular velocity Ω of a lengthwise Janus particle as a function of pitch λ and other parameters the same as in figure 4.3. The inset shows the peak in Ω_z . (c) The contributions of circumferential and tangential concentration gradients to U_z as a function of λ . (d) The contributions of circumferential and tangential concentration gradients to Ω_z as a function of λ 29
- 4.6 Streamlines (obtained in the stationary frame) of flow in the vicinity of a helix with (a) large pitch ($\lambda/L_0 = 60$) and (b) small pitch ($\lambda/L_0 = 5$). 31
- 4.7 (a) Off-diagonal entries of the third row of the mobility tensor M as a function of pitch λ , and other parameters as given in Fig. 4.3. (b) Mobility tensor component M_{33} as a function of pitch λ . Note the difference in scale from (a); the diagonal entry dominates the third row of M . (c) Translational velocity component along the helix axis U_z for a lengthwise Janus activity profile as a function of pitch (all other parameters are the same as in Fig. 4.5). The full calculation that takes into account all components of M and the right-hand side vector b shows good agreement with an approximate solution obtained as $b_3/80$, where $1/80$ is chosen as a characteristic value of the “flat” part of the curve in (b). (d) Components of the right-hand side vector b as a function of pitch λ for the lengthwise Janus particle. 32

4.8	(a) Dimensionless catalytic activity $j(x_s)$ on the surface of a z-wise Janus particle with $\lambda/L_0 = 5$ and parameters r , \mathcal{L} , and R the same as in figure 4.3. (b) Three-dimensional plot of the concentration c on the surface of the particle. (c) Concentration with respect to the tangential position s . The shaded grey area shows the range of values that were obtained for c for a given s and various circumferential angles ϕ (not shown). The solid curve is a theoretical expression for the circumferentially averaged concentration obtained with slender body theory.	33
4.9	(a) Components of the translational velocity U of a z-wise Janus particle as a function of pitch λ , with parameters r , \mathcal{L} , and R the same as in figure 4.3. (b) Components of the angular velocity Ω . (c) The z-component U_z of the particle translational velocity as a function of pitch, as well as the contributions of circumferential and tangential concentration gradients to U_z . (d) The z-component Ω_z of the particle angular velocity as a function of pitch, as well as the contributions of circumferential and tangential concentration gradients.	34
4.10	(a) Concentration with respect to the tangential position s for an “inside-out” Janus helix. The shaded grey area shows the range of values that were obtained for c for a given s and various circumferential angles ϕ (not shown), and the blue line shows the mean value as a function of s . The solid curve is a theoretical expression for the circumferentially averaged concentration obtained with slender body theory. (b) Variation of concentration c as a function of circumferential angle ϕ for various values of s . The values of s are as follows: blue circles, $s = -0.85$; blue crosses, $s = 0.85$; red circles, $s = -0.65$; red crosses, $s = 0.65$; green circles, $s = -0.35$; green crosses, $s = 0.35$; black diamonds, $s = 0$	34
4.11	(a) Three-dimensional plot of the concentration c on the surface of the “inside-outside” Janus helix. (b) Components of the translational velocity U as a function of the number of turns N and pitch $\lambda/L_0 = 5$, contour radius $R/L_0 = 2.5$, and filament radius $r_0/L_0 = 0.265$. (c) Components of the and angular velocity Ω as a function of the number of turns N	36
5.1	Illustration of the particle geometries. As indicated by the colors both particles can be self-diffusiophoretic, but the catalyst distribution is not limited to the shown case. Here the red and white areas indicate chemically active regions and the black and blue surfaces are inert.	46
5.2	Schematic depiction of the torus-sphere system. In this example both particles are half covered ($\chi_{s,t} = 0$) and separated by a distance d . The sphere has radius R , and the torus has tube radius a and tube centerline radius b . The frame is co-moving with the torus.	48
5.3	(a) Variation of the relative velocity U_{rel} between a half covered self-diffusiophoretic sphere $R = 0.3$ and torus $a = 0.5$ with the separation distance d . (b) Schematic illustration of the four possible configurations the system can be in. (c) Torus velocity U_t as a function of d . (d) Sphere velocity as it changes with d . All results were obtained with the boundary element method and the lines are only a guide to the eye.	51

5.4	Comparison of the relative velocity U_{rel} between the full model and a purely hydrodynamic model (see 5.3.1). Both particles are half covered and have $R = 0.3$ and $a = 0.5$ respectively. All results were obtained with the boundary element method and the lines are only a guide to the eye.	52
5.5	Illustration of Cartesian (x, z) , spherical (r, Θ) and toroidal (ξ, η) coordinate system. The sphere and torus surface, as well as the toroidal basis vectors, are also depicted.	52
5.6	Concentration profiles on the surface of a half covered torus ($a = 0.5$) as a function of the angle η . The torus is at a distance of $d = -5$ (a) and $d = 0$ (b) from a half covered sphere ($R = 0.3$). The line indicates the analytic prediction (see 5.4.2) and the points are calculated with the boundary element method	57
5.7	Concentration profiles on the surface of a half covered sphere ($R = 0.3$) as it changes with the angle Θ . The sphere is at a distance of $d = -5$ (a), $d = 5$ (b), $d = -2$ (c), $d = 2$ (d), $d = -0.5$ (e), $d = 0.5$ (f), $d = -0.1$ (g) and $d = 0.1$ (h) from a half covered torus ($R = 0.5$). The line indicates the analytic prediction (see 5.4.2) and the points are calculated with the boundary element method.	59
5.8	The relative velocity U_{rel} between a self-diffusiophoretic spheres ($R = 0.1$) and a torus ($a = 0.1$) fully covered by a catalyst as a function of their separation distance d . In (a) the sphere is half covered ($\chi_s = 0$) and in (b) it is less then half covered ($\chi = -0.2$). All results were obtained with the boundary element method and the lines are only a guide to the eye.	60
6.1	(a) Two-dimensional (2d) cut of a prolate spheroidal particle with semi-major axis b_z and semi-minor axis b_x ; also shown are the x and z axes of the co-moving system of coordinates and the unit vectors e_τ and e_ζ of the prolate spheroidal coordinate system; (b) 2d cut of a chemically-active self-phoretic particle; the chemically active part is the cap-like region shown in white, while the rest of the surface (black) is chemically inert. The quantity χ ("coverage") denotes a certain measure for the extent of the active part (see Sec. 6.5.1 in the main text).	65
6.2	The absolute value $ U_n $ (Eq. (6.21)) of the contribution of the slip modes $n = 1, 3, 5, 7$ to the velocity of a prolate squirmer for aspect ratios $r_e = 0.3, 0.5, 0.7, 0.9$. The lines represent only a guide to the eye.	71
6.3	The absolute value $ S_n $ (Eq. (6.22)) of the contribution of the slip modes $n = 1, 3, 5, 7$ to the stresslet of a prolate squirmer for aspect ratios $r_e = 0.3, 0.5, 0.7, 0.9$. The lines represent only a guide to the eye. This figure has been updated compared to the published version.	72
6.4	The flow field (streamlines and velocity magnitude (color coded background)) induced by a prolate squirmer with $B_n = \delta_{n,n_0}$ for (top to bottom) $n_0 = 1, 2, 3, 4$ and aspect ratio $r_e = 0.3$ (left column) and $r_e = 0.5$ (right column), respectively. The results are shown in the laboratory frame and are obtained by using the series representation of the stream function (see the main text). The arrows on the particles indicate the directions of their motion.	74
6.5	Velocity components v_τ and v_ζ on the iso-surfaces $\tau = 1.1\tau_0$ and $\tau = 2\tau_0$ near a prolate squirmer with $B_n = \delta_{n,1}$	75
6.6	Velocity components v_τ and v_ζ on the iso-surfaces $\tau = 1.1\tau_0$ and $\tau = 2\tau_0$ near a prolate squirmer with $B_n = \delta_{n,3}$	75

6.7	The absolute value $ U_n $ of the contribution of the slip modes $n = 1, 3, 5, 7$ to the velocity of an oblate squirmer for aspect ratios $r_e^{-1} = 0.3, 0.5, 0.7, 0.9$. The lines represent only a guide to the eye. This figure has been updated compared to the published version.	76
6.8	The absolute value $ S_n $ of the contribution of the slip modes $n = 1, 3, 5, 7$ to the stresslet of an oblate squirmer for aspect ratios $r_e^{-1} = 0.3, 0.5, 0.7, 0.9$. The lines represent only a guide to the eye. This figure has been updated compared to the published version.	76
6.9	The flow field (streamlines and velocity magnitude (color coded background)) induced by an oblate squirmer with $B_n = \delta_{n,n_0}$ for (top to bottom) $n_0 = 1, 2, 3, 4$ and aspect ratio $r_e^{-1} = 0.3$ (left column) and $r_e^{-1} = 0.5$ (right column), respectively. The results are shown in the laboratory frame and are obtained by using the mapping discussed in the main text and the flows of the corresponding prolate squirmers shown in Fig. 6.4. The arrows on the particles indicate the directions of their motion.	77
6.10	The flow field (streamlines and velocity magnitude (color coded background)) induced by a chemically active prolate particle moving by self-phoresis, calculated either analytically via the stream function (left column) or numerically, i.e., by directly solving the corresponding Laplace and Stokes equations using the BEM [198] (right). The results shown correspond to the cases of half ($\chi = 0$, top two rows) and less than half ($\chi = -0.3$, bottom two rows) coverage, and two values, $r_e = 0.3$ and $r_e = 0.5$, of the aspect ratio, respectively. The arrows on the particles indicate the directions of their motion. The red area depicts the chemically active region. The motion of the particle and the direction of the flow corresponds to the choice $b < 0$; the characteristic velocity U_0 is defined as in Ref. [196]	82
6.11	The flow field around a self-phoretic particle ($\chi = 0.8$, $r_e = 0.9$) when keeping the first (a) two and (b) eight terms (effective squirmer modes) in the series expansion of the stream function. The red area depicts the chemically active region.	83
6.12	The flow field around a prolate squirmer with $r_e = 0.3$; in the left column only the first slip mode is active, and on the right column only the second slip mode is active. In both cases the analytical results are shown in the top row, the numerical results (BEM [198]) in the middle row, and the relative error between the two (Eq. (6.31)) in the bottom row.	84
6.13	The flow field around a prolate squirmer with $r_e = 0.3$; in the left column only the third slip mode is active, and on the right column only the fourth slip mode is active. In both cases the analytical results are shown in the top row, the numerical results (BEM [198]) in the middle row, and the relative error between the two (Eq. (6.31)) in the bottom row.	85
6.14	The flow field around half covered ($\chi = 0$) self-phoretic particles with aspect ratio $r_e = 0.3$ (left) and $r_e = 0.5$ (right). In both cases the analytical results are shown in the top row, the numerical results (BEM [198]) in the middle row, and the relative error between the two (Eq. (6.31)) in the bottom row. The red area depicts the chemically active region.	86
7.1	Microscopy image showing pair formation in systems of disk-shaped active Janus colloids. Pairs are identified by red circles. Scale bar, $40\mu\text{m}$. The figure has been reprinted from [107].	87

7.2	Steady separation of two particles as a function of frequency. Closed symbols show the experimental results; open symbols show the results of numerical calculations. The figure has been reprinted from [107].	88
7.3	(a) Side view of the flow field in the vicinity of a Janus discoid in the DC limit ($f \rightarrow 0$). The discoid center is located at $(0, 0, 1.06R)$, and the flow field is shown in the symmetry plane $y = 0$. A solid wall is located at $z = 0$. The metal and insulating “faces” of the particle are shown in black and grey, respectively. The color field encodes the magnitude of the fluid velocity, $ u(x) /U_0$. A large vortex is located behind the particle and near the wall. Streamlines start and end on the front and rear of the particle, respectively, reflecting the fact the particle is moving to the right. (b) Experimental data showing the probability distribution (left) and trajectories (right) of tracer particles in the vicinity of a Janus particle. Tracers in the rear vortex move with the particle as they execute recirculating motions in the vortex. The figure has been reprinted from [107].	88
7.4	Schematic illustration of two spheroids, including their swimming directions $\hat{d}^{(1)}$ and $\hat{d}^{(2)}$, angles ϕ_1 and ϕ_2 and separation vector r	92
7.5	Assigned slip velocities for an oblate squirmer with aspect ration $r_e = 5$. (a) and (b) are axisymmetric and (c) has a purely non-axisymmetric slip velocity following the definition in Eq. 7.7. (a) Shows a motile colloid with squirming mode amplitudes $B_n = \delta_{n,1}$ and $\tilde{B} = 0$. (b) and (c) are stationary particles with amplitudes (b) $B_n = \delta_{n,2}$, $\tilde{B} = 0$, and (c) $B_n = 0$, $\tilde{B} = 1$	93
7.6	(a) Phase map for head-to-head pairs with fixed squirming modes $B_1 = 0.1$ and $B_2 = -1$ and varying δ and Γ . The background colors show the stability predicted by our model and the symbols represent numerical calculations done with BEM. The red symbols indicate particle pairs without a stable head-to-head separation. The crosses represent data including the non-axisymmetric squirming mode (Eq. 7.7), whereas the calculations using the ICEP effective squirmer model (see 7.8.7) are indicated with circles. The latter data is also connected by a dashed line as a guide to the eye. (b) Top down view of a sample trajectory for $\tilde{B} = 1.6833$ and $\Gamma = -0.8349$. The particles are initial separated by $x_{\text{initial}} = 2$ and $y_{\text{initial}} = 55$	95
7.7	(a) Phase space for head-to-tail pairs with fixed geometric parameter $\Gamma_2 = -0.8$ and velocity ratio $U = 0.8$ and varying S and Γ_1 . The background colors show the stability predicted by our model and the symbols represent numerical calculations done with BEM. The red symbols indicate particle pairs without a stable head-to-tail separation. (b) Top-down view of a head-to-tail pair. The coordinates, separation distances x_2 and y_2 , aspect ratios $r_e^{(\alpha)}$ and swimming directions $\hat{d}^{(\alpha)}$ are also shown. (c)-(g) Top-down view of a sample trajectory for $S = 2.2$ and $\Gamma_1 = -0.7$ in five steps. This pair is represented by a blue cross in the phase space. The particles are initial separated by $x_{2,\text{initial}} = 3$ and $y_{2,\text{initial}} = 20$	96

7.8	(a) The absolute value $ U $ of the contribution of the slip modes $n = 1, 3, 5, 7$ to the velocity of a prolate squirmer for aspect ratios $r_e = 0.3, 0.5, 0.7, 0.9$. (b) The absolute value $ S $ of the contribution of the slip modes $n = 1, 3, 5, 7$ to the stresslet of a prolate squirmer for aspect ratios $r_e = 0.3, 0.5, 0.7, 0.9$. (c) The absolute value $ U $ of the contribution of the slip modes $n = 1, 3, 5, 7$ to the velocity of an oblate squirmer for aspect ratios $r_e^{-1} = 0.3, 0.5, 0.7, 0.9$. (d) The absolute value $ S $ of the contribution of the slip modes $n = 1, 3, 5, 7$ to the stresslet of an oblate squirmer for aspect ratios $r_e^{-1} = 0.3, 0.5, 0.7, 0.9$. The lines represent only a guide to the eye.	102
7.9	(a) Comparison between the analytically predicted and the numerically calculated velocity $ U_s $ over a range of aspect ratios r_e . For these calculations, only B_1 is non zero. (b) Comparison between the analytic predicted and the numerically calculated stresslet magnitude $ S_0 $ over a range of aspect ratios r_e . For these calculations only B_2 is non zero.	103
7.10	Comparison between the predicted and the calculated (BEM) separation distance for head- to-tail pairs. The velocities $U_s^{(2)} = 0.2$ and $U_s^{(1)} = 0.25$ are fixed in all cases. We show three different geometries (a) $r_e^{(1)} = 1.1055$ and $r_e^{(2)} = 3$, (b) $r_e^{(1)} = 1.1055$ and $r_e^{(2)} = 1.1055$, (c) $r_e^{(1)} = 0.5774$ and $r_e^{(2)} = 0.5774$	103
7.11	The S_{dd} , S_{cc} and S_{ee} contributions for a squirmer with constant asymmetric mode $\tilde{B} = 1$ for changing aspect ratio r_e . The lines represent only a guide to the eye.	104

CHAPTER 1

INTRODUCTION

Smaller. Faster. Better. Miniaturization is an integral part of the maturation process of any technology. Computers and electronics in general are the most famous and successful example. While the first computers could fill a whole building, a modern smartphone with a processing power many magnitudes higher can fit in our pocket. In his 1959 lecture “There’s Plenty of Room at the Bottom: An Invitation to Enter a New Field of Physics” Richard Feynman envisioned a future in which humans are able to manipulate matter at the nano and micro scales. Many aspects of his vision have come true, but we still do not “swallow our doctor,” as he put it. The idea of using microscale robots to perform surgeries, remove blood clots, or deliver drugs directly to cancerous growth is still motivating scientists all around the world and arouses interest in the general public, such as in the New York Times [3]. Why have the problems not been solved in the sixty years since then, one might ask? First of all, the research into active matter, and microswimmers in particular, unfortunately did not start in earnest until decades later. Secondly, mobility in fluids at low Reynolds number, which includes motion in water at the microscale, is drastically different compared to our everyday experiences. Milk accidentally added to a low Reynolds number coffee could get “unstirred” again, but even Michael Phelps would barely swim forward using the crawl or backstroke.

In order to overcome these hurdles, a natural first step is to investigate nature. Organisms exist at all length scales and have evolved propulsion mechanisms adapted to their environments [86, 180]. Understanding why and how these work is required in order to replicate them- or, at least, can provide the inspiration necessary to mimic them. Beyond that, a better understanding of nature (for example bacteria), is a worthwhile goal on its own and will also have benefits for new medical treatments.

Many microorganisms propel themselves with the help of flagella, thread-like appendages of varying size. Often these are small but numerous, and cover the entire body, similar to a carpet. When the cilia beat in a coordinated manner, the surrounding fluid gets pushed in such a way that the organism moves forward. While it is not feasible to recreate the cilia for artificial microswimmers, their effect, i.e. the resultant flows, can be mimicked. One such interfacially-driven system are self-diffusiophoretic colloids. Being only partially covered by a catalyst, they produce an inhomogeneous concentration field in their surroundings. Molecular-scale interactions with the product molecules can create flows similar to flows driven by the beating of cilia and propel the particle forward. This mechanism is described in greater detail in chapter 2.4.

Another aspect immediately obvious when studying biological microswimmers is the wide range of shapes. Spheres, due to their relative ease of manufacturing and mathematical elegance, are a favorite both for experimental and theoretical studies. However, if nature holds true as an indicator, they are not the optimal shape in most cases. Instead, elongated, constricted and even concave, i.e. *E. coli*, shapes are much more common [21, 101, 133, 224, 263].

Answering the question, why this is the case and how more complex geometries can be used for real world applications is one of the main goals of this work.

It is safe to assume that most of the envisioned applications will not be achieved with only a single type of microswimmer. While freeing a blocked artery might be similar to removing micro plastics from corrals [20], those tasks are vastly different from controlling a chemical spill with a lab-on-a-chip device [74]. Similarly, certain so-called micromachines have already been proposed and prototypes designed, but a microdrill [78] will never look similar to a microgear [11]. In addition, they are often envisioned to be composed of multiple, self-assembling parts.

Beyond the shape, the second main focus in this thesis are the interactions between microswimmers. A single particle is small and will not have enough effect to achieve the goal. For example, a single microswimmer will not be able to deliver enough drugs to stop the growth of a tumor. It is thus, imperative to understand how individual particles react to each other. Only this will allow us to design particles that can function as the building blocks of a more complex system. Over the last decade, this has lead to a significant interest in understanding the collective behavior of artificial and biological microswimmers. The main focus to date has been on two classes of clustering phenomena.

The first class is called motility-induced phase separation (MIPS) and relies on a self-trapping mechanism induced by the steric interaction between particles [38, 189]. Two microswimmers can not swim through each other, and instead become stuck when colliding. The particles only escape, if one rotates enough to slide past the other. However, if a third swimmer crashes into the pair beforehand, a cluster begins to grow. While aggregation is also known for passive colloids, microswimmer do not need an attractive particle-particle interaction in order to form such a cluster. Instead, above a characteristic particle density and swimming speed, a phase separation occurs. In the “gas” phase the colloids are far apart and continue to move freely. In the second phase, the clusters, the particles are in direct contact and severely limited in their mobility. There is no inherent alignment between particles in such clusters. Overall, equilibrium between a dense cluster phase and a tenuous “gas” phase is established by a kinetic balance between incoming and outgoing fluxes of particles at the interface between the phases.

The second kind of clusters, on the other hand, form by ordering. A velocity-aligning interaction between the particles enables the formation of these co-moving clusters. These interactions are non-steric and typically hydrodynamic, electric, or magnetic. Fascinating phenomena such as swarming [110, 113], consistent unidirectional movement [32], vortices [31, 89, 128] and superfluidity [147] have been observed under these conditions. For artificial microswimmers, Quincke rollers [261], magnetic rollers [113], and electrokinetic particles [255] are commonly used. All three of these systems have two limitations in common: they are restricted to a confined space and need an external field. For many applications, these limitations are detrimental, if not prohibitive. For instance, a three dimensional micromachine could not assemble and a chemical spill needs to be controlled wherever it appears.

In a recent study, hydrodynamic interaction between two active colloids are shown to create

clusters [107]. Pairs of colloidal disks aligned in a head-to-head configuration, but crucially their direction is not influenced by the external field and they are well separated. This indicates the possibility to design artificial microswimmers, that have neither severe limitations to their mobility (type 1), nor the restrictions associated with clusters of the second type. Such systems could open many possibilities in the future and investigating them in the context of complex shapes is the second part of this thesis.

After a brief introduction to the physical laws and equations underlying the dynamics of self-phoretic particles, four novel contributions to the field are presented. All four use a combination of analytical predictions and numerical calculations to predict and understand the behavior of active particles with non-spherical shapes.

In the first half (Chapters 1 and 2), self-diffusiophoretic colloids are discussed. These particles achieve self-propulsion by decomposing a “fuel” in the surrounding fluid (see section 2.4). Due to their relative ease of production and not needing an external field (i.e. electrical or magnetic field), self-diffusiophoretic colloids are commonly used in experimental studies. These chapters focus on self-diffusiophoretic colloids with a concave geometry. Helical shapes (Chapter 1) create circumferential, in addition to the well-known tangential, variations in the concentration field, and enable the colloid to swim with many more degrees of freedom. Using the simplest catalytic distribution, covering the bottom half of the particle, a sphere can only swim forward or backwards. A helix, on the other hand, can swim in all three directions and can rotate around all three axes. We investigate how these six velocity components can be controlled through tailoring the surface chemistry and shape of the helical particle.

In Chapter 2 the pair interaction between a self-diffusiophoretic torus and sphere are investigated. These pairs are shown to form stable, co-moving pairs, an important stepping stone for many applications relying on alignment. In addition, the torus can be designed to be stationary and impassible for specific spheres. The exclusion criterion is the sphere’s self-propulsion speed, meaning the torus functions as a speed gate for spheres.

Instead of self-diffusiophoresis, Chapters 3 and 4 discuss the more general squirmer model (see section 2.5) for spheroidal geometries. In Chapter 3 the traditional (spherical) squirmer model is extended to spheroidal shapes. This does not only increase the applicability of the model, but also shows an inherent advantage spheroidal shapes have over spherical ones. Many patterns of surface actuation which fail to propel spherical microswimmers can do so for spheroidal microswimmers.

Finally, in Chapter 4, this extended model is used to understand the formation of only recently discovered stationary microswimmer pairs [107]. A full stability analysis is performed for these “head-to-head” pairs. In addition, the existence of stable, co-moving “head-to-tail” pairs is predicted.

CHAPTER 2

THEORETICAL BACKGROUND

In this chapter, we review the basic theory of low Reynolds number flows, molecular diffusion, and self-phoresis. We also briefly discuss our chosen numerical method, the boundary element method. Detailed treatments of creeping flow are provided by Lauga [137], Brenner [93], and Kim and Karilla [125]. The boundary element method is developed in detail by Pozrikidis [199].

2.1 Navier-Stokes equation

The Navier-Stokes equation

$$\rho \left(\frac{\partial \mathbf{v}}{\partial t}(\mathbf{r}, t) + (\mathbf{v}(\mathbf{r}, t) \cdot \nabla) \mathbf{v}(\mathbf{r}, t) \right) = -\nabla p(\mathbf{r}, t) + \mu \nabla^2 \mathbf{v}(\mathbf{r}, t) + \mathbf{f}(\mathbf{r}, t) \quad (2.1)$$

is the fundamental equation of fluid dynamics and relates the flow velocity \mathbf{v} of a fluid, to its dynamic viscosity μ , mass density ρ , pressure p , and external body force density \mathbf{f} . It can be derived directly from Newton's famous second law $\mathbf{F} = \frac{d}{dt}(m \cdot \mathbf{v})$ connecting an applied force \mathbf{F} to the changes in mass m and velocity \mathbf{v} . In order to solve the Navier-Stokes equation, incompressibility

$$\nabla \cdot \mathbf{v} = 0 \quad (2.2)$$

will be assumed, in addition to the boundary conditions.

2.1.1 Reynolds number

Reynolds number $\text{Re} = \frac{UL\rho}{\mu}$ is a dimensionless number often used in fluid dynamics to distinguish and classify fluid flows, ranging from air around a plane $\text{Re} \gg 1,000,000$ to lava flowing out of a volcano $\text{Re} \leq 2,000$ [44]. It is calculated using the characteristic velocity $|\mathbf{v}(\mathbf{r}, t)| \approx U$ and length L of the system in question and represents the ratio of inertial to viscous forces as

$$\text{Re} = \frac{\text{inertial forces}}{\text{viscous forces}} = \frac{UL\rho}{\mu} = \frac{1\mu\text{m} \cdot \text{s}^{-1} \cdot 10\mu\text{m} \cdot 10^3\text{kg} \cdot \text{m}^{-3}}{10^{-3}\text{Pa} \cdot \text{s}} = 10^{-5} \ll 1. \quad (2.3)$$

For a typical microswimmer Re is very small. Microswimmers are commonly $L \approx 10\mu\text{m}$ long and swim at speeds of about $U \approx 1\mu\text{m} \cdot \text{s}^{-1}$ in water ($\rho = 10^3\text{kg} \cdot \text{m}^{-3}$; $\mu = 10^{-3}\text{Pa} \cdot \text{s}$). It follows that for microswimmers, viscous forces dominate inertial forces. The Navier-Stokes

equation (2.1) expressed in terms of dimensionless quantities t' , v' and r' reads

$$\begin{aligned}\frac{\rho U^2}{L} \left(\frac{\partial \mathbf{v}'}{\partial t'}(\mathbf{r}', t') + (\mathbf{v}'(\mathbf{r}', t') \cdot \nabla') \mathbf{v}'(\mathbf{r}', t') \right) &= \frac{-1}{L} \nabla' p(\mathbf{r}', t') + \frac{\mu U}{L^2} \nabla'^2 \mathbf{v}'(\mathbf{r}', t') + \mathbf{f}(\mathbf{r}', t') \\ \frac{UL}{\mu/\rho} \left(\frac{\partial \mathbf{v}'}{\partial t'}(\mathbf{r}', t') + (\mathbf{v}'(\mathbf{r}', t') \cdot \nabla') \mathbf{v}'(\mathbf{r}', t') \right) &= \frac{-L}{\mu U} \nabla' p(\mathbf{r}', t') + \nabla'^2 \mathbf{v}'(\mathbf{r}', t') + \frac{L^2}{\mu U} \mathbf{f}(\mathbf{r}', t') \\ \text{Re} \left(\frac{\partial \mathbf{v}'}{\partial t'}(\mathbf{r}', t') + (\mathbf{v}'(\mathbf{r}', t') \cdot \nabla') \mathbf{v}'(\mathbf{r}', t') \right) &= -\nabla' p'(\mathbf{r}', t') + \nabla'^2 \mathbf{v}'(\mathbf{r}', t') + \mathbf{f}'(\mathbf{r}', t'), \quad (2.4)\end{aligned}$$

when introducing the characteristic timescale $T = \frac{L}{U}$ and dimensionless pressure $p' = \frac{L}{\mu U} p$.

2.2 Stokes equation

Reynolds number being very small ($\text{Re} \ll 1$) reduces Eq. (2.1) to the Stokes equation

$$0 = -\nabla p(\mathbf{x}) + \mu \nabla^2 \mathbf{v}(\mathbf{x}) + \mathbf{f}(\mathbf{x}) \quad (2.5)$$

by neglecting the left hand side. Stokes equation has several mathematical properties which describe remarkable real world behavior. The equation has no explicit time dependence, which makes every process automatically reversible. Famously, G.I. Taylor showcased this in a video for the National Committee for Fluid Mechanics Films by mixing and demixing a drop of paint in glycerin [2]. This can be reproduced by anybody by slowly stirring the glycerin a set number of turns one way to mix and then rotating it in the opposite direction the exact same number of turns to demix. Another immediate result of reversibility is the so-called “no scallop theorem” [200]. It states: “No time symmetric, periodic motion can produce a net displacement for a microswimmer”. For a scallop in the low Reynolds number, or creeping flow, regime, this means how ever much it moves forward when opening its shell, it will move backwards the exact same amount when closing it. The speed at which the two separate motions are done has no effect on the final outcome.

The solution to a Stokes problem can be time dependent if either the boundary conditions or the applied forces f are time dependent. However, the solution will be instantaneous, meaning the influence of these changes will spread immediately throughout the entire system. It follows that microswimmers need a continuous propulsion mechanism. As soon as the propulsion is interrupted, the microswimmer will come to a standstill; coasting is impossible. Finally, Eq. (2.5) is linear, a property very useful for analytic solutions. A complex problem can be split up into multiple, geometrically identical auxiliary problems. After solving every auxiliary problem individually, the overall solution can be constructed by simple addition of the individual solutions.

2.3 Laplace equation

The convection-diffusion equation governs the spread and distribution of a chemical concentration field c in a fluid

$$\frac{\partial c}{\partial t} = \nabla \cdot (D \nabla c) - \nabla \cdot (\mathbf{v}c) + S_c. \quad (2.6)$$

Here S_c is a sink, which can be a function of \mathbf{r} and t , and D the diffusion coefficient. Using the incompressibility condition, Eq. (2.6) can be arranged into

$$\frac{\partial c}{\partial t} = \nabla \cdot (D \nabla c) + S_c, \quad (2.7)$$

with the left hand side representing the effect of advection and the right hand side the effect of molecular fluxes. The Péclet number

$$\text{Pe} = \frac{\text{advective transport rate}}{\text{diffusive transport rate}} = UL/D = \frac{1\mu\text{m} \cdot \text{s}^{-1} \cdot 10\mu\text{m}}{4 \cdot 10^{-9}\text{m}^2\text{s}^{-1}} = 2.5 \cdot 10^{-3} \ll 1 \quad (2.8)$$

compares the advective transport rate to the diffusive transport rate. For a typical self-diffusiophoretic microswimmer in free space (see 2.4, $S_c = 0$, $D \approx 4 \cdot 10^{-9}\text{m}^2\text{s}^{-1}$ for O_2) the diffusive transport rate is much higher and Eq. (2.6) reduces to the Laplace equation.

$$\nabla^2 c = 0. \quad (2.9)$$

2.4 Self-phoretic particles

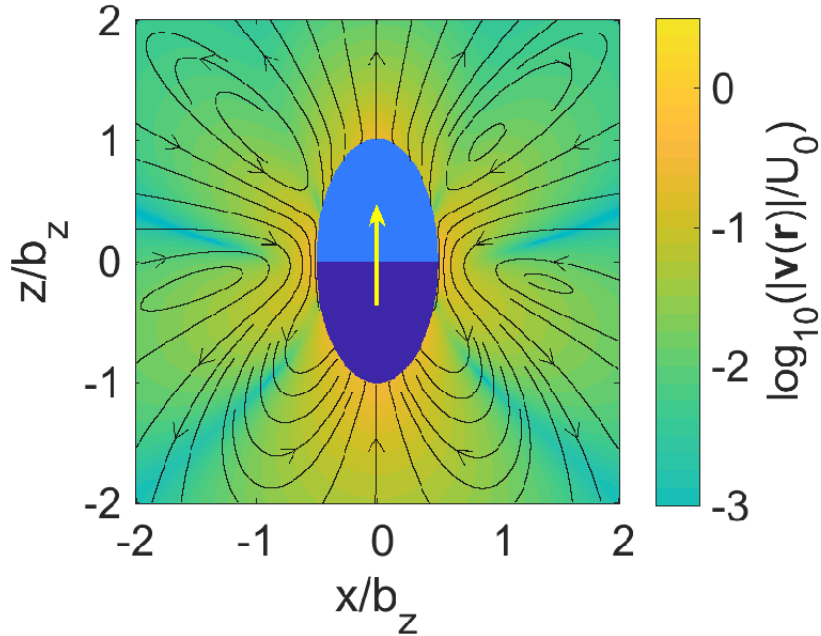


Figure 2.1: Half-covered self-diffusiophoretic prolate. The lines represent the velocity stream lines and the color indicates the magnitude of the flow field.

Self-diffusiophoresis is one propulsion mechanism developed for artificial microswimmers. These colloids propel themselves by harvesting local free energy from a chemical fuel. Due to the size limitations at the microscale ($V \propto R^3$), they can not transport the fuel and instead it needs to be available in the surrounding fluid. Their surface is split into at least two parts with different chemical properties; one part of the particle surface catalyses a decomposition of fuel molecules in the surrounding fluid, while the rest is inert. A common example is platinum covered polystyrene. In an $\text{H}_2\text{O}-\text{H}_2\text{O}_2$ solution the platinum catalyses the decomposition of H_2O_2 into H_2O and O_2 . The product molecules (O_2) are not spread homogeneously along the surface and a concentration gradient is created. The molecules within a molecular-sized distance, δ , of the colloid surface feel either an attraction or repulsion from the particle. This interaction generates a force on the molecules inside the δ region; but the impenetrability of the particle prevents the molecules at the particle boundary from moving normal to it. The forces are instead balanced by a pressure difference, i.e., there is a local hydrostatic equilibrium in the direction normal to the surface similar to the gravity induced pressure increase in water. This local equilibrium, i.e., equilibrium concerning variation of the concentration in the normal direction, can be achieved because the boundary layer is thin ($\delta \ll R$). Whether the interaction is repulsive or attractive does not change the fundamental mechanism, but only its sign.

Since the concentration along the surface changes, so does the pressure and a so-called slip flow emerges [196]. This slip velocity is self-generated and causes the particle to propel itself forward, hence the name self-diffusiophoresis.

For this work only zeroth order reaction kinetics are considered, i.e. the chemical activity does not depend on the product concentration. This assumption is justified if the “fuel” concentration does not diminish notably, i.e. the chemical activity is low and the “fuel” is plentiful in solution.

As stated above, the Péclet number for a typical self-diffusiophoretic colloid is very small. This justifies the neglect of all advection effects on the concentration field and assuming the system to be a quasi-steady instead.

For a colloid in an unbounded fluid, it follows that the concentration field satisfies Laplace’s equation

$$\nabla^2 c = 0 \quad (2.10)$$

with boundary conditions on the particle surface

$$-D[\mathbf{n} \cdot \nabla c] = \kappa j(\mathbf{x}_s) \quad (2.11)$$

and at infinity

$$c(\mathbf{r}) \rightarrow 0 \text{ for } r \rightarrow \infty. \quad (2.12)$$

As mentioned before, the catalytic activity j varies along the particle surface \mathbf{x}_s , κ is the characteristic rate of solute production per unit area, and \mathbf{n} the surface normal pointing into the fluid.

Once the concentration field along the surface is known, the slip velocity can be calculated using the equation

$$\mathbf{v}_s = -b\nabla_{||}c(\mathbf{x}_s) \quad (2.13)$$

as stated by Anderson [7]. The surface mobility b represents the interaction details between the particle surface and the product molecules. For an attractive interaction, b is positive. b is material dependent, and hence can take different values on the inert and catalytic faces. Self-propelled microswimmers are force and torque free. Using this property, their swimming speed \mathbf{U} and $\mathbf{\Omega}$ can be calculated via the Lorentz reciprocal theorem 2.6.

2.5 Squirmer model

The squirmer model was originally invented by Lighthill [145] in 1952 and later corrected and extended by Blake [25]. Its original intent was to model axisymmetric, spherical, ciliated microswimmer by averaging the movement of the flagella in both space and time. This is justified if the flagella beat much faster than the particle moves and are much shorter than the particle body. The flow induced by the envelope of cilia tips is replaced with a constant slip velocity in an infinitesimal surface layer between fluid and particle. Hereto, two approximations are necessary. Firstly, the finite length of the flagella is neglected and their effect is reduced to a single (surface) layer; secondly, since the flagella beat much faster than the particle moves, the induced flow field is averaged over one period. This approach can be extended to any slip driven, self-propelled microswimmer, e.g. self-diffusiophoretic colloids. For a spherical particle the normal v_n and tangential v_s component are developed in terms of the Legendre polynomials P_n and associated Legendre polynomials P_n^1

$$v_n = \sum_n^{\infty} A_n P_n(\cos(\theta)) \quad (2.14)$$

$$v_s = \sum_n^{\infty} B_n \frac{-n(n+1)}{2} P_n^1(\cos(\theta)) \quad (2.15)$$

respectively. The coefficients A_n and B_n are the amplitudes for the individual modes. A_1 and B_1 immediately and solely fix the particle swimming velocity $|\mathbf{U}| = \frac{1}{3}(2B_1 - A_1)$.

2.6 Lorentz reciprocal theorem

Lorentz reciprocal theorem will allow for the calculation of the swimming speed \mathbf{U} and $\mathbf{\Omega}$ of a microswimmer without solving the fluid dynamic problem in the whole fluid. Instead, it connects the velocity \mathbf{v} , and Newtonian stress tensor $\boldsymbol{\sigma}$, on the surfaces of two geometrically identical systems S and S' . The second system, with different boundary conditions, will be conveniently chosen.

Using Einstein notation, the equation

$$\mathbf{v}' \cdot (\nabla \cdot \sigma) = \frac{\partial(v'_j \sigma_{ij})}{\partial x_i} - \sigma_{ij} \frac{\partial v'_j}{\partial x_i} \quad (2.16)$$

can be rewritten assuming incompressibility $\nabla \cdot \mathbf{v}(\mathbf{r}) = 0$ and with the definition of the Newtonian stress tensor

$$\sigma_{ij} = -\delta_{ij}p + \left(\frac{\partial v_i}{\partial x_j} + \frac{\partial v_j}{\partial x_i} \right). \quad (2.17)$$

This leaves

$$\begin{aligned} & \frac{\partial(v'_j \sigma_{ij})}{\partial x_i} - (-\delta_{ij}p + \left(\frac{\partial v_i}{\partial x_j} + \frac{\partial v_j}{\partial x_i} \right)) \frac{\partial v'_j}{\partial x_i} \\ &= \frac{\partial(v'_j \sigma_{ij})}{\partial x_i} - \left(\frac{\partial v_i}{\partial x_j} + \frac{\partial v_j}{\partial x_i} \right) \frac{\partial v'_j}{\partial x_i} = v'_j \frac{\partial \sigma_{ij}}{\partial x_i}, \end{aligned} \quad (2.18)$$

which can be further simplified for Stoke flows $\frac{\partial \sigma_{ij}}{\partial x_i} = 0$ and if there are no external body forces ($\mathbf{f}(\mathbf{r}) = 0$)

$$\frac{\partial(v'_j \sigma_{ij})}{\partial x_i} - \left(\frac{\partial v_i}{\partial x_j} + \frac{\partial v_j}{\partial x_i} \right) \frac{\partial v'_j}{\partial x_i} = 0. \quad (2.19)$$

The primed and the unprimed system are interchangeable. Subtract the respective equations from each other, one obtains the Lorentz reciprocal relation

$$\frac{\partial}{\partial x_i} (v'_j \sigma_{ij} - v_j \sigma'_{ij}) = 0. \quad (2.20)$$

Applying Gauss's theorem reformulates the differential equation in its integral form, also known as Lorentz reciprocal theorem

$$\int_{\partial \Sigma} dS \mathbf{v}' \cdot \sigma \cdot \mathbf{n} = \int_{\partial \Sigma} dS \mathbf{v} \cdot \sigma' \cdot \mathbf{n}. \quad (2.21)$$

Here $\partial \Sigma$ is the boundary of the fluid and \mathbf{n} is its normal.

2.7 Boundary element method

The boundary element method (BEM) [198] is a numerical approach to calculating the velocities of a particle using the Lorentz reciprocal theorem. It can be split up into two steps; first the chemical concentration field on the surface of the particle needs to be determined. This is done by solving the Laplace problem presented in 2.4 numerically. Using its solution the slip velocity $v_{\text{surface}}(\mathbf{r}_P)$ can be calculated. With it the hydrodynamic boundary condition on the particle surface is fixed.

As introduced above, for the Lorentz reciprocal theorem to be usable, a secondary system S' is necessary. BEM actually uses six S'_i , one for each of the particle velocity components.

Each one has a no-slip condition on the particle surface and is driven by an external force, such that the particle velocities are fixed as

$$\begin{aligned}
(\mathbf{U}'_1, \mathbf{\Omega}'_1) &= (U_0 \mathbf{e}_x, 0) \\
(\mathbf{U}'_2, \mathbf{\Omega}'_2) &= (U_0 \mathbf{e}_y, 0) \\
(\mathbf{U}'_3, \mathbf{\Omega}'_3) &= (U_0 \mathbf{e}_z, 0) \\
(\mathbf{U}'_4, \mathbf{\Omega}'_4) &= (0, \Omega_0 \mathbf{e}_x) \\
(\mathbf{U}'_5, \mathbf{\Omega}'_5) &= (0, \Omega_0 \mathbf{e}_y) \\
(\mathbf{U}'_6, \mathbf{\Omega}'_6) &= (0, \Omega_0 \mathbf{e}_z).
\end{aligned}$$

Because the fluid flow vanishes at infinity $\mathbf{v}(\mathbf{x} \rightarrow \infty) = 0$, the Lorentz reciprocal theorem reads

$$\int_{\partial\Sigma} dS \mathbf{v}'_i \cdot \boldsymbol{\sigma} \cdot \mathbf{n} = \int_{\partial\Sigma} dS \mathbf{v} \cdot \boldsymbol{\sigma}'_i \cdot \mathbf{n}. \quad (2.22)$$

For the force driven particle, the boundary conditions are $\mathbf{v}'_s = \mathbf{U}'_i + \mathbf{\Omega}'_i \times (\mathbf{r} - \mathbf{r}_0)$ and the left hand side of Eq. (2.22) changes to

$$\begin{aligned}
&\int_{\partial\Sigma} dS (\mathbf{U}'_i + \mathbf{\Omega}'_i \times (\mathbf{r} - \mathbf{r}_0)) \boldsymbol{\sigma} \cdot \mathbf{n} \\
&= \mathbf{U}'_i \cdot \int_{\partial\Sigma} dS \boldsymbol{\sigma} \cdot \mathbf{n} + \mathbf{\Omega}'_i \cdot \int_{\partial\Sigma} dS (\mathbf{r} - \mathbf{r}_0) \times \boldsymbol{\sigma} \cdot \mathbf{n} \\
&= \mathbf{U}'_i \cdot \mathbf{F} + \mathbf{\Omega}'_i \cdot \boldsymbol{\tau}.
\end{aligned} \quad (2.23)$$

\mathbf{F} and $\boldsymbol{\tau}$ are the forces and torques acting on the microswimmer.

Repeating the same calculation for the right side of (2.22) with $\mathbf{v}_{\text{surface}} = \mathbf{U}_i + \mathbf{\Omega}_i \times (\mathbf{r} - \mathbf{r}_0) + \mathbf{v}_s$ leads to

$$\mathbf{U}_i \cdot \mathbf{F}' + \mathbf{\Omega}_i \cdot \boldsymbol{\tau}' + \int_{\partial\Sigma} dS \mathbf{v}_s \cdot \boldsymbol{\sigma}'_i \cdot \mathbf{n}. \quad (2.24)$$

Active particles are force-free, $\mathbf{F} = 0$ and torque-free $\boldsymbol{\tau} = 0$, and the forces necessary to drive the particle in the six chosen modes can be calculated using the code provided by Pozrikidis [198]. The problem reduces to a system of six equations with six unknowns: $U_x, U_y, U_z, \Omega_x, \Omega_y$ and Ω_z

$$\mathbf{U}_i \cdot \mathbf{F}' + \mathbf{\Omega}_i \cdot \boldsymbol{\tau}' = - \int_{\partial\Sigma} dS \mathbf{v}_s \cdot \boldsymbol{\sigma}'_i \cdot \mathbf{n}. \quad (2.25)$$

This system of equations can be solved.

2.8 Stresslet

In fluid dynamics the zeroth and first moment of the surface stress are commonly used to define three properties[125]; the stokeslet, stresslet and rotlet. Each of those terms represents a distinct flow field pattern (see Fig. 2.2) and fundamental solution to the Stokes equation.

The stokeslet

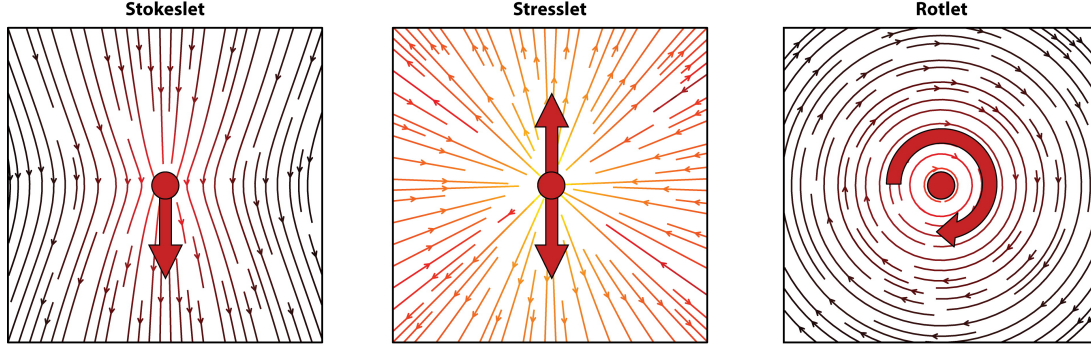


Figure 2.2: Characteristic flow fields created by stokeslet (left), stresslet (middle) and rotlet (right) respectively. The figure has been reprinted from [210] with the permission.

$$F_j = \oint (\sigma \cdot \mathbf{n})_j dS \quad (2.26)$$

is the solution to a single point force in zero Reynolds number flow. The first moment D_{jk} on the other hand is split into the symmetric stresslet S_{jk} , and the antisymmetric rotlet T_{jk} .

$$D_{jk} = \oint (\sigma \cdot \mathbf{n})_j \xi_k dS \quad (2.27)$$

$$D_{jk} - \frac{1}{3} D_{ii} \delta_{jk} = S_{jk} + T_{jk} \quad (2.28)$$

$$S_{jk} = \frac{1}{2} \int_{S_\alpha} [\sigma_{ji} n_i x_k + \sigma_{ki} n_i x_j] dS - \frac{1}{3} \int_{S_\alpha} \sigma_{li} n_i x_l dS \delta_{jk}. \quad (2.29)$$

By convention, the trace of D_{jk} is not part of either the stresslet or the rotlet since the incompressibility condition prevents any effect it might have on the fluid flow.

Self-propelled microswimmers are force and torque free, this removes any stokeslet or rotlet contribution to their flow fields. If the stresslet is non-zero, it is the slowest decaying term in the far field:

$$u_i = \frac{1}{8\pi\mu} \left(\frac{x_i \delta_{jk}}{r^3} - \frac{3x_i x_j x_k}{r^5} \right) S_{jk}^{(\alpha)}, \quad (2.30)$$

It is commonly used to distinguish two types of particles, puller and pusher. A pusher has a positive stresslet contribution and pushes the fluid immediately in front and behind its body away. A puller has a negative stresslet contribution.

2.9 Stokes stream function

For incompressible stokes flows with an axisymmetric geometry and boundary conditions a scalar auxiliary function $\psi(\mathbf{r})$ can be defined to replace the three dimensional flow field \mathbf{v} [93]. This scalar function relates to the flow field with the simple transformation

$$\mathbf{v} = \nabla \times \left(\frac{1}{h_\varphi} \psi \mathbf{e}_\varphi \right). \quad (2.31)$$

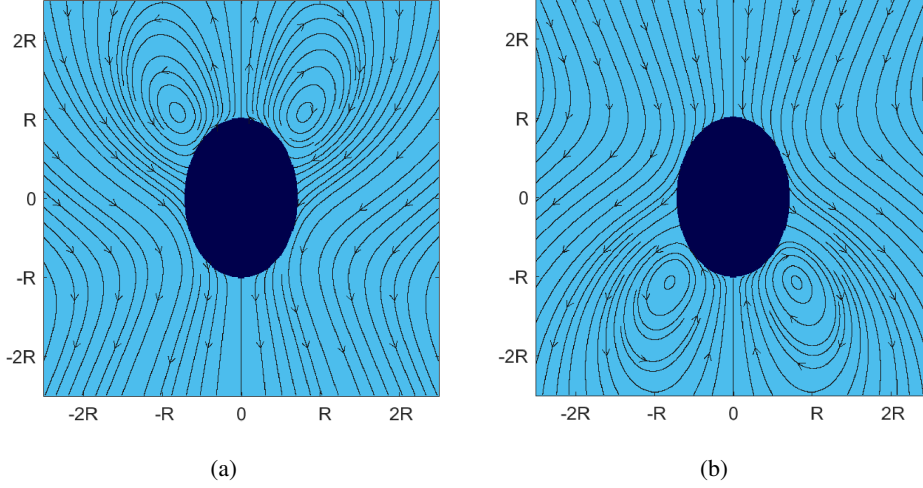


Figure 2.3: Velocity stream lines around (a) a puller and (b) a pusher spheroidal squirmer particle in free space. The system is chosen such that the particle is at rest (co-moving frame).

For any ψ the incompressibility condition is automatically fulfilled, since $\nabla \cdot \nabla \times f = 0$ for all functions f .

In order to rewrite Stokes equation (2.5) in terms of ψ , it is convenient to apply the curl operator on both sides of the equation. This eliminates the ∇p term and leaves

$$0 = \nabla \times (\nabla^2 \mathbf{v}(\mathbf{r})) \quad (2.32)$$

for a system without external forces $\mathbf{f} = 0$. Using $\nabla \cdot \mathbf{v} = 0$ in the vector identity

$$\nabla^2 = \nabla(\nabla \cdot \mathbf{v}) - \nabla \times (\nabla \times \mathbf{v}) \quad (2.33)$$

Eq. (2.32) rewrites as

$$\begin{aligned} 0 &= \nabla \times (\nabla \times (\nabla \times \mathbf{v})) \\ \Leftrightarrow E^4 \psi &= 0. \end{aligned} \quad (2.34)$$

E^2 is a differential operator depending on the chosen coordinate system

$$E^2 = \nabla^2 - \frac{2}{k} \frac{\partial}{\partial k}. \quad (2.35)$$

Here k is the coordinate orthogonal to the axis of symmetry. If ψ solves Eq. (2.34) with the appropriate boundary conditions, then (2.31) is the unique solution to the corresponding Stokes problem.

CHAPTER 3

PUBLISHED WORK

Two chapters of the work presented in this thesis have been published in peer reviewed journals and are reprinted with the permission of the publisher. A third paper I have co-authored during my time at University of Hawai'i at Manoa discusses an alternative propulsion mechanism ("Induced-charge electrophoresis"). It is not included in this thesis, but in part inspired the work leading to the forth chapter presented here. That chapter is currently in preperation for submission to a peer review journal.

- Full papers:
 - Poehnl, R., Popescu, M. N., & Uspal, W. E. (2020). Axisymmetric spheroidal squirmers and self-diffusiophoretic particles. *Journal of Physics: Condensed Matter*, 32(16), 164001.
 - Poehnl, R., & Uspal, W. (2021). Phoretic self-propulsion of helical active particles. *Journal of Fluid Mechanics*, 927, A46.
- Publications
 - Katuri, J., Poehnl, R., Sokolov, A., Uspal, W., & Snezhko, A. (2022). Arrested-motility states in populations of shape-anisotropic active Janus particles. *Science Advances*, 8(26), eabo3604.

CHAPTER 4

PHORETIC SELF-PROPULSION OF HELICAL ACTIVE PARTICLES

Starting the discussion of self-propelled microswimmers with non-isotropic geometries, a self-diffusiophoretic helical colloid in free space is considered. Self-diffusiophoretic colloids are a type of artificial microswimmers commonly used in experiments. They do not rely on an external field for their propulsion mechanism, enabling their usage in a wide range of environments with no or limited accessibility for humans.

The work presented in this chapter has been published in the peer reviewed journal *Journal of Fluid Mechanics* [187] and the copyrights are owned by Cambridge University Press & Assessment. The results are reprinted with the permission request waived due to the policies outlined by Cambridge University Press & Assessment [1].

4.1 Abstract

Chemically active colloids self-propel by catalysing the decomposition of molecular “fuel” available in the surrounding solution. If the various molecular species involved in the reaction have distinct interactions with the colloid surface, and if the colloid has some intrinsic asymmetry in its surface chemistry or geometry, there will be phoretic flows in an interfacial layer surrounding the particle, leading to directed motion. Most studies of chemically active colloids have focused on spherical, axisymmetric “Janus” particles, which (in the bulk, and in absence of fluctuations) simply move in a straight line. For particles with complex (non-spherical and non-axisymmetric) geometry, the dynamics can be much richer. Here, we consider chemically active helices. Via numerical calculations and slender body theory, we study how the translational and rotational velocities of the particle depend on geometry and the distribution of catalytic activity over the particle surface. We confirm the recent finding of [116] that both tangential and circumferential concentration gradients contribute to the particle velocity. The relative importance of these contributions has a strong impact on the motion of the particle. We show that by a judicious choice of the particle design parameters, one can suppress components of angular velocity that are perpendicular to the screw axis, or even select for purely “sideways” translation of the helix.

4.2 Introduction

Many micro-organisms self-propel through liquid by continuously rotating a helical or screw-like filament. A prime example is *E. coli*. In order to swim, it bundles its flagella in a single helical tail and rotates the bundle to propel itself forward. The prominence of this swimming strategy in the microscopic realm derives from the unique properties of highly viscous flows:

owing to the linearity and time reversibility of the Stokes equation, a time-reversible sequence of mechanical deformations of a swimmer’s body cannot induce a net displacement [200]. Continuous rotation of a helical tail evades this so-called “scallop theorem.” In terms of mechanical forces, this swimming strategy exploits the anisotropy of the Stokes drag force on a moving rod; the entire tail can be regarded as made up of rod-like segments, and the anisotropic drag, when integrated over the helix contour, yields a net propulsive force, i.e., thrust [135].

Recently, inspired by nature, and facilitated by advances in colloid fabrication methods, a wide range of artificial microswimmers has been developed. Initially, manufacturing capabilities limited those to simple shapes, e.g., spheres, spheroids, and rods. However, more recently, complex and non-axisymmetric shapes have come into focus [77]. For instance, Gibbs and Fischer showcase helical microdrills that consist of a spherical “head” and helical “tail” [78]. On the surface, the design resembles the aforementioned *E. coli*. However, this design is a self-phoretic particle: it is covered by a catalyst, and when immersed in a solution containing molecular “fuel,” induces and sustains gradients of the various molecular species involved in the reaction. The chemical gradients, in conjunction with the molecular forces of interaction between the molecules and the particle surface, drive fluid flow in the vicinity of the particle surface, leading to directed motion [6]. Accordingly, the superficial similarity between *E. coli*, a mechanical swimmer, and self-phoretic helical swimmers may not hold up upon more detailed investigation. For instance, it is not obvious whether self-phoretic helices would exhibit any significant rotation around the helix axis, or display circular trajectories when in the vicinity of a solid boundary, a well-known behaviour of *E. coli* [21, 133]. Furthermore, the optimal geometry of a helical self-phoretic swimmer for self-propulsion is of obvious interest, and may not be identical to that of a mechanical swimmer. As another example, we note that enhancing the screw axis rotation of a self-phoretic helix would enhance its function as a microdrill. However, rotations with respect to the other body axes would hinder this function. More generally, rotary micromotors and nanomotors are envisioned as key elements of future active colloidal machines [11, 123]; being able to control their motion (e.g., by restricting rotation to only one body-fixed axis) by design would boost development of these applications.

The aim of this work is to develop a framework to study implications of the helical geometry for self-phoretic swimmers, and their possibilities for a wide range of applications, e.g., in lab-on-a-chip devices or for targeted drug delivery. We start by introducing the mathematical description of the particle shape in Section 4.3.1. We then outline the physical model and governing equations in Section 4.3.2. In Section 4.3.3, we specify activity profiles, i.e., distributions of catalytic activity over the particle surface. We detail three model activity profiles that are relevant to current experiments. Before presenting our results, we outline our numerical method in Section 4.3.5. In the results (Section 4.4), we discuss the hydrodynamic resistance tensor in Sect. 4.4.1, and then the concentration field and the particle velocities for three different activity profiles in Sects. 4.4.2, 4.4.3, and 4.4.4. Finally, we provide a novel and detailed development of slender body theory (SBT) for the concentration in Section 4.4.5.

On this path, the hydrodynamic resistance tensor turns out to be a highly important quantity. Calculation of the hydrodynamic resistance tensor for a helix is a classical problem in low Reynolds number hydrodynamics that sparks interest in its own right [60, 85, 112, 173, 201, 207]. Moreover, it has additional relevance for application to magnetically driven helical swimmers [23, 76, 152, 161, 184]. With our numerical implementation of the boundary element method (BEM), we obtain good agreement with the experimental estimates of resistance tensor components obtained by [201] and corresponding numerical calculations from [47], validating our approach. Moreover, we find that slender body theory, which resolves hydrodynamic interactions between particle segments – but not the finite thickness of the particle – exhibits excellent agreement with detailed calculations obtained with the BEM. In contrast, resistive force theory, which neglects hydrodynamic interactions, performs poorly [207]. These findings have implications for the study of helix sedimentation dynamics [173].

Regarding the concentration, our numerical calculations and extended slender body theory show that, in general, there will be circumferential spatial variations (i.e., variations circling around the contour tangent vector) in the vicinity of the particle surface. Notably, these variations are absent for simple geometries, e.g., spheres and spheroids with axisymmetric patterning, and they contribute to particle motion. Depending on the helix parameters (pitch, catalyst coverage, etc.), these variations can become negligible compared to, or dominate over, the tangential variations. In the latter case, one can observe significant motion perpendicular to the helix screw axis. This qualitative dependence on the helix parameters allows one to choose between a wide range of possible trajectories by changing only one or two aspects of the helix.

4.3 Theory

4.3.1 Particle geometry

We consider a solid particle that has the shape of a cylindrical tube bent into a helical contour (figure 4.1). The tube radius is r_0 , the radius of the helix centerline around the helix axis is R , the helix pitch is λ , the end-to-end distance is L , and the total contour length of the helix is \mathcal{L} . The two ends of the particle are terminated by hemispherical caps with radius r_0 . The centerline of the helix (between the two caps) is described by a space curve $\mathbf{x}_h(t)$ parameterized by t :

$$\begin{aligned}x_h &= R \cos t \\y_h &= R \sin t \\z_h &= bt,\end{aligned}\tag{4.1}$$

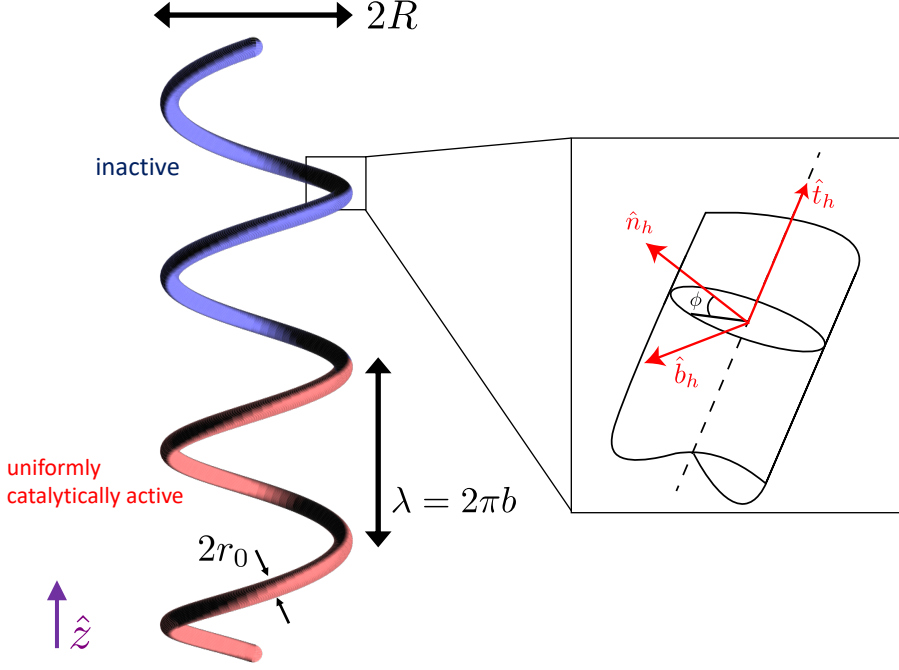


Figure 4.1: Schematic illustration of the particle geometry. The particle consists of a solid “tube” with a helical contour and circular cross-section, plus two solid hemispherical endcaps. Here, we label the contour radius R , the helix pitch λ , the tube radius r_0 , the local tangent vector $\hat{\mathbf{t}}_h$, the local surface normal $\hat{\mathbf{n}}_h$, and the local surface binormal $\hat{\mathbf{b}}_h$. For a given point on the helix centerline, the angle ϕ defines a point on the tube surface. In this example, the particle has a “lengthwise Janus” catalytic activity profile.

where $2\pi b = \lambda$. The helix has N turns, so that $L = N\lambda$, $\mathcal{L} = N\sqrt{\lambda^2 + (2\pi R)^2}$, and $t \in \{0, 2\pi N\}$. The surface of the tube (between the end caps) is described by

$$\begin{aligned} x_s &= R \cos t - r_0 \cos t \cos \phi + \frac{r_0 b}{\sqrt{R^2 + b^2}} \sin t \sin \phi \\ y_s &= R \sin t - r_0 \sin t \cos \phi - \frac{r_0 b}{\sqrt{R^2 + b^2}} \cos t \sin \phi \\ z_s &= bt + \frac{r_0 b}{\sqrt{R^2 + b^2}} \cos \phi, \end{aligned} \quad (4.2)$$

where $\phi \in \{0, 2\pi\}$ is an angle that describes position on the circular cross-section of the tube surface centered at position t on the centerline. At any point t on the helix, the tangent vector $\hat{\mathbf{t}}_h \equiv \frac{\partial \mathbf{x}_h}{\partial t} / |\frac{\partial \mathbf{x}_h}{\partial t}|$, normal vector $\hat{\mathbf{n}}_h \equiv \frac{\partial \hat{\mathbf{t}}_h}{\partial t} / |\frac{\partial \hat{\mathbf{t}}_h}{\partial t}|$ and binormal vector $\hat{\mathbf{b}}_h \equiv \hat{\mathbf{t}}_h \times \hat{\mathbf{n}}_h$ define three orthogonal vectors, where $\hat{\mathbf{t}}_h = \left(-\frac{R \sin t}{\sqrt{R^2 + b^2}}, \frac{R \cos t}{\sqrt{R^2 + b^2}}, \frac{b}{\sqrt{R^2 + b^2}} \right)$, $\hat{\mathbf{n}}_h = (-\cos t, -\sin t, 0)$, and $\hat{\mathbf{b}}_h = \left(\frac{b \sin t}{\sqrt{R^2 + b^2}}, -\frac{b \cos t}{\sqrt{R^2 + b^2}}, \frac{R}{\sqrt{R^2 + b^2}} \right)$. Accordingly, for a point on the surface of the tube, $\phi = 0^\circ$ if the point is displaced from the helix centerline along the local normal $\hat{\mathbf{n}}_h$, and $\phi = 90^\circ$ if it is displaced from the centerline along the local binormal $\hat{\mathbf{b}}_h$. Note that the local surface normal $\hat{\mathbf{n}}_h$ always points towards the axis of the helix, entailing that a point on the particle

surface with $\phi = 0^\circ$ is in the interior space.

For the following analysis, we also find it useful to define the tangential position $s \in [-1, 1]$ along the centerline of the cylindrical tube, where $s = -1$ corresponds to the centre of the base of one hemispherical endcap, $s = 1$ to the centre of the base of the other hemispherical endcap, and $s = 0$ to the midpoint of the contour. Additionally, all geometric quantities will be specified in terms of a characteristic length scale $L_0 \sim R$.

4.3.2 Physical model and governing equations

We consider a stationary reference frame in which the instantaneous position of the geometric centroid of the helix is $\mathbf{x}_p = (x_p, y_p, z_p)$. The helix is immersed in a liquid solution containing reactant (“fuel”) molecules, and part of the surface of the helix catalyses the decomposition of the reactant, producing a reaction product that has a number density field $c(\mathbf{x})$ (hereafter called the concentration field), where \mathbf{x} is a position in the solution. We assume that the characteristic timescale for diffusion of the reactant is much smaller than the characteristic timescale for particle motion. Therefore, the concentration field can be regarded as quasi-static, and it satisfies the Laplace equation $\nabla^2 c = 0$. The concentration field is subject to the boundary conditions $c(|\mathbf{x}| \rightarrow \infty) = 0$ and $-D[\hat{\mathbf{n}} \cdot \nabla c] = \kappa j(\mathbf{x}_s)$ on the particle surface. Here, D is the diffusion coefficient of the product molecules, κ is a characteristic rate of solute production per unit area, \mathbf{x}_s is a position on the particle surface, and $\hat{\mathbf{n}}$ is a unit vector locally normal to the particle surface. The normal is defined to point into the fluid. (Note that the surface normal $\hat{\mathbf{n}}$ is distinct from the space curve normal $\hat{\mathbf{n}}_h$ introduced in the previous section. In particular, $\hat{\mathbf{n}} = \cos \phi \hat{\mathbf{n}}_h + \sin \phi \hat{\mathbf{b}}_h$ over the tube surface.) The function $j(\mathbf{x}_s)$ is dimensionless, and describes the distribution of catalytic activity over the particle surface. For simplicity, we have assumed zeroth order kinetics, i.e., the activity has no dependence on the product concentration $c(\mathbf{x})$.

The above problem for $c(\mathbf{x})$ can be solved numerically, using the boundary element method. Once $c(\mathbf{x})$ is known, one can obtain the surface gradient $\nabla_s c$, where $\nabla_s \equiv (\mathbf{1} - \hat{\mathbf{n}}\hat{\mathbf{n}}) \cdot \nabla$. Since $\nabla_s c$ is defined on the surface of the particle, it lies within a plane that is locally tangent to the tube surface and has normal $\hat{\mathbf{n}}$. Conceptually, we can decompose $\nabla_s c$ into a tangential component, $(\hat{\mathbf{t}}_h \cdot \nabla_s c) \hat{\mathbf{t}}_h$, and a circumferential component $(\mathbf{1} - \hat{\mathbf{t}}_h \hat{\mathbf{t}}_h) \cdot \nabla_s c = (\hat{\mathbf{n}}_h \cdot \nabla_s c) \hat{\mathbf{n}}_h + (\hat{\mathbf{b}}_h \cdot \nabla_s c) \hat{\mathbf{b}}_h$. This decomposition will be useful in the subsequent analysis.

The suspending fluid is assumed to be Newtonian and governed by the Stokes equation

$$-\nabla P + \mu \nabla^2 \mathbf{u} = 0, \quad (4.3)$$

and incompressibility condition $\nabla \cdot \mathbf{u} = 0$, where $\mathbf{u}(\mathbf{x})$ is the velocity of the fluid, $P(\mathbf{x})$ is the fluid pressure, and μ is the viscosity. The fluid velocity is subject to the boundary conditions

$$\mathbf{u}(\mathbf{x}_s) = \mathbf{U} + \boldsymbol{\Omega} \times (\mathbf{x}_s - \mathbf{x}_p) + \mathbf{v}_s(\mathbf{x}_s) \quad (4.4)$$

on the surface of the helical particle, where \mathbf{U} and $\boldsymbol{\Omega}$ are the (unknown) translational and

(j)	$\mathbf{U}^{(j)}$	$\mathbf{\Omega}^{(j)}$
1	$U_a \hat{\mathbf{x}}$	0
2	$U_a \hat{\mathbf{y}}$	0
3	$U_a \hat{\mathbf{z}}$	0
4	0	$\Omega_a \hat{\mathbf{x}}$
5	0	$\Omega_a \hat{\mathbf{y}}$
6	0	$\Omega_a \hat{\mathbf{z}}$

Table 4.1: Boundary conditions for the auxiliary problem (j) .

angular velocities of the particle, as well as $\mathbf{u}(|\mathbf{x}| \rightarrow \infty) = 0$. The quantity \mathbf{v}_s , the so-called phoretic slip velocity, is obtained as $\mathbf{v}_s = -b(\mathbf{x}_s) \nabla_s c$, where $b(\mathbf{x}_s)$, the so-called surface mobility, is a material dependent quantity that encodes interactions between the reactant and the particle surface [6]. Finally, to close the system of equations, we specify that the particle is force-free,

$$\int_S \boldsymbol{\sigma} \cdot \hat{\mathbf{n}} \, dS = 0, \quad (4.5)$$

and torque-free,

$$\int_S (\mathbf{x}_s - \mathbf{x}_p) \times \boldsymbol{\sigma} \cdot \hat{\mathbf{n}} \, dS = 0. \quad (4.6)$$

where S indicates an integral over the particle surface.

In order to solve this problem for \mathbf{U} and $\mathbf{\Omega}$, we use the Lorentz reciprocal theorem. This theorem relates two solutions to the Stokes equation with the same geometry but different boundary conditions. For an auxiliary problem (j) , we write:

$$\int_S \mathbf{u} \cdot \boldsymbol{\sigma}^{(j)} \cdot \hat{\mathbf{n}} \, dS = \int_S \mathbf{u}^{(j)} \cdot \boldsymbol{\sigma} \cdot \hat{\mathbf{n}} \, dS, \quad (4.7)$$

where auxiliary problem (j) has the boundary conditions

$$\mathbf{u}^{(j)}(\mathbf{x}_s) = \mathbf{U}^{(j)} + \mathbf{\Omega}^{(j)} \times (\mathbf{x}_s - \mathbf{x}_p) \quad (4.8)$$

and $\mathbf{u}^{(j)}(|\mathbf{x}| \rightarrow \infty) = 0$, i.e., the particle moves as a rigid body with no slip on the surface. We specify six auxiliary problems $j \in \{1, 2, \dots, 6\}$, with the boundary conditions for each (j) given in table 4.1.

Combining equations 4.4, 4.7, and 4.8, we obtain

$$\begin{aligned} \mathbf{U} \cdot \int_S \boldsymbol{\sigma}^{(j)} \cdot \hat{\mathbf{n}} \, dS + \mathbf{\Omega} \cdot \int_S (\mathbf{x}_s - \mathbf{x}_p) \times \boldsymbol{\sigma}^{(j)} \cdot \hat{\mathbf{n}} \, dS + \int_S \mathbf{v}_s(\mathbf{x}_s) \cdot \boldsymbol{\sigma}^{(j)} \cdot \hat{\mathbf{n}} \, dS = \\ \mathbf{U}^{(j)} \cdot \int_S \boldsymbol{\sigma} \cdot \hat{\mathbf{n}} \, dS + \mathbf{\Omega}^{(j)} \cdot \int_S (\mathbf{x}_s - \mathbf{x}_p) \times \boldsymbol{\sigma} \cdot \hat{\mathbf{n}} \, dS. \end{aligned} \quad (4.9)$$

According to equations 4.5 and 4.6, the two integrals on the right hand side vanish. Moreover, on the left hand side, we recognize that the integrals represent components of the hydrodynamic resistance matrix R (with a negative sign). Accordingly, the equation can be

represented as a linear system

$$6\pi\mu \mathbf{R} \cdot \begin{pmatrix} \mathbf{U} \\ \mathbf{\Omega} \end{pmatrix} = \mathbf{b}, \quad (4.10)$$

where the six-component right hand side vector \mathbf{b} is

$$b_j = \int_S \mathbf{v}_s(\mathbf{x}_s) \cdot \boldsymbol{\sigma}^{(j)} \cdot \hat{\mathbf{n}} dS / V^{(j)}, \quad (4.11)$$

where $V^{(j)} = V_a$ for $j \in \{1, 2, 3\}$, and $V^{(j)} = \Omega_a$ for $j \in \{4, 5, 6\}$. Note the factor of $6\pi\mu$ appears in equation 4.10 because of how we choose to define R . The various components of R are proportional to, and have the same units as, L_0 , L_0^2 , or L_0^3 . Equation 4.10 can be solved by standard methods to determine \mathbf{U} and $\mathbf{\Omega}$. Interestingly, the right-hand side vector \mathbf{b} can be regarded as a generalized effective swimming force; the first three rows have units of force, and last three rows have units of torque.

Finally, from consideration of the governing equations, we determine a characteristic concentration $c_0 \equiv \kappa L_0/D$ and a characteristic velocity $U_0 = |b_0|\kappa/D$, where $|b_0|$ is a characteristic surface mobility coefficient. A characteristic force can be defined as $F_0 \equiv \mu U_0 L_0$. In the following, we will present quantitative results in terms of these characteristic quantities, except where noted.

4.3.3 Specification of catalytic activity and surface chemistry

In this work, we consider three choices of $j(\mathbf{x}_s)$. For all choices, we present results for uniform surface mobility, i.e., $b(\mathbf{x}_s) = b_0$, where $b_0 < 0$. The sign of b_0 ensures that the solute/surface interaction is repulsive, such that the particle tends to propel away from regions of high solute concentration. Although we examined the effect of a surface mobility contrast between the catalytic and inert regions, we did not find it to qualitatively change the results presented below.

Lengthwise Janus particle

For the “lengthwise Janus” particle, like the one shown in figure 4.1, we choose $j(\mathbf{x}_s) = \Theta(s)$ for a position on the surface of the cylindrical tube, where $\Theta(s)$ is the Heaviside step function. Additionally, the hemispherical endcap with its base at the point $s = -1$ has $j(\mathbf{x}_s) = 1$, and the endcap with its base at the point $s = 1$ has $j(\mathbf{x}_s) = 0$. In other words, half of the particle is uniformly catalytic, and the other half is inert.

z-wise Janus particle

For the “z-wise Janus” particle, we choose $j(\mathbf{x}_s) = -(\hat{\mathbf{n}} \cdot \hat{\mathbf{z}})\Theta(-\hat{\mathbf{n}} \cdot \hat{\mathbf{z}})$. For this particle, the region of the surface with a negative z-component of the local surface normal $\hat{\mathbf{n}}$ is catalytically active. Additionally, over this region, the catalytic activity is proportional to the z-component of the local surface normal. This activity profile is shown in figure 4.8(a) for a particular

choice of helix geometry. Note that this particle has an inherent polarity in the activity profile, so that one expects translational motion in the z -direction and rotation around the z -axis.

There are several motivations for examining this activity profile. First, it is similar to the experimentally relevant case of a Janus particle with a coating of catalytic material whose thickness smoothly varies, with position on the surface, from zero thickness to some maximum [43, 193]. This spatially varying thickness is often obtained in coating deposition processes. It is also similar to the case of a light-activated Janus particle, for which the catalytic activity on the surface is locally proportional to the flux of incident light [237]. As a further motivation, to be developed below, one can expect phoretic motion of these particles to be dominated by circumferential concentration gradients.

Inside-outside Janus particle

For the third model activity profile, we designate $j(\mathbf{x}_s) = \Theta(\phi + \pi/2)\Theta(-\phi - \pi/2)$. In this case, the activity varies only with the circumferential angle ϕ . The surfaces pointing towards the interior space of the helix are inert, and the chemical reaction is limited to the outside facing surfaces.

Helical fibers with this activity profile could be obtained using a coaxial capillary microfluidic system, as shown by [259]. Additionally, one can imagine obtaining it in a deposition process. The particle is first formed out of an inert material, and in a second step, the catalyst is deposited onto it. For this activity profile, we assume the catalyst only covers the easier to reach outside of the helix and leaves the inside inert.

4.3.4 Three-dimensional trajectories

In general, for a chemically active helical particle, all six components of the translational and rotational velocity will be non-zero, except when components vanish by symmetry (e.g., for a particle with uniform activity and uniform surface mobility). Therefore, one expects active helices to generally exhibit helical trajectories [252]. The radius r_{traj} of the helical trajectory is given as

$$r_{\text{traj}} = \frac{|\mathbf{U} \times \boldsymbol{\Omega}|}{|\boldsymbol{\Omega}|^2} \quad (4.12)$$

and the pitch as

$$\lambda_{\text{traj}} = 2\pi \frac{|\mathbf{U} \cdot \boldsymbol{\Omega}|}{|\boldsymbol{\Omega}|^2}, \quad (4.13)$$

where \mathbf{U} and $\boldsymbol{\Omega}$ are evaluated in a body-fixed coordinate system. Although we do not further consider particle trajectories in this work, we note that they can be straightforwardly calculated from equations 4.12, 4.13, and the velocities calculated below.

4.3.5 Numerical method for solution of PDEs

In order to solve the Laplace and Stokes equations numerically, we use the boundary element method (BEM) [197, 199, 236]. Briefly, in this method, the PDE of interest is recast as an

integral equation over the surface of the particle. For instance, for Laplace's equation, one can obtain the following equation via manipulation of Green's identities [236]:

$$\int_{\mathcal{V}} c(\mathbf{x}) \nabla^2 G(\mathbf{x}, \mathbf{x}_0) dV = - \int_S [c(\mathbf{x}) \nabla G(\mathbf{x}, \mathbf{x}_0) - G(\mathbf{x}, \mathbf{x}_0) \nabla c(\mathbf{x})] \cdot \hat{\mathbf{n}} dS. \quad (4.14)$$

Here, \mathcal{V} is the fluid domain (i.e., the domain exterior to the particle), S is the particle surface, and \mathbf{x}_0 is an observation point, which may be placed anywhere (i.e., in \mathcal{V} , inside the particle, or on the particle surface S). The integrals are taken with respect to \mathbf{x} . The Green's function $G(\mathbf{x}, \mathbf{x}_0)$ solves the Poisson equation

$$\nabla^2 G(\mathbf{x}, \mathbf{x}_0) + \delta(\mathbf{x} - \mathbf{x}_0) = 0, \quad (4.15)$$

and is given by

$$G(\mathbf{x}, \mathbf{x}_0) = \frac{1}{4\pi|\mathbf{x} - \mathbf{x}_0|}. \quad (4.16)$$

For \mathbf{x}_0 on the particle surface, the integral on the left hand side of Eq. 4.14 has a singularity. Taking the Cauchy principal value, we obtain the following boundary integral equation:

$$\frac{1}{2}c(\mathbf{x}_0) = \int_S [c(\mathbf{x}) \nabla G(\mathbf{x}, \mathbf{x}_0) - G(\mathbf{x}, \mathbf{x}_0) \nabla c(\mathbf{x})] \cdot \hat{\mathbf{n}} dS. \quad (4.17)$$

In the problem considered in this work, Eq. 4.17 relates the unknown surface concentration c to the given $\hat{\mathbf{n}} \cdot \nabla c$. For the Stokes equation, one can obtain the following single-layer formulation of the boundary integral equation, given in index notation [103, 105, 197]:

$$u_k(\mathbf{x}_0) = - \int_S [\mathcal{G}_{ik}(\mathbf{x}_0, \mathbf{x}) q_i] dS, \quad \mathbf{x}_0 \in S. \quad (4.18)$$

where \mathbf{x}_0 is on the particle surface. Here, the Green's function \mathcal{G} for the Stokes equation is

$$\mathcal{G}_{ij}(\mathbf{x}, \mathbf{x}_0) = \frac{1}{8\pi\mu r} \left(\delta_{ij} + \frac{\tilde{x}_i \tilde{x}_j}{r^2} \right), \quad (4.19)$$

where $\tilde{x}_j = x_j - x_{0,j}$ and $r \equiv |\mathbf{x} - \mathbf{x}_0|$. Concerning the quantity \mathbf{q} , we first define the traction $\mathbf{f} = \boldsymbol{\sigma} \cdot \hat{\mathbf{n}}$ exerted by the fluid exterior to the particle on the particle surface S . We additionally suppose that there is fluid interior to the particle volume, confined by S . The traction exerted by this fictitious interior fluid, which is subject to the same boundary conditions on S as the exterior fluid, is \mathbf{f}_{in} . The quantity \mathbf{q} is given as

$$\mathbf{q} = \mathbf{f} - \mathbf{f}_{in}, \quad (4.20)$$

and the unknown distribution of \mathbf{q} is related to a prescribed surface distribution of \mathbf{u} (e.g., rigid body motion in the six auxiliary problems) by Eq. 4.18. The quantity \mathbf{q} is defined up to a constant multiple of the surface normal $\hat{\mathbf{n}}$, as incompressibility implies $\int_S \mathcal{G} \cdot \hat{\mathbf{n}} dS = 0$. One can choose for this constant to be zero by imposing $\int_S \mathbf{q} \cdot \hat{\mathbf{n}} dS = 0$. For the case of rigid

body motion, \mathbf{f}_{in} is simply a constant multiple of $\hat{\mathbf{n}}$, and \mathbf{q} can simply be replaced with \mathbf{f} .

Each boundary integral equation can be discretized by meshing the surface of the particle, yielding a dense linear system that can be solved numerically. To implement the boundary element method for active colloids, we adapt the open source numerical library BEMLIB [199]. For the helical filaments considered here, the large variation in length scales can make this geometry numerically challenging. Furthermore, the interface between catalytic and inert regions of the particle surface must be resolved carefully. For all data points obtained with the BEM and presented below, we confirm numerical convergence with respect to mesh refinement. Specifically, as a rule of thumb, we consider numerical convergence to be obtained when we obtain no more than 3% change in all quantities of interest upon addition of 10 000 or more surface elements. Where possible, we compare our numerical data against slender body theory for further validation. For the “lengthwise Janus” catalytic activity profile, it is potentially difficult to capture the abrupt change in activity with a discrete number of meshed points. Accordingly, we have considered both a “hard” step function activity profile and a “soft” hyperbolic tangent activity profile with a length scale $l_0 \sim r_0$, and found good quantitative agreement between them for $\sim 50\,000$ surface elements.

To obtain insight into the conditions for numerical convergence, we visually inspected the activity profiles by plotting $j(\mathbf{x}_s)$. We found that numerical convergence is associated with having a sufficiently smooth interface between the active and inert sides of the particle. An illustrative example of this smoothness is provided in Fig. 4.2. The BEM code solves for the concentration at nodes of the particle mesh (colored points). The red points represent catalytically active nodes of the mesh, while the green points represent inert nodes. The area elements of the mesh are colored by interpolation from the surrounding nodes; blue represents inert and yellow represents active. The interface between the inert and active sides shows that the active and inert nodes are separated. Moreover, the interface between the two sides is smooth and approximately lies within a plane containing a circular cross-section of the article. The slight roughness observed is due to slight differences / non-uniformity between the local density of nodes (which are distributed during the meshing process on the two sides). For future work, we suggest that refinement of the mesh near the interface could lead to gains in computational efficiency (requiring fewer nodes and elements for the same level of accuracy).

With regard to computational efficiency, we note that application of the Lorentz reciprocal theorem can save significant computational time in that, for a given helix geometry, the six auxiliary problems for the Stokes equation only need to be solved once. Solving these problems yields the resistance matrix and tractions that can be used for any distribution of surface slip. Therefore, one can examine different distributions of catalytic coverage, surface mobility parameters, etc., without having to perform additional hydrodynamic calculations.

Solution of the system in Eq. 4.10 yields the particle velocity, but not the flow field $\mathbf{u}(\mathbf{x})$. When desired, the flow field can be obtained by subsequent additional numerical solution of Eq. 4.18, subject to the (now completely known) boundary condition Eq. 4.4. One can then

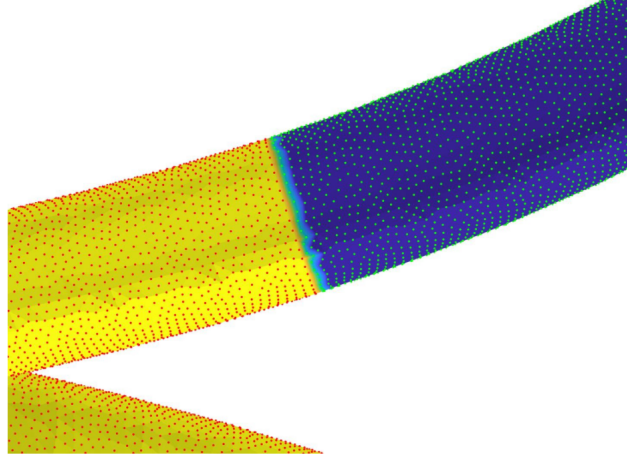


Figure 4.2: Close-up of a meshed interface for a lengthwise Janus particle under conditions of numerical convergence. The red points represent catalytically active nodes of the mesh, while the green points represent inert nodes. The area elements of the mesh are colored by interpolation from the surrounding nodes; blue represents inert and yellow represents active.

obtain the velocity field using the boundary integral equation

$$u_k(\mathbf{x}_0) = - \int_S [\mathcal{G}_{ik}(\mathbf{x}_0, \mathbf{x}) q_i] dS, \quad \mathbf{x}_0 \in \mathcal{V}. \quad (4.21)$$

4.4 Results

4.4.1 Hydrodynamic resistance tensor

As our starting point, we consider the hydrodynamic resistance tensor R of a helical filament, as it is a key quantity entering into equation 4.10. Each row j of R can be obtained by solving auxiliary problem (j) for rigid body motion of the helix and, from the solution for $\mathbf{u}^{(j)}$, calculating the force and torque on the particle. We can solve each auxiliary problem numerically, using the BEM.

In figure 4.3, we consider an example problem in order to both validate our numerical scheme and to shed some light on how the hydrodynamic resistance of a helix depends on its shape. Specifically, we obtain the components of R as a function of pitch λ for a helix with fixed contour length \mathcal{L} , fixed tube radius r_0 , and fixed contour radius R . This variation of λ can be regarded as “stretching out” an initially tightly coiled helix, as shown schematically in figure 4.3(a). Of particular interest are R_{33} , $R_{36} = R_{63}$, and R_{66} . The quantity R_{33} represents the coefficient for hydrodynamic drag (in the $\hat{\mathbf{z}}$ direction) on a helix translating along its screw axis, i.e., in the $\hat{\mathbf{z}}$ direction. Likewise, R_{66} represents the rotational drag coefficient for rotation around the helix axis. Finally, R_{63} represents translational-rotational coupling, i.e., the torque in the $\hat{\mathbf{z}}$ direction that results when a helix translates in the $\hat{\mathbf{z}}$ direction, *or* the force in the $\hat{\mathbf{z}}$ direction that results when a helix rotates around the $\hat{\mathbf{z}}$ axis.

Interestingly, we obtain non-monotonic behaviour for all three quantities shown in figure 4.3, with a minimum in R_{63} and maxima in R_{33} and R_{66} appearing around $\lambda/L_0 \approx 20$. In

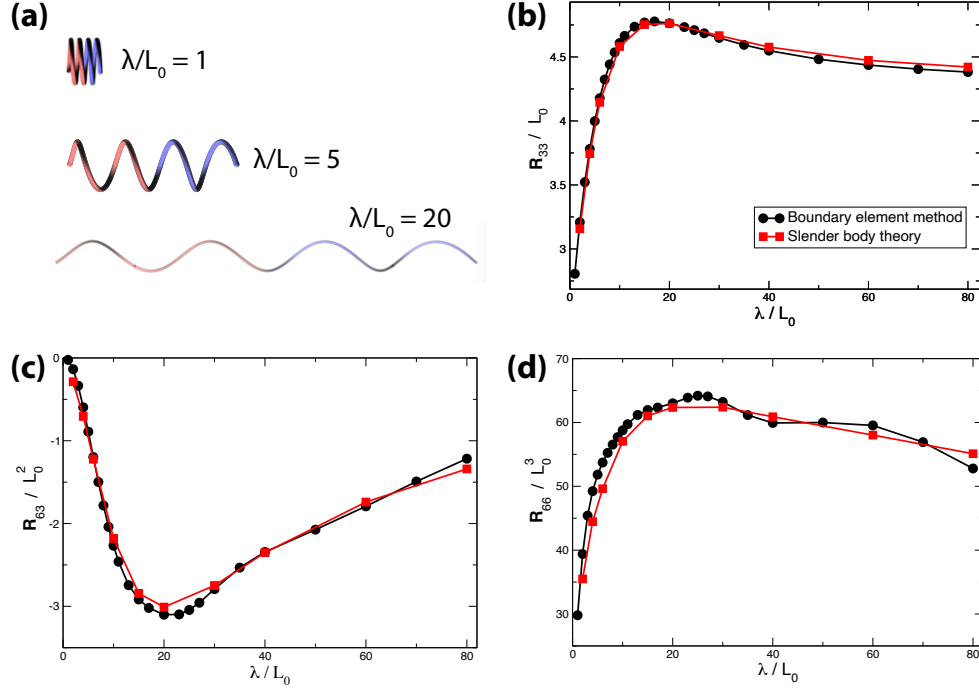


Figure 4.3: (a) Schematic illustration of three helices with different values of pitch λ , but identical contour length $\mathcal{L}/L_0 = 57.5$, contour radius $R/L_0 = 2.5$, and filament radius $r_0/L_0 = 0.265$. (b) Variation of R_{33} , the dimensionless drag coefficient for translational motion along the axis, with λ . Black circles were obtained with the boundary element method, and red circles were obtained by the slender body theory described in [126]. (c) Variation of the translational-rotational coupling coefficient R_{63} with λ . Note that $R_{63} = R_{36}$. (d) Variation of R_{66} , the dimensionless rotational drag coefficient for rotation around the helix axis, as a function of λ .

N_{turns}	ψ	R_{33}/L_0	R_{36}/L_0^2	R_{66}/L_0^3
5	20°	16.98	9.48	374.95
3	55°	5.11	2.61	63.91
5	55°	7.09	3.58	89.9

Table 4.2: Experimental measurements from [201], rescaled to be dimensionless for comparison with our BEM results in table 4.4.

N_{turns}	ψ	R_{33}/L_0	R_{36}/L_0^2	R_{66}/L_0^3
5	20°	15.16	7.43	331.41
3	55°	4.64	2.50	59.81
5	55°	6.45	3.39	96.52

Table 4.3: Numerical calculations from [47], rescaled to be dimensionless for comparison with our BEM results in table 4.4.

order to cross-check our results, we also performed calculations with slender body theory (SBT), as described in the work of [126]. The BEM and SBT broadly agree, except that with the BEM we obtain a slight oscillation in R_{66} as a function of λ (figure 4.3(d)). The minor discrepancies between SBT and BEM could be due to the fact the SBT does not account for the circumferential variation of hydrodynamic stress (i.e., variation with ϕ) over the surface of the particle. Moreover, the SBT equations in [126] assume that the cross-sectional radius of the particle varies as $r_b \sqrt{1 - s^2}$, where r_b is the maximum thickness; recall that our particle has uniform cross-section, except for the hemispherical endcaps.

We have also sought to compare our results with resistive force theory (RFT), using the expressions in [173] and [46]. For calculation of the components of the resistance tensor, resistive force theory treats the filament as consisting of hydrodynamically non-interacting rod-like segments. We obtained semi-quantitative agreement of RFT with SBT and BEM for the variation of R_{36} with λ , semi-quantitative agreement for the variation of R_{36} with λ for $\lambda/L_0 > 30$, and poor agreement for R_{33} . It has been known since the work of Rodenborn *et al.* that RFT generally has poor quantitative agreement with theories that include non-local hydrodynamic interactions, such as SBT and BEM; therefore, we do not include the RFT results here.

As another check, we consider the helix geometries studied experimentally by [201] using metal wire and numerically with the regularized boundary element method by [47]. Specifically, both works consider a helix with fixed end-to-end distance L , number of turns L/λ , pitch angle $\psi = 2\pi R/\lambda$, and filament radius r_0 , with R determined from the fixed parameters. The treatment of the two helix ends is not explicitly reported in [47]. The quantities A , B , and D in [201] correspond to our R_{33} , R_{36} , and R_{66} , respectively, and are tabulated in table 4.2. Likewise, in [47], the quantities R , P_{33} and T_{33} , correspond to R_{33} , R_{36} , and R_{66} in this work, and are tabulated in table 4.3. However, the quantities given in [201] and [47] are dimensional. We rescaled the quantities to be dimensionless in table 4.2 and table 4.3 by choosing the length scale to be $L_0 = \frac{2}{5}R$. In table 4.4, we show that our implementation of the BEM has good agreement with [47] and good convergence with mesh

N_{turns}	ψ	R_{33}/L_0	R_{36}/L_0^2	R_{66}/L_0^3	N_{elm}	% error R_{33}	% error R_{36}	% error R_{66}
5	20°	15.37	-7.76	336.88	12 048	1.39	4.38	1.65
5	20°	15.37	-7.76	336.98	48 192	1.39	4.41	1.68
3	20°	4.66	-2.46	59.72	5 808	0.59	1.78	0.16
3	20°	4.66	-2.46	59.72	23 232	0.59	1.78	0.14
5	55°	6.55	-3.48	97.71	9 648	1.44	2.74	1.23
5	55°	6.55	-3.48	97.73	38 592	1.44	2.73	1.25

Table 4.4: Results of BEM numerical calculations for resistance matrix of a helix. Percent error is calculated with respect to the numerical data of [47]

refinement. The slight discrepancy between our results and those of [47] may be due to the treatment of the helix ends.

4.4.2 Lengthwise Janus chemically active particle

Now we consider the effect of catalytic activity for a lengthwise Janus particle, beginning with the concentration field c . In order to validate our boundary element numerical method, we compare the results of BEM for c against predictions of a slender body approach that will be developed in detail in Section 4.4.5 below. In figure 4.4(a), the grey area shows the range of variation of concentration on the surface of a particle as a function of tangential position s , determined with the BEM. Note that for each tangential position s there is a range of values of concentration c , indicated by the vertical extent of the grey area, due to variation of c with the circumferential angle ϕ . The red curve is the prediction of SBT, for this geometry and activity profile, of the circumferentially averaged concentration on the particle surface as a function of s . The red curve shows excellent agreement with the variation of the grey region with s . In figure 4.4(b), we show the concentration on the surface of the particle; the variation of c is dominated by tangential gradients, but circumferential variation is also clearly visible.

In order to gain a better understanding of the circumferential variation, we plot c as function of ϕ for different values of s in figure 4.4(c). The symbols were obtained with the BEM. For each value of s , we find that c varies with ϕ in a sinusoidal fashion, with the amplitude and phase depending on s . Interestingly, in the inert region of the particle ($s > 0$), the curves generally have maxima that approach $\phi \approx -\pi/2$ as s approaches $s = 1$. As detailed in Section 4.4.5, we extend SBT to account for circumferential variation of concentration. Briefly, we hypothesize that the concentration on the surface of a circular cross-section of the filament, at a given s , is polarized by an ambient gradient in concentration created by the rest of the particle. This hypothesis is shown schematically in figure 4.4(d). By making an analogy with a cylinder in uniform potential flow, we are able to obtain the solid curves in figure 4.4(c).

Now we consider the velocity of the lengthwise Janus particle as a function of pitch λ , with other geometric parameters the same as in figure 4.3. In figure 4.5(a), we show the three components of translational velocity. As one might expect, U_z is significantly greater in magnitude than U_x and U_y . Moreover, U_z is everywhere positive, as the particle is repelled

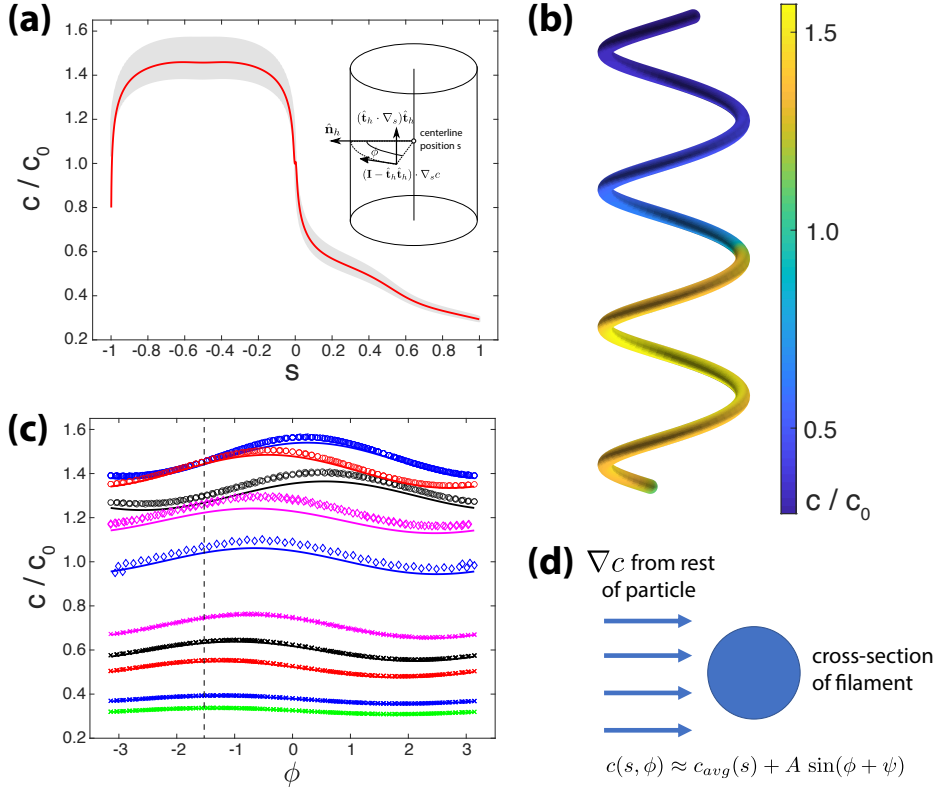


Figure 4.4: (a) Concentration with respect to the tangential position s for $\lambda/L_0 = 5$ and other parameters the same as in figure. 4.3. The shaded grey area shows the range of values that were obtained for c for a given s and various circumferential angles ϕ (individual data points are omitted for clarity). The solid curve is a theoretical expression for the circumferentially averaged concentration obtained with slender body theory. The inset shows the definition of the angle ϕ with respect to the local \hat{n}_h at a position s along the centerline, as well as decomposition of the surface concentration gradient $\nabla_s c$ into tangential and circumferential (i.e., in the plane of the helix cross-section at s) components. (b) Three-dimensional plot of the concentration c on the surface of the particle. (c) Variation of concentration c as a function of circumferential angle ϕ for various values of s . The dashed line indicates $\phi = -\pi/2$. (d) Schematic illustration of the modification of the slender body theory to obtain the circumferential variation of concentration around the cross-section at s . To obtain the solid curves in (c), it is assumed that the local concentration gradient created by the rest of the particle induces a dipolar variation of concentration on the filament surface with respect to ϕ . In (c), the values of s are as follows: black circles, $s = -0.95$; blue circles, $s = -0.65$; red circles, $s = -0.15$; magenta diamonds, $s = -0.02$; blue diamonds, $s = 0$; magenta crosses, $s = 0.05$; black crosses, $s = 0.15$; red crosses, $s = 0.35$; blue crosses, $s = 0.65$; green crosses, $s = 0.85$.

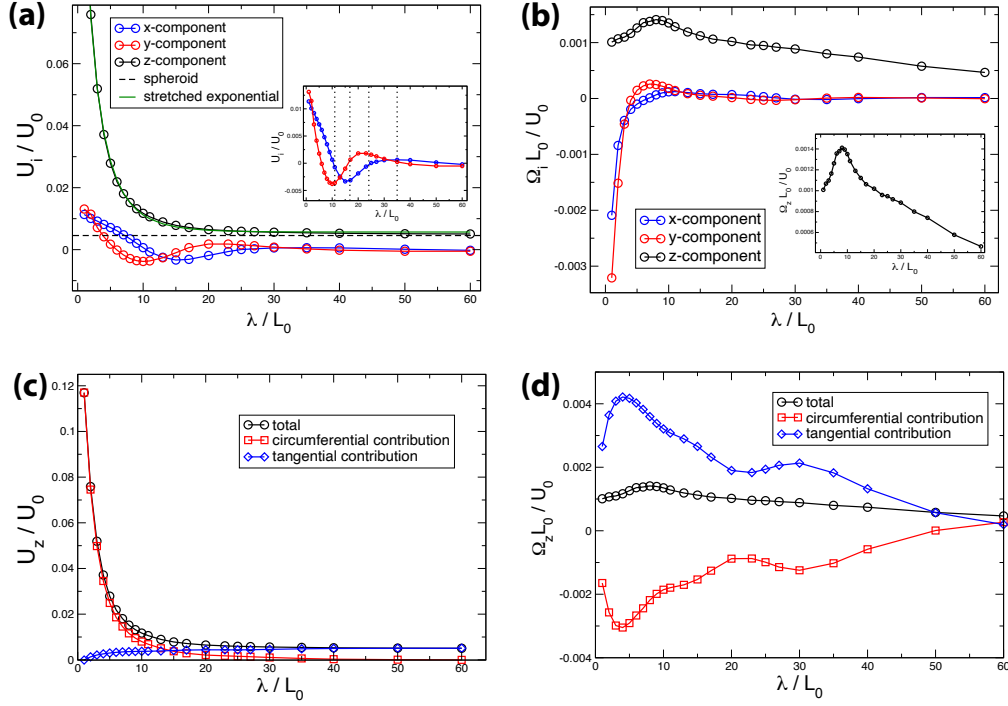


Figure 4.5: (a) Components of the translational velocity \mathbf{U} of a lengthwise Janus particle as a function of pitch λ and parameters r , \mathcal{L} , and R the same as in figure 4.3. In the main figure, the dashed line shows the value of U_z for a spheroidal particle with major axis diameter \mathcal{L} and minor axis diameter $2r$, as determined from [99]. The green curve shows a stretched exponential fit to U_z . In the inset, the dashed lines indicate values of λ for which the number of turns is a half-integer. (b) Components of the angular velocity $\mathbf{\Omega}$ of a lengthwise Janus particle as a function of pitch λ and other parameters the same as in figure 4.3. The inset shows the peak in Ω_z . (c) The contributions of circumferential and tangential concentration gradients to U_z as a function of λ . (d) The contributions of circumferential and tangential concentration gradients to Ω_z as a function of λ .

from regions of high concentration. For $\lambda/L_0 \gg 1$, U_z asymptotes to a constant value, since the filament geometry approaches the limit of a straight cylinder with hemispherical ends. For comparison, we plotted the velocity of a spheroidal particle with major axis diameter \mathcal{L} and minor axis diameter $2r$ (dashed line), obtained from [99]. The asymptotic value and the velocity of the spheroid are comparable, as expected. As a side note, we find that the variation of U_z with λ is captured by a stretched exponential fit.

The components U_x and U_y exhibit a decaying oscillatory behaviour as a function of λ . As expected from symmetry considerations, U_x and U_y approach zero for large λ . In the inset of figure 4.5(a), we show the oscillatory behaviour in closer detail. Hypothesizing that the oscillation is due to end effects for a finite length helix, we indicate with dashed lines the values of λ for which the number of turns N_{turns} is a half-integer. These values approximately correspond to the locations of the maxima and minima of U_x and U_y , giving credence to our hypothesis.

Now we consider the decomposition of the surface concentration gradient into circumferential and tangential components. In figure 4.5(c) and 4.5(d), we observe that the contributions of circumferential concentration gradients to U_z and Ω_z are surprisingly important. Concerning U_z , one expects that, for large pitch, i.e., for a geometry approaching that of a straight rod, tangential gradients should dominate circumferential gradients, and this is indeed the case in Fig. 4.5(c). However, we also find a crossover at intermediate pitch, and circumferential gradients are dominant at low pitch. Moreover, tangential and circumferential gradients compete with regard to rotation around the helix screw axis: tangential gradients tend to rotate the particle counter-clockwise around this axis, while circumferential gradients drive clockwise rotation (figure 4.5(d)). As a result, the angular velocity Ω_z is small. These findings suggest designing an activity profile to deliberately suppress one of the two contributions to particle motion.

The significance of circumferential gradients for low pitch helices additionally has impact on the flow field in the vicinity of the particle. In Fig. 4.6, we show streamlines (obtained in a stationary frame) in the vicinity of helices with small and large pitch. For the large pitch helix, the flow field is only weakly perturbed from being axisymmetric. A stagnation point is identifiable near the middle of the active side of the particle. Noting that fluid is drawn into the poles of the particle and expelled from the sides, we expect that the particle is a hydrodynamic “puller.” For the small pitch helix, in contrast, the structure of streamlines is much more complex. Streamlines can wrap around the helix surface over and over, owing to the strong circumferential flows. However, a stagnation point and a puller-like structure of streamlines in the far-field are still recognizable.

As an additional note, from the peak in R_{33} in Fig. 4.3(b), one might expect a corresponding minimum in U_z at the same value of λ . However, in Fig. 4.5(a), we observe monotonic decay of U_z with λ . To resolve this apparent paradox, we note that in solving Eq. 4.10, we effectively multiply both sides of the equation by the inverse of the resistance matrix, i.e., the mobility matrix $M \equiv R^{-1}$. The extrema of the mobility matrix components may not appear at the same λ as the extrema of the resistance matrix. Moreover, the components of the

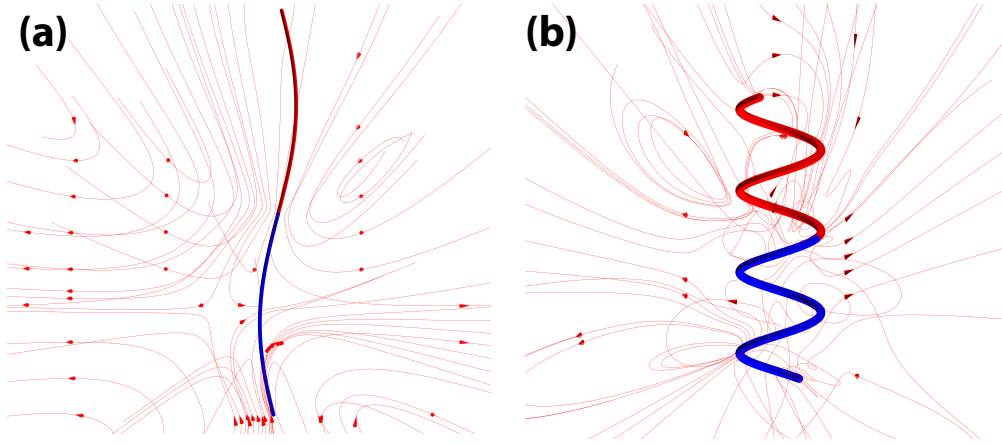


Figure 4.6: Streamlines (obtained in the stationary frame) of flow in the vicinity of a helix with (a) large pitch ($\lambda/L_0 = 60$) and (b) small pitch ($\lambda/L_0 = 5$).

right-hand side vector \mathbf{b} will also vary with λ . In Fig. 4.7(a) and (b), we show the entries of the third row of the mobility matrix. The diagonal entry M_{33} clearly dominates the third row, which determines U_z . Moreover, M_{33} is approximately flat over a broad range of λ/L_0 , and exhibits only a very shallow minimum at $\lambda/L_0 \approx 13$. This finding permits the approximation shown in Fig. 4.7(c). Taking $6\pi/80 \approx 0.236$ as a characteristic value of the flat region of Fig. 4.7(b), we approximate U_z/U_0 as $b_3/80F_0$, obtaining good agreement with the complete calculation. Thus, translation along the axis is largely determined by the z-component of the effective “force” \mathbf{b} , and coupling to other modes of motion is negligible. Moreover, the variation of U_z with λ is determined, for most λ , by the variation of b_3 with λ . In Fig. 4.7(d), we show the variation of the components of \mathbf{b} as a function of λ for the lengthwise Janus particle. It can be observed that the dependence of b_3 on λ resembles the dependence of U_z on λ .

4.4.3 “z-wise” Janus particle

We now consider the “z-wise” Janus particle (figure 4.8(a)). For this particle, one can expect circumferential gradients to be strong, while tangential gradients should be weak by symmetry of the activity profile along the contour. These expectations are borne out by our numerical calculations of the concentration, shown in figure 4.8(b) and figure 4.8(c). In particular, we note that the broad width of the grey area in figure 4.8(c) for fixed s , at most values of s , which indicates strong circumferential gradients. Additionally, the circumferentially averaged concentration (red curve, obtained by SBT) is fairly flat, except for the helix ends, indicating that tangential gradients are small.

Turning to the results for the velocity, we find that the particle has strong rotation around the screw axis, i.e., the z-axis, while rotation around the perpendicular axes is negligible (figure 4.9(b)). This is useful for applications – the particle will show strong directed motion along the screw axis direction, and will not tumble haphazardly. Concerning the decomposition into tangential and circumferential contributions, we find that our expectations are confirmed

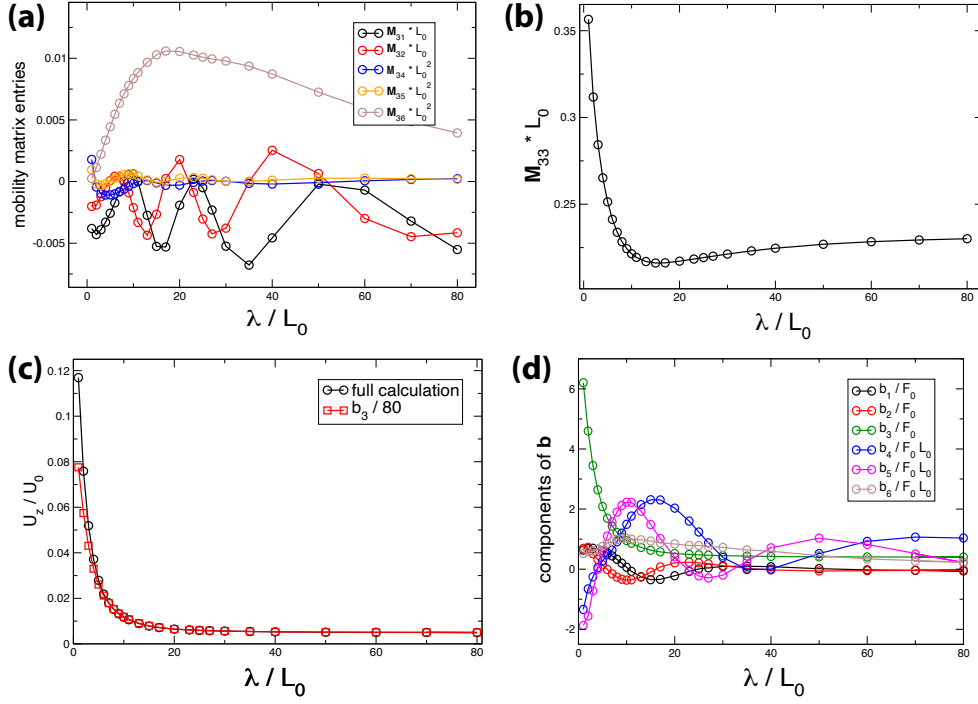


Figure 4.7: (a) Off-diagonal entries of the third row of the mobility tensor M as a function of pitch λ , and other parameters as given in Fig. 4.3. (b) Mobility tensor component M_{33} as a function of pitch λ . Note the difference in scale from (a); the diagonal entry dominates the third row of M . (c) Translational velocity component along the helix axis U_z for a lengthwise Janus activity profile as a function of pitch (all other parameters are the same as in Fig. 4.5). The full calculation that takes into account all components of M and the right-hand side vector \mathbf{b} shows good agreement with an approximate solution obtained as $b_3/80$, where $1/80$ is chosen as a characteristic value of the “flat” part of the curve in (b). (d) Components of the right-hand side vector \mathbf{b} as a function of pitch λ for the lengthwise Janus particle.

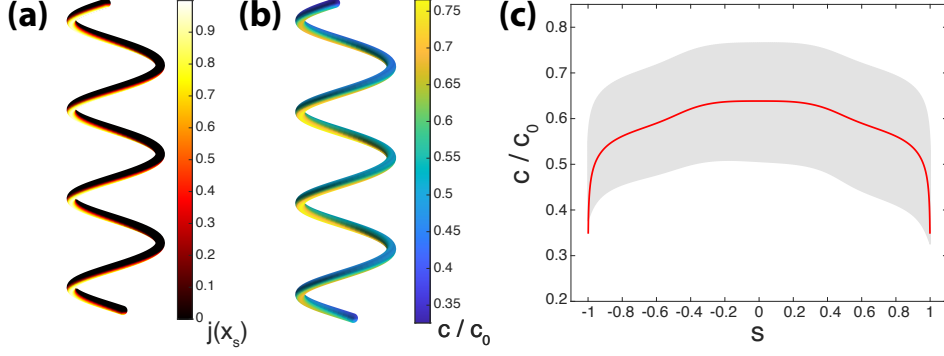


Figure 4.8: (a) Dimensionless catalytic activity $j(\mathbf{x}_s)$ on the surface of a z-wise Janus particle with $\lambda/L_0 = 5$ and parameters r , \mathcal{L} , and R the same as in figure 4.3. (b) Three-dimensional plot of the concentration c on the surface of the particle. (c) Concentration with respect to the tangential position s . The shaded grey area shows the range of values that were obtained for c for a given s and various circumferential angles ϕ (not shown). The solid curve is a theoretical expression for the circumferentially averaged concentration obtained with slender body theory.

(figure 4.9(c) and (d)).

4.4.4 “Inside-outside” Janus particle

Finally, we consider the “inside-out” Janus particle. As one might expect, the circumferential variations in the concentration field c are substantial (see figure 4.10 (a)), and dominate the tangential variations. Following the slender body approach in 4.4.5, we can identify three distinct factors that contribute to the concentration profile. First, the circumferentially averaged concentration field is again very well predicted by the circumferentially averaged SBT (red line). First, the circumferentially averaged SBT (red line) again lies very well within the variation of the concentration field (grey area). It also matches the mean concentration field (blue line) to a high degree, despite only accounting for the averaged catalytic activity (see section 4.4.5). As expected, it is symmetric with respect to s . However, for this activity profile, two additional factors lead to circumferential variation (for a given s) of the concentration profile (see figure 4.10 (b)).

The second factor is the circumferential variation of the activity profile, i.e., the dependence of $j(\mathbf{x}_s)$ on ϕ . In the slender body approach, this factor can be accounted for in the construction of the inner solution. Specifically, we solve for the concentration field around an infinite, half-covered cylinder with translational symmetry via a series expansion. Therefore, this factor be reduced to and solved in two dimensions. The third factor is, as before, polarization of the surface concentration at s induced by the ambient concentration gradient created by the rest of the particle. Concerning these second and third factors, the contribution from the local catalytic activity (i.e., the second factor) is dominant, and ensures that the minimal concentration is always close to the centre of the inert region ($\phi \approx 0$) and the maximum on the opposite side ($\phi \approx \pm\pi$). Away from the centre ($s = 0$) of the helix (represented by black

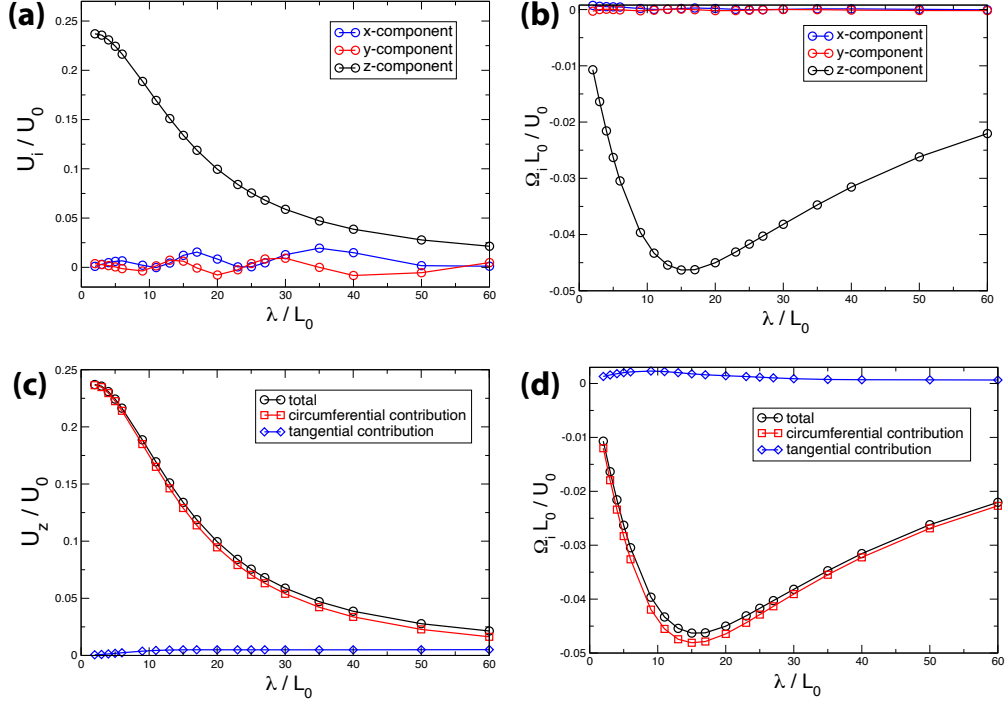


Figure 4.9: (a) Components of the translational velocity \mathbf{U} of a z-wise Janus particle as a function of pitch λ , with parameters r , \mathcal{L} , and R the same as in figure 4.3. (b) Components of the angular velocity $\mathbf{\Omega}$. (c) The z-component U_z of the particle translational velocity as a function of pitch, as well as the contributions of circumferential and tangential concentration gradients to U_z . (d) The z-component Ω_z of the particle angular velocity as a function of pitch, as well as the contributions of circumferential and tangential concentration gradients.

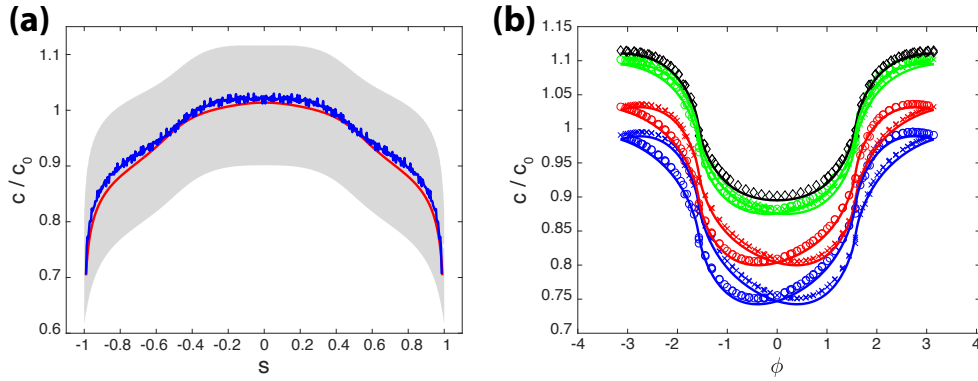


Figure 4.10: (a) Concentration with respect to the tangential position s for an “inside-out” Janus helix. The shaded grey area shows the range of values that were obtained for c for a given s and various circumferential angles ϕ (not shown), and the blue line shows the mean value as a function of s . The solid curve is a theoretical expression for the circumferentially averaged concentration obtained with slender body theory. (b) Variation of concentration c as a function of circumferential angle ϕ for various values of s . The values of s are as follows: blue circles, $s = -0.85$; blue crosses, $s = 0.85$; red circles, $s = -0.65$; red crosses, $s = 0.65$; green circles, $s = -0.35$; green crosses, $s = 0.35$; black diamonds, $s = 0$.

diamonds in figure 4.10 (b)), the average concentration drops, and a circumferential asymmetry develops. This circumferential asymmetry is due to the third factor, i.e., the dipolar polarization introduced by the rest of the particle. Due to the symmetry of the activity profile along the contour, the disturbances at locations s and $-s$ are mirror symmetric with respect to $s = 0$. The asymmetry becomes more significant further away from the center.

Analyzing the velocity components for “inside-outside” Janus helices (see figure 4.11) we immediately see that, due to their symmetric design, both the U_z and Ω_z components vanish. All other components exhibit a decaying oscillation with respect to the total number of turns N in the helix. These particles have completely different trajectories compared to the first two examples and are not propelled in the direction of the screw axis. For both the translation and the rotational velocity, the minima and maxima in the x -component lead the corresponding maxima and minima in the y -component by a quarter turn. This can again be understood by our hypothesis that the movement in xy plane is mainly due to end effects. In order to illustrate this, we will take a closer look at the U_y component. Recall that our helices are constructed by fixing the bottom end to point in the y direction; the tangential direction of top end depends on the number of turns N and other parameters. For an integer number of turns, the ends point in opposite (y and $-y$) directions and balance each other. Upon increasing N , the top ($s = 1$) rotates by an angle $\gamma = 2\pi \bmod (N, 1)$ and increases its y -component $\hat{\mathbf{t}}_h(s=1) \cdot \hat{\mathbf{y}} \propto -\cos(\gamma)$, while the bottom end stays in place. At the next half integer turn, the top and the bottom end are pointing in the same direction, i.e., y , and the overall velocity U_y reaches a maximum. Further growth of the helix causes the top contribution to shrink, until the two balance each other again at the next full turn. Note that U_y is never negative because of the construction of the helix. For the other three non-zero velocities, U_x , Ω_x and Ω_y , the periodicity can be explained similarly. When inspecting U_x more closely, we see that these end effects do not entirely account for the variation of the velocity, e.g., U_x is not exactly 0 at $N = 1, 2, 3, 4, 5$. This offset is caused by the finite size of the body and can be understood best by examining the details of the $N = 1$ helix. The centre of this helix ($s = 0$) lies on the x -axis, and circumferential variations in the concentration field at $s = 0$ can only induce movement in the x -direction. For any off-center values $s_0 \neq 0$, the helix can have y -contributions. However, due to the symmetry in the concentration field, the y -contribution at $s = -s_0$ has to be of equal magnitude and opposite sign. Thus, the two cancel each other out, and there is no movement in the y -direction for helices with an integer number of turns. This is not true for the x -components. The $s = 0$ contribution to U_x is counteracted by the points $\pm s_0 = \pm \frac{1}{4N}$ half a turn up and down the helix axis, which have normal vectors $\hat{\mathbf{n}}_h(s_0) = \hat{\mathbf{n}}_h(-s_0)$ in the opposite direction, i.e., $\hat{\mathbf{n}}_h(s_0) = -\hat{\mathbf{n}}_h(0)$. However, the finite size of the helix causes the concentration field to decrease away from the helix centre towards the ends. The two contributions at $\pm s_0$ do not add up to the same magnitude as at the center, and the particle has a net velocity in the x -direction. In summary, we consider that a finite size effect is responsible for the slight shift of the zeroes of U_x , as a function of N , away from integer values of N (figure 4.11(c)).

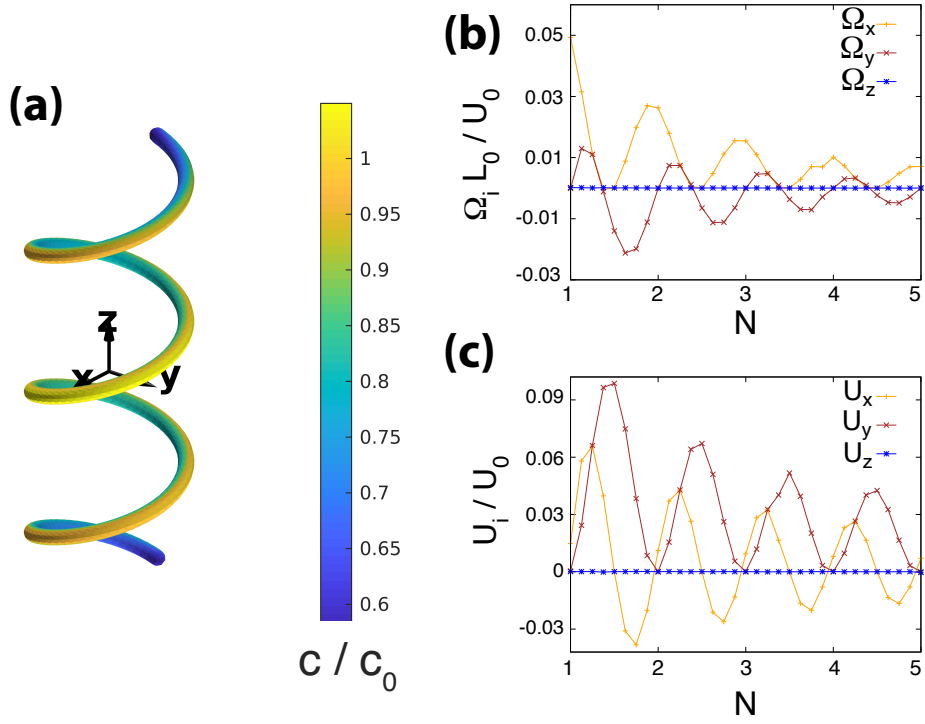


Figure 4.11: (a) Three-dimensional plot of the concentration c on the surface of the “inside-outside” Janus helix. (b) Components of the transitional velocity \mathbf{U} as a function of the number of turns N and pitch $\lambda/L_0 = 5$, contour radius $R/L_0 = 2.5$, and filament radius $r_0/L_0 = 0.265$. (c) Components of the and angular velocity $\mathbf{\Omega}$ as a function of the number of turns N .

4.4.5 Slender body theory for helix surface concentration

In this section, we introduce an analytical approximation that relies on the “slenderness” parameter $\epsilon \equiv 2r_0/\mathcal{L}$ being very small, i.e., $\epsilon \ll 1$. We neglect the role of the hemispherical caps. Our treatment is influenced by the work in [99] and [217] on slender, *axisymmetric* self-phoretic particles, as well as [121] on the hydrodynamic resistance of slender bodies. In particular, our presentation in Section 4.4.5 closely follows the formal manipulations and asymptotic mathematics of [121]. It can be regarded as transposing some of their results to the context of Laplace’s equation and active colloids. Our presentation in the subsequent section, in contrast, is intended as a phenomenological, physically motivated attempt to model circumferential variations of concentration. It is developed on the basis of a physical hypothesis and a physical analogy to potential flow.

We note that recently, a systematic and rigorous derivation of slender body theory for a chemically active filament was published by [116], who work from the alternative basis provided by [127]. One advantage of working from that basis is that it facilitates consideration of circumferential variation of the surface stress. Thus, [116] are able to (numerically) calculate particle velocities in the framework of SBT; in that sense, their formulation of SBT is complete. Here, we restrict our attention to calculation of the concentration field. Additionally, we make no pretense to the level of formal rigor and systematic mathematical development provided in [116]. However, our brief treatment may provide an accessible point of entry into SBT for some readers. Additionally, by being grounded in a physical model, it sheds light on underlying physical mechanisms.

For the slender body analysis, the governing equations for the concentration will be non-dimensionalized using a characteristic length $L \equiv \mathcal{L}/2$ (i.e., the half-length of the particle) and characteristic concentration $C_0 \equiv \kappa r_0/D$, distinct from the previously defined c_0 . Accordingly, the equations become:

$$\nabla^2 c = 0 \tag{4.22}$$

and

$$\hat{\mathbf{n}} \cdot \nabla c = -j(s)/\epsilon, \tag{4.23}$$

with $c(|\mathbf{x}| \rightarrow \infty) = 0$, where c and the gradient operator are understood to be dimensionless. We will use this non-dimensionalization for the rest of Section 4.4.5.

Circumferentially averaged concentration

Using asymptotic expansions, the solution for $c(\mathbf{x})$ can be separated into “inner” and “outer” regions in the limit $\epsilon \rightarrow 0$. The outer region is defined such that, for a position \mathbf{x} in the outer region, the distance r to the closest point on the helix backbone is $\mathcal{O}(1)$, i.e., much larger than ϵ in the limit $\epsilon \rightarrow 0$. In this region, we can represent the concentration as being due to a

distribution of sources $\alpha(s)$ along an infinitesimally thin space curve:

$$c_{\text{out}}(\mathbf{x}) = \int_{-1}^1 \frac{\alpha(s')}{|\mathbf{x} - \mathbf{x}_h(s')|} ds' \quad (4.24)$$

In the inner region, where r is $O(\epsilon)$ as $\epsilon \rightarrow 0$, the particle resembles an infinitely long cylinder. Here, we introduce the stretched coordinate $\rho \equiv r/\epsilon$. Following the logic of [217], we integrate Eq. 4.22 (assuming an effectively two-dimensional problem) and impose the boundary condition in Eq. 4.23 to obtain

$$c_{\text{in}}(\rho, s) = C(s; \epsilon) - j(s) \ln \rho, \quad (4.25)$$

where the function $C(s; \epsilon)$ will be determined by matching to the outer solution. Physically, the logarithmic term can be interpreted as the (two-dimensional) concentration field due to an infinitely long and uniformly active cylinder. The function $C(s; \epsilon)$ is an “integration constant” for the contour position s .

Our next task is to perform asymptotic matching between the inner region and outer region in the limit $\epsilon \rightarrow 0$ to obtain $C(s; \epsilon)$ and $\alpha(s)$. Concerning the outer solution, we consider a position $\mathbf{x} = \mathbf{x}_h(s) + \mathbf{r}$, with $\mathbf{r} \cdot \hat{\mathbf{t}}(s) = 0$ (i.e., \mathbf{x} is in the plane defined by the particle cross-section at s) and $|\mathbf{r}| = r$. We wish to examine the limits $\mathbf{r} \rightarrow 0$ as $\epsilon \rightarrow 0$. We expect that the concentration $c_{\text{out}}(\mathbf{r}, s) \equiv c_{\text{out}}(\mathbf{x}_h(s) + \mathbf{r})$ is singular as $\mathbf{r} \rightarrow 0$, since the domain of the integral includes s itself, and since the evaluation point \mathbf{x} approaches the helix backbone as $\mathbf{r} \rightarrow 0$.

In the following, we closely follow the procedure in Appendix of [121]. Our aim is to isolate the singularity, i.e., move it out of the integral, and evaluate it analytically. First, we first change the integration variable $q = s' - s$ in Eq. 4.24:

$$c_{\text{out}}(\mathbf{x}) = \int_{-(1+s)}^{1+s} \frac{\alpha(s+q)}{|\mathbf{x}_h(s) + \mathbf{r} - \mathbf{x}_h(s+q)|} dq. \quad (4.26)$$

We define $\mathbf{R}_0 \equiv \mathbf{x}_h(s) - \mathbf{x}_h(s+q)$, with $R_0 \equiv |\mathbf{R}_0|$, as well as

$$R^2 \equiv |\mathbf{R}_0 + \mathbf{r}|^2 = R_0^2 + 2\mathbf{r} \cdot \mathbf{R}_0 + r^2. \quad (4.27)$$

We also define the quantity $K^2(\mathbf{R}_0, \mathbf{r})$ by $R^2 \equiv r^2 + K^2 q^2$. The usefulness of K will become apparent shortly, when discussing the limit $q \rightarrow 0$. The integral can be rewritten as

$$c_{\text{out}}(\mathbf{x}) = \int_{-(1+s)}^{1+s} \frac{\alpha(s+q)}{R} dq = \int_{-(1+s)}^{1+s} \frac{\alpha(s+q)}{\sqrt{r^2 + K^2 q^2}} dq. \quad (4.28)$$

For small q , we can expand \mathbf{R}_0 as follows:

$$\mathbf{R}_0 = \left(\frac{\partial \mathbf{x}_h}{\partial s} \right)^2 q^2 - \left(\frac{\partial^2 \mathbf{x}_h}{\partial s^2} \cdot \mathbf{r} \right) q^2 + O(q^3). \quad (4.29)$$

The vector $\mathbf{i} \equiv \frac{\partial \mathbf{x}_h}{\partial s}$ is tangent to the backbone and, since length is non-dimensionalized by $\mathcal{L}/2$ in this section, has unit length. We also define $\mathbf{i}_s \equiv \frac{\partial^2 \mathbf{x}_h}{\partial s^2}$, giving

$$\mathbf{R}_0 = (1 - \mathbf{r} \cdot \mathbf{i}_s) q^2 + O(q^3), \quad (4.30)$$

and

$$K^2 = 1 - \mathbf{r} \cdot \mathbf{i}_s + O(q). \quad (4.31)$$

From Eq. 4.28 and Eq. 4.31, it is apparent that, for small r and q , the singularity in the integral has the form $1/\sqrt{r^2 + q^2}$. We attempt to isolate it from the integral as follows:

$$c_{\text{out}}(\mathbf{x}) = \int_{-(1+s)}^{1+s} \left[\frac{\alpha(s+q)}{\sqrt{r^2 + K^2 q^2}} - \frac{\alpha(s)}{\sqrt{r^2 + q^2}} \right] dq + \int_{-(1+s)}^{1+s} \frac{\alpha(s)}{\sqrt{r^2 + q^2}} dq. \quad (4.32)$$

For $r = 0$, the first integral is finite. This can be shown by putting the two terms in the integrand over a common denominator q and expanding $\alpha(s+q)$ with respect to q , allowing for cancellation of the denominator. Interestingly, the numerator of the second integral has no dependence on q . Thus, the second integral can be evaluated analytically:

$$\int_0^t \frac{dq}{\sqrt{r^2 + q^2}} = \left[\ln \left(\sqrt{t^2 + r^2} + t \right) - \ln r \right]. \quad (4.33)$$

We thus obtain

$$\lim_{r \rightarrow 0} c_{\text{out}}(\mathbf{r}, s) = 2\alpha(s) \ln \left(\frac{1}{r} \right) + \int_{-(1+s)}^{1-s} \left[\frac{\alpha(s+q)}{|\mathbf{x}_h(s+q) - \mathbf{x}_h(s)|} - \frac{\alpha(s)}{|q|} \right] dq + \alpha(s) \ln[4(1+s)(1-s)], \quad (4.34)$$

or equivalently

$$\lim_{r \rightarrow 0} c_{\text{out}}(\mathbf{r}, s) = 2\alpha(s) \ln \left(\frac{2}{r} \right) + \int_{-(1+s)}^{1-s} \left[\frac{\alpha(s+q)}{|\mathbf{x}_h(s+q) - \mathbf{x}_h(s)|} - \frac{\alpha(s)}{|q|} \right] dq + \alpha(s) \ln[(1+s)(1-s)], \quad (4.35)$$

which exposes the logarithmic singularity. Note that equation 4.35 does not capture circumferential variations of concentration. Secondly, note that the “nonlocal” integral contains information about the helical shape of the backbone. In asymptotic matching, we determine the unknown $\alpha(s)$ and $C(s; \epsilon)$ from

$$\lim_{r \rightarrow 0} c_{\text{out}}(\mathbf{r}, s) = \lim_{\rho \rightarrow \infty} c_{\text{in}}(\rho, s) \quad (4.36)$$

as $\epsilon \rightarrow 0$. Matching Eqs. 4.25 and 4.35, we find

$$\alpha(s) = \frac{1}{2} j(s), \quad (4.37)$$

$$C(s; \epsilon) = j(s) \ln \left(\frac{2}{\epsilon} \right) + C_0(s), \quad (4.38)$$

and

$$C_o(s) \equiv \frac{1}{2} \int_{-(1+s)}^{1-s} \left[\frac{j(s+q)}{|\mathbf{x}_h(s+q) - \mathbf{x}_h(s)|} - \frac{j(s)}{|q|} \right] dq + \frac{1}{2} j(s) \ln[(1+s)(1-s)]. \quad (4.39)$$

Using Eq. 4.25 and associated expressions evaluated at the helix surface $r = \epsilon$ (recall the non-dimensionalization of length in this section), we plot the red curve in figure 4.4(a) (reverting to the previous characteristic concentration c_0 in the figure). This curve runs through the scattered data points very well; however, it cannot account for the scatter, because equation 4.39 has no ϕ dependence. (Recall that the scatter represents the range of the variation of concentration in the angle ϕ for a given value of s .)

Circumferential variation of concentration

The slender body analysis in Section 4.4.5 gave an expression for concentration that had no dependence on ϕ , and which can therefore be regarded as a circumferentially averaged concentration. This expression is useful for considering variations of concentration with s , i.e., the component of the surface gradient in the $\hat{\mathbf{t}}$ direction. However, the circumferential component of the surface concentration gradient could also contribute to self-propulsion, as discussed above.

Moreover, the numerical results clearly show a circumferential variation of concentration. In Figure 4.4(c), we show the concentration on the surface of the lengthwise Janus particle, obtained via the BEM, as a function of ϕ for various values of s . (Specifically, for each s , we consider values of c on the surface for numerical mesh points within a small neighborhood of s .) By inspection, there seems to be a sinusoidal dependence on ϕ , with the phase depending on s . For s within the active region, i.e., $s < 0$, the maximum in concentration is around $\phi = 0$ and the minimum at $\phi = \pm\pi$, indicating that the circumferential variation in concentration is largely variation between the “inside” and “outside” of the helix. For the inert region $s > 0$, the maximum is shifted to approximately -90° . This indicates that the circumferential variation of concentration is dominated by $\hat{\mathbf{b}}_h$. Note that $\hat{\mathbf{b}}_h$ has a $\hat{\mathbf{z}}$ component and $\hat{\mathbf{n}}_h$ does not; since the maximum is at -90° , the high concentration region is oriented towards the active side of the particle, i.e., towards $-\hat{\mathbf{z}}$.

Based on these observations, we make the following hypothesis: at a point s , the circumferential variation of concentration is due to polarization by the “external” concentration gradient ∇c , i.e., the concentration gradient created by catalytic activity on other points of the helix. For instance, this would explain why, in the inert region of the helix, the high concentration region is oriented towards the active side of the helix. We can make an analogy with the classical problem of an infinite cylinder in uniform, two-dimensional potential flow, shown schematically in figure 4.4(d). On the basis of this analogy and the solution to that classical problem, we expect that the amplitude of the sinusoidal variation at s to be *twice* the magnitude of the component of external gradient in the plane defined by $\hat{\mathbf{n}}_h$ and $\hat{\mathbf{b}}_h$, i.e., $(\mathbf{1} - \hat{\mathbf{t}}_h \hat{\mathbf{t}}_h) \cdot \nabla c$, evaluated at the centerline position $\mathbf{x}_h(s)$. Secondly, the phase of sinusoidal

variation will be such that, for a particular s , the vector between the concentration minimum and concentration maximum (defined in three-dimensional space) will be aligned with the in-plane component of ∇c . Our analogy receives further motivation when we consider that we had regarded the tube surface as a “quasi-infinite cylinder” when solving for the inner concentration in the previous section.

Based on these ideas, we proceed to consideration of ∇c for a lengthwise Janus helix. For a point $s > 0$ in the inert region, we can simply write

$$\nabla c(\mathbf{x}_h) = -\frac{1}{2} \int_{-1}^1 \frac{j(s') [\mathbf{x}_h(s) - \mathbf{x}_h(s')] ds'}{|\mathbf{x}_h(s) - \mathbf{x}_h(s')|^3} \quad (4.40)$$

or

$$\nabla c(\mathbf{x}_h) = -\frac{1}{2} \int_{-1}^0 \frac{[\mathbf{x}_h(s) - \mathbf{x}_h(s')] ds'}{|\mathbf{x}_h(s) - \mathbf{x}_h(s')|^3}. \quad (4.41)$$

For the second expression, we do not have any issues with integrating through a singularity, as $s > 0$ in inert region. Specifically, we are interested in the normal and binormal components, since we need to know the orientation of the external gradient with respect to the local value of \hat{n}_h . We obtain:

$$\nabla c(\mathbf{x}_h) \cdot \hat{n}_h = -\frac{1}{2} \int_{-1}^0 \frac{(\mathbf{x}_h(s) - \mathbf{x}_h(s')) \cdot \hat{n}_h(s) ds'}{|\mathbf{x}_h(s) - \mathbf{x}_h(s')|^3}, \quad (4.42)$$

$$\nabla c(\mathbf{x}_h) \cdot \hat{b}_h = -\frac{1}{2} \int_{-1}^0 \frac{(\mathbf{x}_h(s) - \mathbf{x}_h(s')) \cdot \hat{b}_h(s) ds'}{|\mathbf{x}_h(s) - \mathbf{x}_h(s')|^3}. \quad (4.43)$$

We find the amplitude A of the sinusoidal variation as

$$A = 2 |\nabla c(\mathbf{x}_h) \cdot \hat{b}_h + \nabla c(\mathbf{x}_h) \cdot \hat{n}_h|, \quad (4.44)$$

and the phase ψ as

$$\psi = \arg \left(\nabla c(\mathbf{x}_h) \cdot \hat{n}_h + i \nabla c(\mathbf{x}_h) \cdot \hat{b}_h(s) \right). \quad (4.45)$$

Numerically integrating Eqs. 4.42 and 4.43, we obtain the theoretical curves (solid lines) for the inert region of the particle (corresponding to the cross symbols) in figure 4.4(c).

For the active region of the particle ($s < 0$), the line integral in equation 4.40 has to been handled with care, since there is a singularity at $s = s'$. As in Sect. 4.4.5, we follow the procedure in Appendix A of [121] (see Eq. A1 and Eq. 2 of that work). Via similar manipulations, we can isolate the singularities, obtaining:

$$\begin{aligned} \nabla c(\mathbf{x}_h(s)) \cdot \hat{n}_h = & -\frac{1}{2} \left[(\hat{n}_h \cdot \mathbf{i}_s) \log \epsilon - \frac{1}{2} (\hat{n}_h \cdot \mathbf{i}_s) \log[(1-s)(1+s)] + \right. \\ & \left. \hat{n}_h(s) \cdot \left(\int_{-(1+s)}^{1-s} \left[\frac{\mathbf{R}}{R^3} - \frac{-\mathbf{i}(s)q + [-\frac{1}{2}\mathbf{i}_s(s) - j_s(s)\mathbf{i}(s)] q^2}{q^3} \right] dq \right) \right] \end{aligned} \quad (4.46)$$

and

$$\nabla c(\mathbf{x}_h(s)) \cdot \hat{\mathbf{b}}_h = -\frac{1}{2} \hat{\mathbf{b}}_h(s) \cdot \left(\int_{-(1+s)}^{1-s} \left[\frac{\mathbf{R}}{R^3} - \frac{-\mathbf{i}(s)q + \left[-\frac{1}{2}\mathbf{i}_s(s) - j_s(s)\mathbf{i}(s)\right] q^2}{q^3} \right] dq \right) \quad (4.47)$$

on the surface of the particle. Here, $\mathbf{R} \equiv \mathbf{x}_h(s) - \mathbf{x}_h(s+q)$; quantities with s subscripts indicate partial differentiation with respect to s ; and the quantity $\mathbf{i} \equiv \frac{\partial \mathbf{x}_h}{\partial s}$, i.e., \mathbf{i} is tangent to the contour and \mathbf{i}_s is normal to it. The integrals can be evaluated numerically.

These expressions are valid over the whole contour of the particle, and in the inert region return the same results as equations 4.42 and 4.43. In figure 4.4(c), we plot the theoretical curves in the active region (circle symbols and diamond symbols). We obtain generally good agreement with the numerical data. Note that some of the disagreement is because the slender body expressions for the mean / circumferentially averaged concentration tend to underestimate c (possibly because these expressions neglect the catalytic endcap); if the theoretical curves were shifted upward, better agreement would be obtained. The greatest disagreement is for s close to $s = 0$, i.e., the interface between the active and inert halves of the particle, but the theoretical curves still capture the general shape here.

Including circumferential variation of the activity profile

For a particle that has an activity profile that depends on ϕ , like the “inside-outside” Janus particle, the initial approach to obtain the circumferentially averaged concentration does not change significantly. Using the circumferentially-averaged activity profile $\bar{j}(s) \equiv \frac{1}{2\pi} \int_0^{2\pi} j(s, \phi) d\phi$ instead of $j(s)$ in the framework of Section 4.4.5 is sufficient.

However, to obtain the circumferential variation of the concentration, additional terms in the inner solution are needed. In particular, for the “inside-outside” Janus particle the azimuthal deviation from the average needs to be accounted for. One can achieve this by solving Laplace’s equation in 2D for the boundary condition

$$\hat{\mathbf{n}} \cdot \nabla c(\mathbf{x}) \Big|_{r=r_0} = \frac{\partial c}{\partial r} \Big|_{r=r_0} = - \left(\Theta(\phi + \pi/2) \Theta(-\phi - \pi/2) - \frac{1}{2} \right) / \epsilon. \quad (4.48)$$

Essentially, one must solve for the concentration around a Janus cylinder with translational symmetry in the z direction. The parameters a_n and b_n in the multipole solution to Laplace’s equation in 2D,

$$c(r, \theta) = a_0 \log \left(\frac{1}{r} \right) + \sum_{n=1}^{\infty} \frac{a_n \cos(n\theta) + b_n \sin(n\theta)}{r^n}, \quad (4.49)$$

can be determined by applying the boundary conditions. One can substitute equation 4.49 into 4.48, substitute the step function $\Theta(\phi)$ by its Fourier series $\sum_n \beta_n \sin(n\phi)$ with $\beta_n \equiv \frac{-1}{n\pi} (\cos(n\pi) - 1)$, and match terms to determine a_n and b_n .

4.5 Conclusions

Overall, the framework developed here provides a set of analytical and numerical tools for modeling self-phoretic helical particles. In particular, we outline methods to solve the two principal subproblems: diffusion of the product chemical and hydrodynamic reaction to the resulting slip velocity.

By including three-dimensional finite size effects, our extended slender body theory captures both tangential and circumferential variations in the concentration field surrounding the particle. We find that both the magnitude $|c_{\max} - c_{\min}|$ and the phase $\phi_{\max/\min}$ of these (quasi-sinusoidal) variations depend on the geometric and chemical parameters of the helix (see Sections 4.4.2 and 4.4.4). In both cases, our analytical results are in line with numerical calculations done with the boundary element method (BEM). The BEM results for the second subproblem also show good agreement with previously published numerical and experimental data (Section 4.4.1). Although our development of SBT is limited to the chemical concentration field, the spatial variation of concentration near a catalytically active particle is of broad interest in active colloids (e.g., for understanding the phoretic motion of tracer particles [11] and chemical kinetics [185]).

We recovered the intriguing recent finding of [116] that circumferential variations in the concentration field can lead to circumferential slip. This is not seen for simpler geometries. A systematic analysis of contributions to particle motion revealed a natural division of self-phoretic helices into three categories: tangentially driven, circumferentially driven, and intermediate. The first group mostly includes helices with large pitches, which closely resemble straight rods, while the second group mostly includes helices with very small pitches or activity profiles that vary circumferentially. Furthermore, for the latter two groups we can obtain significant movement in the plane orthogonal to the helix screw axis. This perpendicular motion is mainly driven by the ends of the helix (see Sections 4.4.2 and 4.4.4). However, the decreasing concentration away from the centre for finite-sized helices can introduce disturbances. Sections of the helix with opposite normal vectors (defined with respect to the helix contour) do not perfectly balance each other, allowing for net movement even if the end pieces point in opposite directions. Overall, awareness of the groups allows selection of one of the groups by design, through judicious choice of the catalyst coverage.

Self-phoretic helices have fewer inherent restrictions to their movement in all six degrees of freedom than most other particles of this type, while still being a well known and easy to understand geometry. Furthermore, to radically change the movement patterns, only two parameters, pitch size and catalytic coverage, need to be controlled. This makes self-phoretic helices a prime option for many applications, such as targeted drug delivery or chemical clean-up. To fully evaluate their potential, further research is needed to answer questions such as: How do they react to confining surfaces [21, 133] and external fields, e.g., chemical gradients [192] or flows ([118, 151, 154])? How do they interact with each other, e.g., can they synchronize their rotations [124, 203]? How do geometric perturbations, such as a slow

variation of pitch λ or radius R with s , change the behaviour [257]? Can the flow field in the vicinity of a helix be engineered for cargo uptake and transport [13]?

As an outlook and stimulus for future work, we briefly speculate on motion near surfaces. We anticipate from previous work ([241]) that we may observe “sliding” steady states in which the particle axis is aligned in the plane of the surface, and “hovering” steady states in which the particle axis is aligned with the surface normal, i.e., the helix is “standing up” on the surface. In both scenarios, the particle could continuously rotate around its axis. Concerning “sliding,” translation with continuous axial rotation was observed in active helices by [78]. We anticipate that sufficient strong rotation could lead to circular trajectories, similar to those seen for *e. coli*. For “hovering” states, in which the helix center has a steady position, continuous rotation may be interesting from an applications standpoint (for development of self-powered micromachines). In particular, the results in this manuscript suggest that “hovering” may be relevant, provided that the particles are not too heavy. The flow fields for the lengthwise Janus particle have a puller-like far-field structure. and it is known that pullers tend to orient perpendicular to surfaces, i.e., adopt hovering states. Additionally, the repulsive interaction with solute assumed here would tend to drive the active side of a lengthwise Janus particle away from confining surfaces. However, both of these aspects are dependent on the surface chemistry of a particle. For instance, changing the sign of the surface mobility in this work, i.e., changing the particle/solute interaction to effective attraction, would reverse the streamlines and the direction of particle motion, i.e., make the particle an active-forward “pusher.” Moreover, a surface mobility contrast between the active and inert sides could change the pusher/puller character of the particle. These considerations suggests that an immediately fruitful direction for continuing work would be to systematically characterize the flow and concentration fields in the vicinity of a self-phoretic helix, including the pusher/puller character, as a function of geometry and surface mobility contrast. The pusher/puller character could be quantified via numerical calculation of the particle’s active stresslet. We also note that in addition to “sliding” and “hovering,” new scenarios of near-surface motion, in comparison with spheres and spheroids, could be unlocked by the non-axisymmetric shape of helices. In particular, the configuration space of a helix near a surface would be three-dimensional (defined by the height above the surface and two rotational degrees of freedom), which could lead to chaotic dynamics.

CHAPTER 5

CONSTRUCTING MICRO-CHAINS:

A STUDY OF SELF-DIFFUSIOPHORETIC TORUS-SPHERE INTERACTIONS

As a continuation of the previous project, we want to investigate the interaction between a concave shaped particle and a sphere. In this chapter a particle is defined as concave, if a line segment connecting at least two of its points is not fully contained within the particle. Due to the added complexity of having a second particle, we replace the helix with a torus. If both particles are centered on the same axis, the system regains a rotational symmetry, while still including a concave particle, which proved to be important for self-diffusiophoretic helices. The step from understanding single particle to pair and, later, multi-particle behavior is not only a natural one, but also necessary. In nature, a microorganism is rarely alone; it might need to cooperate with others, compete against them for resources, or flee from them. Similarly, artificial microswimmers, in order to have a significant effect, will need to be applied in bulk for many applications. However, this can impose new challenges; they could for instance block each other. To avoid such problems and instead facilitate a productive interaction, we need to first understand how these microswimmers interact with each other.

5.1 Introduction

Both artificial and biological microswimmers interact with their surroundings. These interactions can be divided into three classes: external fields (i.e. gravity, chemical concentration, flow field), physical objects (i.e. walls) and other microswimmers. Many interesting reactions have been discovered within these cases. For example, *e. coli* close to a wall swim in circles [132]. Self-diffusiophoretic janus particles can swim upstream [240] and against gravity [41, 87]. Clusters of active colloids can induce “superfluidity” [147]. Constraining the movement of a group of microswimmers into a chain enables them to transport or “shepherd” a much larger quantity of a substance [110].

Clusters in particular have raised a lot of interest in the active matter community [110, 189, 204, 205, 234]. Those formed by artificial microswimmers are commonly of one of two types. Either they rely on an external field or on steric interactions. Artificial microswimmers typically have rigid bodies and are more dense than water. This restricts their movement to the two dimensional plane above the wall at the bottom of their container. If two such particles collide, they can not pass through each other, and instead have to rotate out of the way. However, if the particle density is high enough, this process is too slow and instead, an additional colloid can collide into the pair and the cluster will start to grow. While these clusters are intuitive to understand, they are also limited. They have no inherent orientation or significant collective motion. Furthermore, the individual particles at the center are blocked from moving in any direction. In contrast, loosely bound clusters built by non-steric interactions, like the recently discovered arrested mobility clusters [107], show richer dynamics

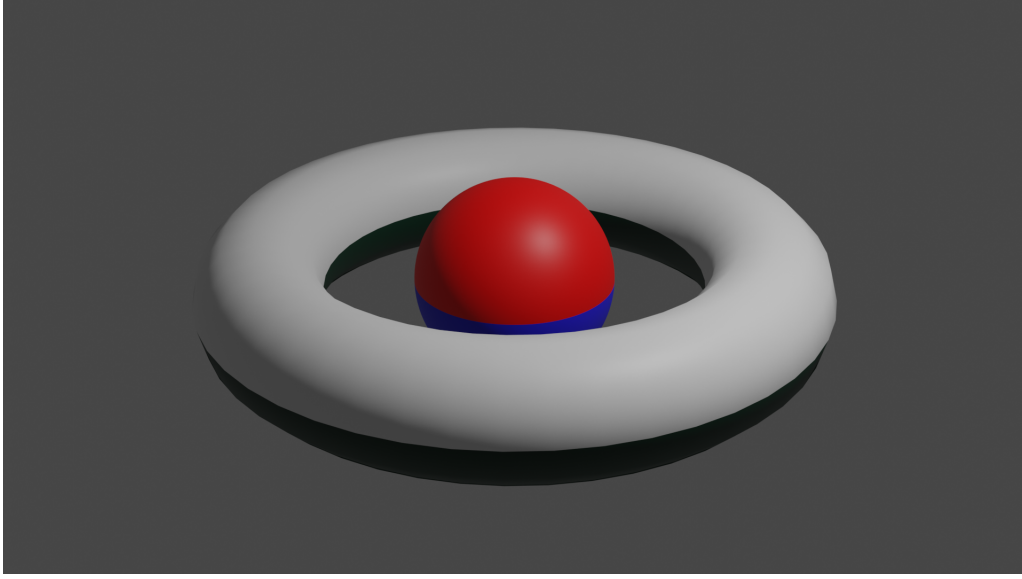


Figure 5.1: Illustration of the particle geometries. As indicated by the colors both particles can be self-diffusiophoretic, but the catalyst distribution is not limited to the shown case. Here the red and white areas indicate chemically active regions and the black and blue surfaces are inert.

and configurations. However, many of these are limited in their application by requiring an external field.

In this chapter the interaction between a self-diffusiophoretic torus and sphere is investigated. Such pairs are a promising candidate to combine the rich dynamics of non-steric interactions with a greater potential for applications. In particular, whether or not the two can move together at a fixed separation distance is of interest. A co-moving pair could be the building block for many future applications, such as a self-diffusiophoretic train transporting drug molecules to a target location.

A unique possibility for this system is also the capability for the sphere to swim completely through the torus. While this behavior is unwanted for the construction of more complex structures, it opens the fascinating possibility to sort active swimmers by their ability to do so or not.

5.2 Geometry

The chosen system to investigate the interactions between a self-diffusiophoretic torus-sphere pair consists of a single sphere of radius R and a torus with tube radius a and tube centerline radius $b > R + a$ in free space (see Fig. 5.1). Both particles are centered on the z -axis and are symmetric with respect to it. In their respective body-fixed frames the surfaces are

described by

$$\begin{aligned}x'_{s,\text{sphere}} &= R \sin(\Theta_s) \cos(\varphi_s) \\y'_{s,\text{sphere}} &= R \sin(\Theta_s) \sin(\varphi_s) \\z'_{s,\text{sphere}} &= R \cos(\Theta_s)\end{aligned}\tag{5.1}$$

and

$$\begin{aligned}x'_{s,\text{torus}} &= (b + a \cos(\Theta_t)) \cos(\varphi_t) \\y'_{s,\text{torus}} &= (b + a \cos(\Theta_t)) \sin(\varphi_t) \\z'_{s,\text{torus}} &= a \sin(\Theta_t),\end{aligned}\tag{5.2}$$

with Θ_t and $\varphi_{s/t} \in [0, 2\pi]$, and $\Theta_s \in [0, \pi]$. From here onward all properties will be given in the frame (x, y, z) co-moving with the torus unless specified otherwise. In this frame the torus is centered at the origin and the sphere can move along the z -axis.

Both the catalytic region $j_{s/t}$ on the torus and sphere are axisymmetric and fully defined by the coverage parameter $\chi_{s/t} \in [-1, 1]$ (see Fig. 5.2)

$$j_s(\mathbf{r}') = \tilde{\Theta}(\chi_s - z'_{s,\text{sphere}})\tag{5.3}$$

$$j_t(\mathbf{r}') = \tilde{\Theta}(\chi_t - z'_{s,\text{torus}}),\tag{5.4}$$

with $\tilde{\Theta}$ being the Heaviside step function and $\chi_{s/t} = -1$ corresponds to zero coverage and $\chi_{s/t} = 1$ to full coverage.

Finally, the torus centerline radius b will be used as the characteristic lengths scale l_0 of the system and all geometric properties will be specified in terms of it.

5.3 Self-phoretic torus-sphere pair

The velocities for the two particles in different configurations are calculated analogously to the earlier chapter 4. First the concentration field in the liquid surrounding the particles needs to be known. Assuming very small Péclet number $Pe \ll 1$ the concentration field c can be calculated using Laplace's equation

$$\nabla^2 c = 0\tag{5.5}$$

with the boundary conditions

$$-D[\mathbf{n}_s \cdot \nabla c] = \kappa j(\mathbf{r}_s); \mathbf{r} \in \mathbf{r}_{s,\text{sphere}}\tag{5.6}$$

$$D[\mathbf{n}_t \cdot \nabla c] = \kappa j(\mathbf{r}_t); \mathbf{r} \in \mathbf{r}_{s,\text{torus}}\tag{5.7}$$

and

$$c(|\mathbf{r}| \rightarrow \infty) = 0.\tag{5.8}$$

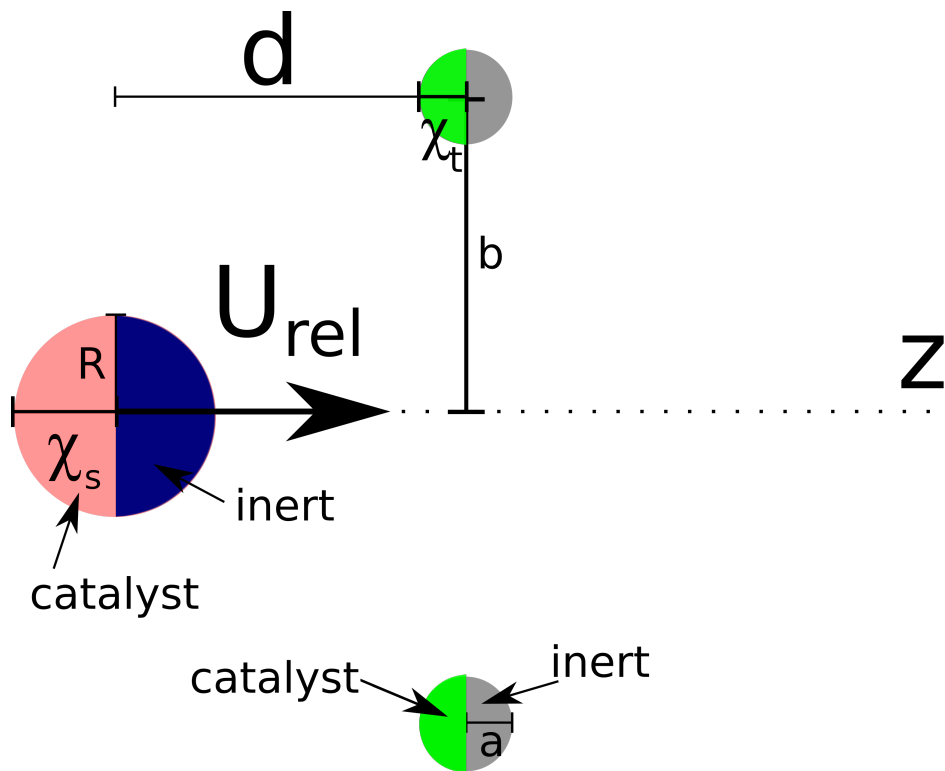


Figure 5.2: Schematic depiction of the torus-sphere system. In this example both particles are half covered ($\chi_{s,t} = 0$) and separated by a distance d . The sphere has radius R , and the torus has tube radius a and tube centerline radius b . The frame is co-moving with the torus.

\mathbf{n}_s and \mathbf{n}_t are the surface normal vectors for the sphere and torus respectively. The surface boundary conditions have opposing signs, because the toroidal normal vector points inwards by convention, while the spherical points outward (see figure 5.5). D is the diffusion constant of the product molecules and the characteristic rates of solute production per unit surface area κ is chosen to be identical on both the sphere and torus. Once the concentration field is known on the surface of particles, it can be used to calculate the so-called slip velocities

$$\mathbf{v}_{slip,s}(\mathbf{r}_s) = -b_s(\mathbf{r}_s)\nabla_s c \quad (5.9)$$

$$\mathbf{v}_{slip,t}(\mathbf{r}_t) = -b_s(\mathbf{r}_t)\nabla_s c \quad (5.10)$$

for a given surface mobility b_s . The surface mobility on the sphere and the torus is set to be uniform, identical and negative. In free space the particles will move with their inert "faces" forward and catalytic caps backward. The slip velocities $\mathbf{v}_{slip,s/t}$ are then used to construct and solve the hydrodynamic problem. The particles are surrounded by a incompressible, Newtonian fluid governed the Stokes equation

$$-\nabla P + \mu \nabla^2 \mathbf{u} = 0. \quad (5.11)$$

In the laboratory frame the fluid far away from the particles is at rest

$$\mathbf{u}(|\mathbf{r}| \rightarrow \infty) = 0 \quad (5.12)$$

and has to fulfill the surface boundary conditions

$$\mathbf{u}(\mathbf{r}_{s,sphere}) = \mathbf{U}_s + \boldsymbol{\Omega}_s \times (\mathbf{r}_{s,sphere} - \mathbf{r}_{c,sphere}) + \mathbf{v}_{slip,s}(\mathbf{r}_{s,sphere}) \quad (5.13)$$

and

$$\mathbf{u}(\mathbf{r}_{s,torus}) = \mathbf{U}_t + \boldsymbol{\Omega}_t \times (\mathbf{r}_{s,torus} - \mathbf{r}_{c,torus}) + \mathbf{v}_{slip,t}(\mathbf{r}_{s,torus}). \quad (5.14)$$

$\boldsymbol{\Omega}_{s/t}$ and $\mathbf{U}_{s/t}$ are the rotational and translational velocities of the sphere and torus respectively. They are not yet known but can be determined using Lorentz reciprocal theorem 2.6 and the force and torque free conditions. For a more concise description all further parameters will be given as dimensionless quantities. This is achieved by using the earlier equations to define a characteristic velocity $U_0 = b_s \kappa / D$ and concentration $c_0 \equiv \kappa l_0 / D$

5.3.1 Pair interaction

Following the above outlined steps the relative velocity $\mathbf{U}_{rel} = \mathbf{U}_s - \mathbf{U}_t$ between the torus and the sphere can be calculated. The relative velocities presented in Fig. 5.3 (a) are for a half-covered sphere of radius $R = 0.3$ and half-covered torus with tube radius $a = 0.5$. These results are numerically calculated with the boundary element method (BEM, see 2.7).

Qualitatively, there are four types of configuration the system can possibly take. Either the sphere or the torus is moving faster and either the sphere or the torus is leading. Fig. 5.3 (b)

shows schematic illustrations for all four possibilities instead of data points as a guide to the reader. Of these four configurations the shown system is shown to be in all of them. Starting with the sphere far in front of the torus, the two particles have no significant interaction and simply move with their respective free space velocities. Under these circumstances the torus is faster (bottom right quadrant) and thus catches up to the sphere. As they get closer to each other the torus slows down a small amount (see Fig. 5.3 (c)). The sphere on the other hand speeds up significantly. Both these changes combine to increase the relative swimming velocity U_{rel} . At a distance of $d_0 = 3.95$ the velocities of both particles are equal and the system reaches a fixed point. In this configuration the two particles still move together, but without any more changes in their relative position or velocity. The pair swimming speed is slightly lower than the torus' free space velocity. This fixed point can be reached from either side, as in the region from $d = 3.95$ to $-d = 0.09$ the relative velocity is positive, meaning the sphere moves faster than the torus.

However, for distances $-0.5 \lesssim d \lesssim 0.5$ the trend for the relative velocity reverses. As d decreases the sphere slows down and the torus speeds up. At a distance of $d_0 = -0.09$ the velocities of both particles are again equal. However, if the sphere is further behind the torus it never catches up to the torus and it escapes instead. The second point of vanishing relative velocity U_{rel} is thus an unstable fixed point. Numeric calculations with the sphere moved and rotated out of the axis of symmetry show, the first fixed point is stable against distortion in all three dimensions, only if the surface mobility is negative. As an illustrative example, moving the sphere at the fixed point of the axis of symmetry, necessarily places it closer to the torus. In this position the half of the sphere closest to the torus experiences a higher concentration field, and combined with the negative surface mobility this pushes the sphere back towards the center.

The interaction between the torus and the sphere consists of two parts, a hydrodynamic one and one facilitated by the chemical field. In order to separate those two all the calculations are redone without updating the slip velocity $v_{\text{slip},s/t}$ at each separation distance d and instead using the free space slip velocities for each respective particle. This calculation gives the contribution to the particles' motion from hydrodynamic interactions. The difference between the "complete" and "reduced" velocities can be regarded as the chemical contribution to the velocity. The resulting velocities are presented in Fig. 5.4. From these results it becomes apparent that both the hydrodynamic interaction, as well as, the chemical field interaction are significant. However, the latter one is dominant and in the next section an analytic solution for the Laplace equation of this system is presented and discussed to gain a deeper understanding of the interaction.

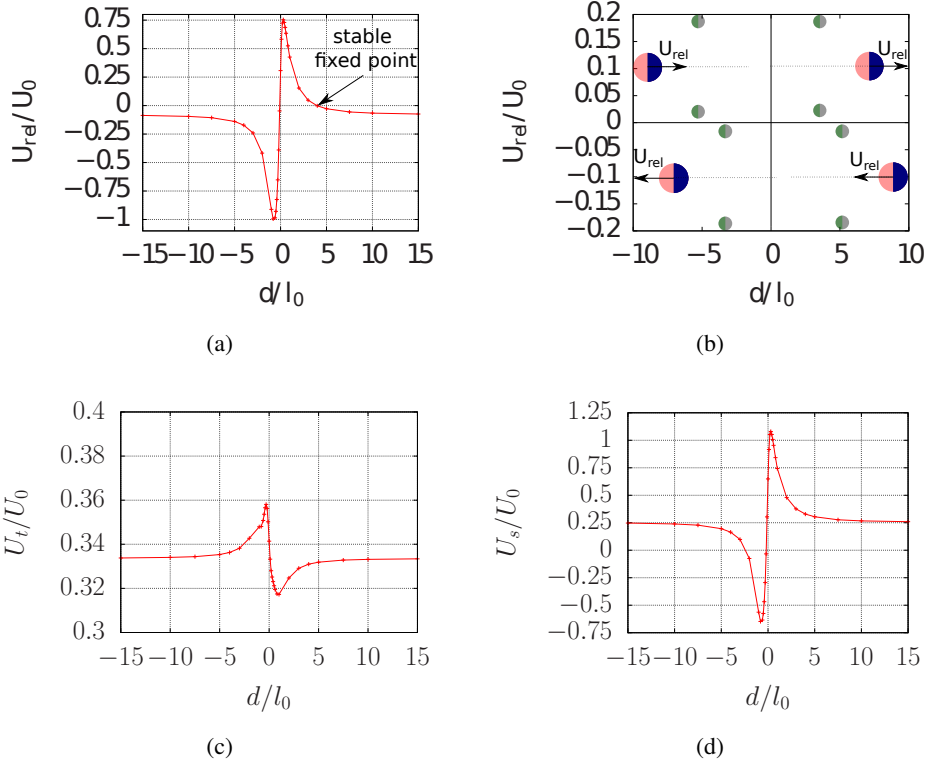


Figure 5.3: (a) Variation of the relative velocity U_{rel} between a half covered self-diffusiophoretic sphere $R = 0.3$ and torus $a = 0.5$ with the separation distance d . (b) Schematic illustration of the four possible configurations the system can be in. (c) Torus velocity U_t as a function of d . (d) Sphere velocity as it changes with d . All results were obtained with the boundary element method and the lines are only a guide to the eye.

5.4 Concentration field

5.4.1 Toroidal coordinates

In order to develop an analytical prediction for the concentration field, it will be convenient to use both spherical coordinates (r, Θ, φ) and toroidal coordinates (ξ, η, φ) (see Fig. 5.5). Due to the axisymmetry in our system the azimuthal angle φ can be neglected, reducing the complexity of the system to two dimensions. The toroidal coordinates transform into the Cartesian coordinates via the following transformations

$$x = d_s \frac{\sinh(\xi)}{\cosh(\xi) - \cos(\eta)} \quad (5.15)$$

$$z = d_s \frac{\sin(\eta)}{\cosh(\xi) - \cos(\eta)}. \quad (5.16)$$

$0 \leq \xi \leq \infty$, $0 \leq \eta \leq 2\pi$ and d_s is a geometric constant depending on a and b . In these coordinates the surface of the torus is defined by a constant $\xi = \xi_0$ value. Finally, the Lamé

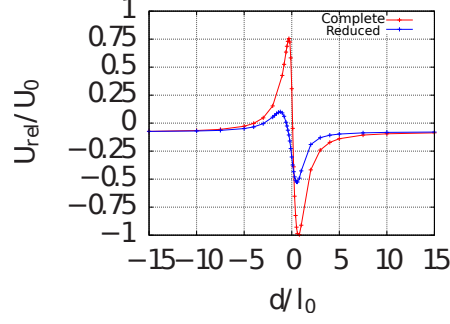


Figure 5.4: Comparison of the relative velocity U_{rel} between the full model and a purely hydrodynamic model (see 5.3.1). Both particles are half covered and have $R = 0.3$ and $a = 0.5$ respectively. All results were obtained with the boundary element method and the lines are only a guide to the eye.

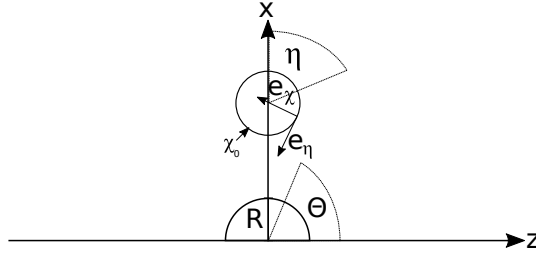


Figure 5.5: Illustration of Cartesian (x, z) , spherical (r, Θ) and toroidal (ξ, η) coordinate system. The sphere and torus surface, as well as the toroidal basis vectors, are also depicted.

parameters will be needed

$$h_{\xi} = h_{\eta} = \frac{d_s}{\cosh(\xi) - \cos(\eta)}. \quad (5.17)$$

As shown in Fig. 5.5 it is important to note that the surface normal vector into the fluid $\mathbf{n}_{\text{torus}}$ points in the opposite as the ξ base vector $\mathbf{e}_{\xi} = -\mathbf{n}_{\text{torus}}$.

5.4.2 Method of reflection

Using the method of reflections the concentration field surrounding the particles can be predicted. This method is well known and often used for electrostatic problems and will be adapted to the present system. In the method of reflections the two particles are viewed as individual particles in free space with additional surface disturbances induced by the other particle in addition to the catalyst. This enables the use of the known free space solutions $c_{\text{sphere}}^{(i)}$ and $c_{\text{torus}}^{(i)}$. Using the linearity of Laplace's equation the overall solution can then be constructed by simply adding the individual terms up

$$c(\mathbf{r}) = \sum_i \left(c_{\text{sphere}}^{(i)}(\mathbf{r}) + c_{\text{torus}}^{(i)}(\mathbf{r}) \right). \quad (5.18)$$

The additional disturbances are dependent on the second particle and have to be calculated iteratively. The $^{(i)}$ indicates which order of reflection the solution term represents. In the following the example of case of an inert sphere and a catalytic torus will be discussed to illustrate this process. The inverted case of an catalytic sphere and an inert torus can be calculated analogously. All other cases can be constructed as a combination of those two. Starting with the catalytic torus in free space the concentration field on its surface, as well as in the surrounding fluid, needs to be calculated. The axisymmetric solution to Laplace's equation in toroidal coordinates (ξ, η, ϕ) (see Fig. 5.5) [162, 163, 216] is known

$$c_{\text{torus}}^{(i)}(\xi, \eta) = \sqrt{\cosh(\xi) - \cos(\eta)} \sum_n (C_n^{(i)} \cos(n\eta) + D_n^{(i)} \sin(n\eta)) P_{n-1/2}(\cosh(\xi)). \quad (5.19)$$

$C_n^{(i)}$ and $D_n^{(i)}$ are coefficients and $P_{n-1/2}$ is the Legendre polynomial of half-integer order $n - 1/2$.

By imposing the initial surface boundary condition

$$\frac{1}{h_\xi} \frac{d}{d\xi} c_{\text{torus}}^{(0)}(\mathbf{r}) = j_t(\mathbf{r}); \mathbf{r} \in r_{s,\text{torus}} \quad (5.20)$$

$C_n^{(0)}$ and $D_n^{(0)}$ are fixed and Eq. (5.19) can be used to calculate the concentration field in the fluid. This concentration field extends all the way to the sphere and can be regarded as an external disturbance on the surface of the inert sphere

$$\frac{d}{dr} c_{\text{torus}}^{(0)}(\mathbf{r}) \neq 0; \mathbf{r} \in r_{s,\text{sphere}}. \quad (5.21)$$

This disturbance violates the sphere's boundary condition and needs to be balanced. An additional term $c_{\text{sphere}}^{(1)}$ is thus needed for the overall solution. Within the method of reflection the sphere is again considered to be in free space with the general axisymmetric solution

$$c_{\text{sphere}}^{(1)} = \sum_n E_n^{(1)} r^{-n-1} P_n(\cos(\vartheta)). \quad (5.22)$$

The boundary condition for this subsystem is

$$\frac{d}{dr} c_{\text{sphere}}^{(1)}(\mathbf{r}) = -\frac{d}{dr} c_{\text{torus}}^{(0)}(\mathbf{r}); \mathbf{r} \in r_{s,\text{sphere}}. \quad (5.23)$$

such that the overall boundary condition on the sphere is restored

$$\frac{d}{dr} c_{\text{torus}}^{(0)}(\mathbf{r}) + \frac{d}{dr} c_{\text{sphere}}^{(1)}(\mathbf{r}) = 0; \mathbf{r} \in r_{s,\text{sphere}}. \quad (5.24)$$

However, this added term now disturbs the boundary condition on the torus surface

$$\frac{1}{h_\xi} \frac{d}{d\xi} c_{\text{sphere}}^{(1)}(\mathbf{r}) \neq 0; \mathbf{r} \in r_{s,\text{torus}}, \quad (5.25)$$

leading to a back and forth with diminishing disturbances until the new terms are sufficiently small to be neglected. A similar iterative process needs be done starting with the boundary condition on the torus. As the last step the individual contributions need to be added up to gain the overall solution.

5.4.3 Solution in toroidal coordinates

For axisymmetric system, the Laplace equation in toroidal coordinates

$$0 = \frac{\partial}{\partial \xi} \left(\frac{\sinh \xi}{\cosh \xi - \cos \eta} \frac{\partial c}{\partial \xi} \right) + \frac{\partial}{\partial \eta} \left(\frac{\sinh \xi}{\cosh \xi - \cos \eta} \frac{\partial c}{\partial \eta} \right) \quad (5.26)$$

is solved by

$$c_{\text{torus}}^{(i)}(\xi, \eta) = \sqrt{\cosh(\xi) - \cos(\eta)} \sum_n (C_n^{(i)} \cos(n\eta) + D_n^{(i)} \sin(n\eta)) P_{n-1/2}(\cosh(\xi)), \quad (5.27)$$

if the concentration field decays to 0 at infinity. The remaining boundary condition states

$$\mathbf{e}_\xi \cdot \nabla c_{\text{torus}}^{(i)}(\xi, \eta)|_{\xi=\xi_0} = \frac{1}{h_\xi} \frac{\partial c_{\text{torus}}^{(i)}(\xi, \eta)}{\partial \xi} \Big|_{\xi=\xi_0} = (\delta_{0,i} \cdot j_t(\eta) + \frac{\partial c_{\text{sphere}}^{(i-1)}(\xi, \eta)}{\partial \xi}) \Big|_{\xi=\xi_0}. \quad (5.28)$$

Following Schmiedling et al [216] the coefficients $C_n^{(i)}$ and $D_n^{(i)}$ can be determined by first calculating the Fourier coefficients \mathfrak{C}_n and \mathfrak{D}_n

$$\frac{(j_t(\eta) + \frac{\partial c_{\text{sphere}}^{(0)}(\xi, \eta)}{\partial \xi})}{\sinh \xi_0 \sqrt{\cosh \xi_0 - \cos \eta}} d = \sum_n (\mathfrak{C}_n \cos n\eta + \mathfrak{D}_n \sin n\eta) \quad (5.29)$$

and then relating them to the coefficients

$$\begin{aligned} & \sum_n (C_n \cos n\eta + D_n \sin n\eta) \left(\frac{1}{2} P_{n-1/2}(\cosh \xi_0) + (\cosh \xi_0 - \cos \eta) P'_{n-1/2}(\cosh \xi_0) \right) \\ &= \sum_n (\mathfrak{C}_n \cos n\eta + \mathfrak{D}_n \sin n\eta). \end{aligned} \quad (5.30)$$

\sum_n are the well known sums, but with the zeroth order multiplied by 1/2.

5.4.4 Spherical solution

On the other hand the axisymmetric Laplace equation in spherical (r, Θ, φ) coordinates reads as

$$0 = \frac{1}{r^2} \frac{\partial}{\partial r} \left(r^2 \frac{\partial}{\partial r} \right) + \frac{1}{r^2 \sin(\Theta)} \frac{\partial}{\partial \Theta} \left(\sin(\Theta) \frac{\partial}{\partial \Theta} \right) \quad (5.31)$$

and for concentration fields vanishing at infinity

$$c_{\text{sphere}}^{(i)}(r, \Theta) \quad (5.32)$$

has the solution

$$c_{\text{sphere}}^{(i)}(r, \Theta) = \sum_n E_n^{(i)} r^{-n-1} P_n(\cos(\Theta)) \quad (5.33)$$

with the surface boundary condition in the normal direction

$$-\mathbf{e}_r \cdot \nabla c_{\text{sphere}}^{(1)}(r, \Theta)|_{r=R} = j_s(\Theta) + \frac{\partial c_{\text{torus}}^{(i-1)}(\xi, \eta)}{\partial r}|_{r=R}. \quad (5.34)$$

E_n can be calculated by multiplying Eq. (5.34) with the corresponding Legendre polynomials and integrating both sides with respect to Θ .

5.4.5 Coordinate Transformations

In order to use the disturbance created by the torus calculated in toroidal coordinates as a boundary condition for the sphere and vice versa, coordinate transformations are necessary. The four coordinate transformations are

$$\Theta = \arctan \left(\frac{\sin \eta (\cosh \xi - \cos \eta)}{\sinh \xi (\cosh \xi - \cos \eta)} \right) \quad (5.35)$$

$$r = d \sqrt{\left(\frac{\sinh \xi}{\cosh \xi - \cos \eta} \right)^2 + \left(\frac{\sin \eta}{\cosh \xi - \cos \eta} \right)^2} \quad (5.36)$$

from toroidal to spherical coordinates and from spherical to toroidal coordinates

$$d_1 = \sqrt{(r \cos(\Theta) + ds)^2 + (r \sin(\Theta))^2} \quad (5.37)$$

$$d_2 = \sqrt{(r \cos(\Theta) - ds)^2 + (r \sin(\Theta))^2} \quad (5.38)$$

$$\xi = \ln(d_1/d_2) \quad (5.39)$$

$$\eta = \arccos \left(\frac{d_1^2 + d_2^2}{2d_1 d_2} \right). \quad (5.40)$$

5.4.6 Results

In Figs. 5.6 and 5.7 the concentration field on the surface of the torus ($a = 0.5$) and sphere ($R = 0.3$) for a range of separation distances d are shown. The solid line represents the analytic prediction and the points numeric calculations with BEM. In both cases the qualitative, as well as the quantitative agreement are remarkable. The method of reflection captures all the noticeable features. Discussing the concentration field profiles on the torus first, it is immediately noticeable that there are almost no qualitative changes with the separation

distance. Both when the two particles are fairly far apart (Fig. 5.6 (a)), as well as when there is no vertical separation between the particles (Fig. 5.6 (b)), the maximum of the concentration is at $\eta_{\max} = 1.162\pi$ and the minimum at $\eta_{\min} = 0.409\pi$. $\eta = \pi$ represents the points on the torus surface facing towards the center and $\eta = 3/2\pi$ is the center of the catalytic patch (see Fig. 5.5). Notably the maximum concentration is not at the center of the patch but instead gets shifted significantly towards the center of the torus due to the influence of torus parts beyond the positive $x - z$ plane. The produced molecules accumulate in the hole, with all 360° of the torus surrounding it contributing to the increase. Whether or not the sphere is close to the center of the torus or not has no noticeable effect on this behavior. The concentration minimum is also shifted away from the center of the inert region $\eta = \pi/2$ of the torus surface, however not as significantly. These results agree very well with the earlier observation that the swimming velocity of the torus remains fairly constant.

The concentration profiles on the surface of the sphere, on the other hand, varies significantly with a changing separation distance d (see Fig 5.7). Starting with the particles well separated ($d = \pm 5$, Fig. 5.7 (a)-(b)) there is no qualitative difference between the two positions and the minimum ($\Theta = 0$) and the maximum ($\Theta = \pi$) of the concentration field are at their expected locations, i.e. the center of the catalytic and inert regions. The tangential gradient is negative throughout and has its highest magnitude at the interface between the inert and catalytic regions ($\Theta = \pi/2$). Qualitatively a difference is noticeable, the minimum value is higher for $d = -5$ since here the inert face of the sphere is closer to the active areas of the torus. The differences depending on whether the sphere or torus are in front become much more pronounced for decreasing d .

Keeping the torus in front and decreasing the separation distance d the concentration profiles change dramatically (see Figs 5.7 (c), (e) and (g)). While the concentration increases for all angles Θ , it rises much faster in the region facing the torus. This pushes both the concentration minimum and maximum more and more towards the interface between the inert and active region (see Fig. 5.7 (c) with $d = -2$). At even closer ranges (see Fig. 5.7 (e) with $d = -0.5$) two minima can be seen at the center of both the inert region ($\Theta = 0$) and the active region ($\Theta = \pi$). The sphere's own activity is irrelevant in this position and becomes fully dominated by the concentration field produced by the torus. The concentration maximum is at the interface of the two regions. These changes also have an enormous influence on the tangential gradient, which determines the slip velocity. Not only does the magnitude of the gradient change, but also its sign. This explains why the propulsion of the sphere close to the torus not only slows down but also changes direction.

Investigating a concentration profile in the area of rapid acceleration of the sphere ($-0.5 \lesssim d \lesssim 0.1$), shows a reversal back to original profile. The gradients of highest magnitude are again at the interface between the inert and catalytic region, although the gradients are still significantly larger.

When the sphere is in front of the torus, changing the distance between the two (see Figs. 5.7 (d), (f) and (h)) does not change the general appearance of the concentration profile. However, the overall magnitude and gradient between the maximum and minimum increase

as d decreases. This again explains why the sphere is faster if it is behind torus.

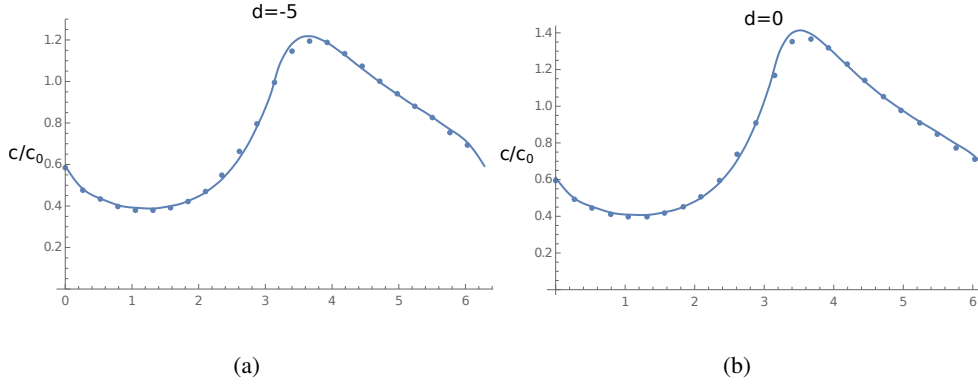


Figure 5.6: Concentration profiles on the surface of a half covered torus ($a = 0.5$) as a function of the angle η . The torus is at a distance of $d = -5$ (a) and $d = 0$ (b) from a half covered sphere ($R = 0.3$). The line indicates the analytic prediction (see 5.4.2) and the points are calculated with the boundary element method

5.4.7 Designing a lock

Finally, in the introduction the question was raised if this system is able to function as barrier for specific types of particles, i.e. in a lock and key type mechanism only certain self-diffusiophoretic swimmers can pass through the torus. For the barrier to be as stationary as possible a fully catalytic torus ($\chi_t = 1$) is chosen. In Figs. 5.8 (a) and (b) two spheres ($R = 0.1$) are separately tested against such a torus ($a = 0.1$). The first sphere is half covered, while the second sphere has a smaller active area ($\chi_s = -0.2$). This reduces the second sphere's free space velocity.

Starting with the spheres located behind the torus, both move towards it. Close to the torus both experience the same pattern of acceleration and deceleration described earlier 5.3.1. However, for the chosen parameters (coverage $\chi_s = 0$ and geometry $R = 0.1$, $a = 0.1$) the first sphere does not slow down enough to form a pair with the torus. Instead, its velocity is always larger than zero and it passes through the torus. In contrast the second, slower sphere gets captured and does not overcome the barrier.

These results show the system can function as a *lock* barrier, letting only specific, i.e. fast enough, self-diffusiophoretic particles (*keys*) through.

5.5 Conclusion

In this work the interaction between a self-diffusiophoretic sphere and a self-diffusiophoretic torus has been studied. In this system a range of interesting dynamics can be observed. Both the sphere and the torus accelerate and decelerate depending on their relative position, their geometric parameters and their catalytic activity. The sphere can even be shown to reverse its direction of motion. Particularly interesting is the existence of stable separation distances, at

which the relative velocity between the particles vanishes and they continue to swim as a pair. Such a pair could function as the building block for a chain of many more active particles moving together in a single direction.

Using the method of reflections an analytic prediction for the concentrations field was used to better understand the complex nature of the observed dynamics. It can also be a useful tool for designing particles and answering some of the still open questions in the future. How stable is the swimming direction for the pair against perturbations? Can the stable separation distance be changed, and how does it change depending on the varies design parameters? And finally, what happens if a third or even more particles are added to the system? Is finding a system with bistability (stable positions for a sphere on both sides of the torus) necessary to achieving self-organizing chains?

For fully covered tori an interesting observation has been made. Due to their inherent symmetry they do not move on their own in free space, but nonetheless, are able to slow down a self-diffusiophoretic sphere. However, due to the much greater velocity difference far apart, the earlier mentioned fixed point does not exist for all spheres. This opens the possibility to design a speed gate. Only self-diffusiophoretic particles above a certain threshold velocity can pass through this filter. This allows for the organized separation of a collection of self-diffusiophoretic particles into distinct groups. Further studies, will be necessary to investigate if these dynamics hold true when replacing the torus with a hole in a wall covered by a catalytic patch and if they can be reproduced experimentally.

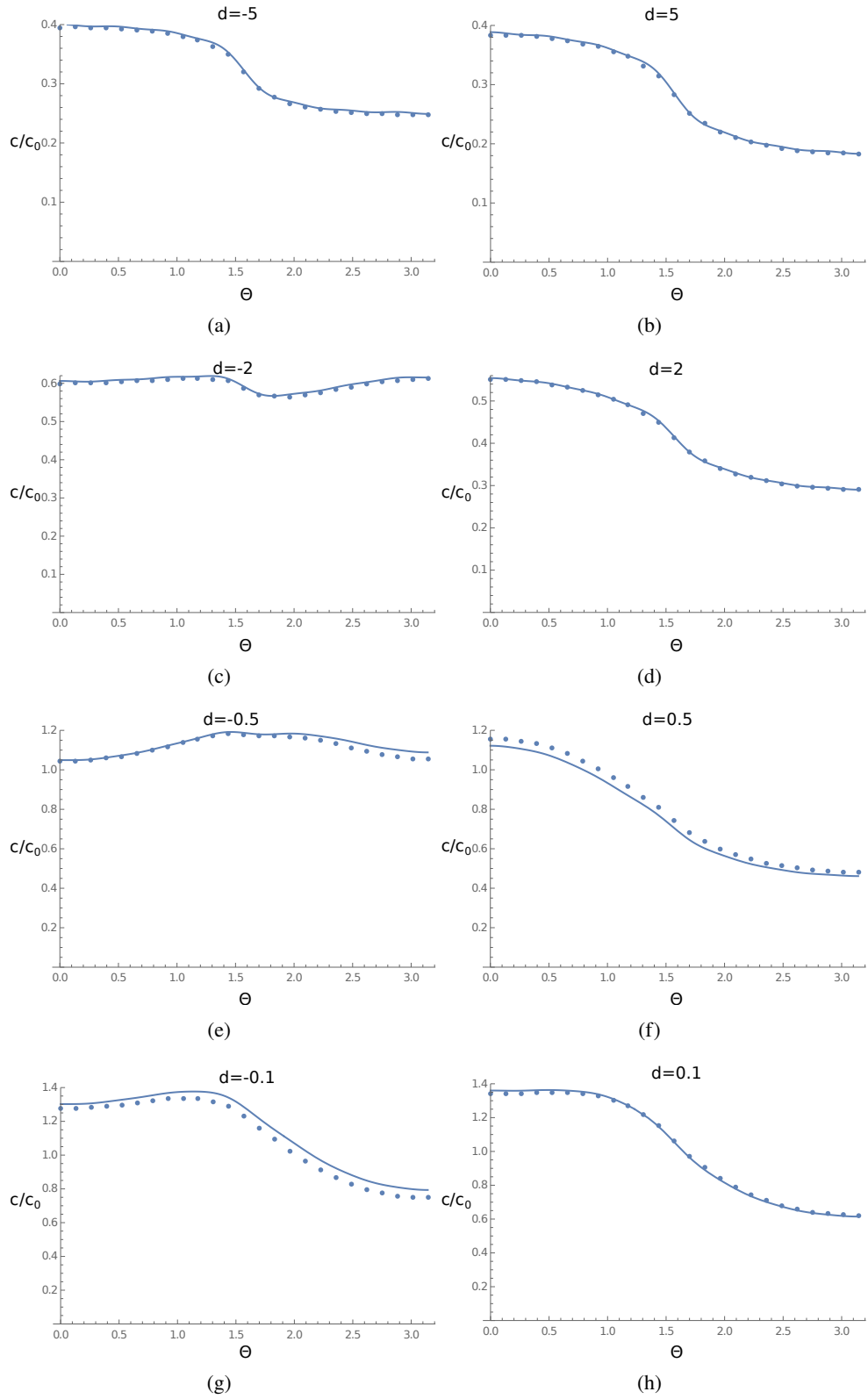


Figure 5.7: Concentration profiles on the surface of a half covered sphere ($R = 0.3$) as it changes with the angle Θ . The sphere is at a distance of $d = -5$ (a), $d = 5$ (b), $d = -2$ (c), $d = 2$ (d), $d = -0.5$ (e), $d = 0.5$ (f), $d = -0.1$ (g) and $d = 0.1$ (h) from a half covered torus ($R = 0.5$). The line indicates the analytic prediction (see 5.4.2) and the points are calculated with the boundary element method.

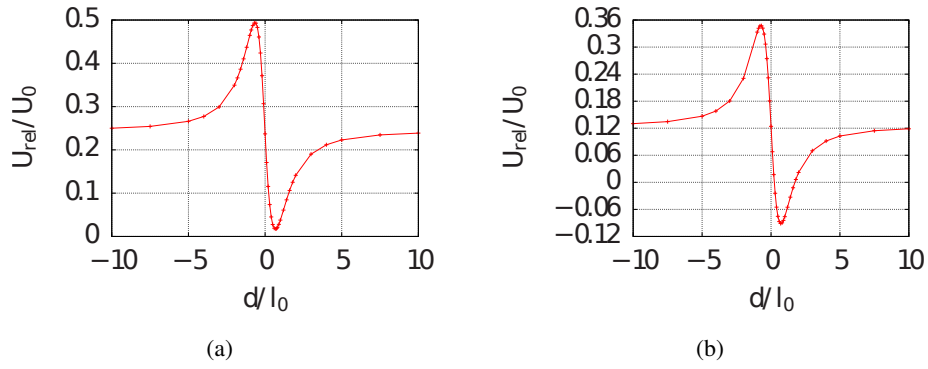


Figure 5.8: The relative velocity U_{rel} between a self-diffusiophoretic spheres ($R = 0.1$) and a torus ($a = 0.1$) fully covered by a catalyst as a function of their separation distance d . In (a) the sphere is half covered ($\chi_s = 0$) and in (b) it is less then half covered ($\chi = -0.2$). All results were obtained with the boundary element method and the lines are only a guide to the eye.

CHAPTER 6

AXISYMMETRIC SPHEROIDAL SQUIRMERS AND SELF-DIFFUSIOPHORETIC PARTICLES

Up to this point this work has focused on one specific type of microswimmer, self-diffusiophoretic colloids. For the final two projects presented, a more general approach will be discussed, the squirmer model. The squirmer model does not include a detailed description of the propulsion mechanism of the microswimmer, and instead uses the slip velocity as its starting point. It immediately follows that squirmer particles only interact hydrodynamically with their surroundings. This simplification allows the model to be applied to a much wider range of microswimmers. In many instances, it can be used for self-diffusiophoretic and other artificial microswimmers [194], but its original purpose is to analyze biological microswimmers such as ciliated microorganisms [145]. Understanding their behavior, limitations, and tendencies will open new opportunities for improvements in the food and nutrient industry. Many everyday food products, such as cheese or bread, rely on microorganisms. Providing optimal conditions for the microorganisms, e.g. bread yeast, to thrive and work at maximum efficiency, can reduce the price of food. Furthermore, by tailoring the conditions to a specific species, contamination can be prevented and food quality improved.

The insight to hinder unwanted microorganisms can also be applied directly in medicine. Whether it is to develop new, more effective methods to sterilize equipment or improve the effectiveness of known therapeutic methods, understanding how microorganisms, e.g. *E. coli*., survive against outside stresses can be used to overcome these strategies.

An aspect of microorganisms not fully understood is their shape. Almost none have a spherical body, but spheroidal ones are much more common. It is well known that even this relatively minor change in the geometry of a particle can have a significant effect on its interactions with the surroundings. Spheroids can, to name only a few effects, align in response to an ambient flow [238], order themselves [141] and change their diffusiophoretic behavior [53] with respect to corresponding spherical particles.

The results of the following chapter have been published under an open access model in the peer-reviewed journal *Journal of Physics: Condensed Matter* [186].

6.1 Abstract

We study, by means of an exact analytical solution, the motion of a spheroidal, axisymmetric squirmer in an unbounded fluid, as well as the low Reynolds number hydrodynamic flow associated to it. In contrast to the case of a spherical squirmer — for which, e.g., the velocity of the squirmer and the magnitude of the stresslet associated with the flow induced by the squirmer are respectively determined by the amplitudes of the first two slip (“squirming”) modes — for the spheroidal squirmer each squirming mode either contributes to the velocity, or contributes to the stresslet. The results are straightforwardly extended to the self-phoresis

of axisymmetric, spheroidal, chemically active particles in the case when the phoretic slip approximation holds.

6.2 Introduction

Self-propulsion of micro-organisms, such as bacteria, algae and protozoa, plays an important role in many aspects of nature. Whether a bacteria tries to reach a nutrient rich area or a sperm cell an unfertilized egg, motility often yields a substantial advantage over competitors. Due to their small size and velocity, the viscous friction experienced by the micro-organisms swimming in water is very strong compared to inertial forces [86, 180]; consequently, they have developed swimming mechanisms adapted to these circumstances.

The motion of motile bacteria and other small organisms is typically induced by the beating of thin, thread-like appendages, the so called flagella; however, these species exhibit a broad morphology, in that they may possess either a single flagellum (e.g., monotrichous bacteria), several flagella (e.g., *E. coli.*), or a carpet of many small flagella, called cilia (e.g. *Opalina*). Focusing for the moment on the example of cilia covered micro-organisms, it was proposed by Lighthill that the emergence of motility can be understood without a detailed modeling of the complex, synchronous beating of the cilia [145]. Instead, the effect of this beating pattern, i.e., the time-averaged surface flow induced by the envelope of cilia tips, has been modeled as providing a prescribed *active* flow velocity \mathbf{v} (actuation) at the surface of the particle (both within the tangent plane of the surface, \mathbf{v}_s , and in the direction normal to the surface, \mathbf{v}_n). The model, known by now as the “squirmer” model, was subsequently corrected and extended by his student Blake [25].

In its simplest and most used form, the tangential slip velocity of a spherical squirmer is taken to be the superposition of the fore-aft asymmetric and fore-aft symmetric modes with the slowest decaying contributions to flow in the surrounding liquid, i.e., the leading order modes. Combined, they make for a squirmer endowed with motility (from the leading fore-aft asymmetric mode) and with a hydrodynamic stresslet (from the leading fore-aft symmetric mode) [83, 240, 246, 264, 265].

Considerable progress has already been made in understanding the behavior of spherical squirmers, and many interesting questions have been answered, such as: what does the flow field around a squirmer look like and how it compares with the ones produced by simple microorganisms [25, 56, 57]; what happens if the swimmer is not in free space, but rather disturbed by boundaries [265] or external flows [240]; and how do pairs or even swarms of these particles interact [83]. Although this model can also be used to better understand the motion of micro-organisms, e.g. *Volvox* [178], observed in experiments, its restriction to spherical swimmers limits a wider application. For example, *Paramecia*, one of the most studied ciliates, has an elongated body [101, 224, 263], which prevents a straightforward application of the traditional squirmer model. However, the aforementioned questions are also of interest for these and other elongated micro-organisms. A generalization of the squirmer model to non-spherical shapes is thus a natural, useful development.

Driven by advances in technology that allow increasingly sophisticated manufacturing capabilities, in the last decade significant efforts have been made towards the development of artificial swimmers [81, 106, 168, 206, 243]. The envisioned lab-on-a-chip devices and micro-cargo carriers [62, 228], e.g., for targeted drug deliveries and nanomachines focused on monitoring and dissolving harmful chemicals [74, 223], all need to perform precise motions on microscopic length scales. A better understanding of the general framework of microscale locomotion is required in order to optimally design and control such devices, and theoretical models facilitate new steps along this path. As one example, chemically active colloids achieve self-propulsion by harvesting local free energy. They catalyze a chemical reaction in the surrounding fluid and propel due to the ensuing chemical gradient. Spherical “Janus” particles belong to this group, and it has been shown that the squirmer model can, in various circumstances, capture essential features of their motion [194]. However, there are many chemically active colloids with non-spherical shape, and rod-like particles are especially prevalent in experimental studies (see, e.g., [155, 176, 177, 206]).

It is well known that passive, non-spherical colloids exposed to an ambient flow exhibit significant qualitative differences — such as alignment with respect to the direction of the ambient flow [238], Jeffery orbits by ellipsoids in shear flow [109], nematic ordering arising from steric repulsion [141], or noise-induced migration away from confining surfaces [174] — in comparison to their spherical counterparts. It is thus reasonable to expect that endowing such objects with a self-propulsion mechanism will lead to rich, qualitatively novel dynamical behaviors, some of which may be advantageous for, while others may hinder, applications. Accordingly, it is important to develop an in-depth understanding of the shape-dependent behavior, and significant experimental and theoretical efforts have been made in this direction (see, e.g., Refs. [9, 22, 54, 71, 98, 147, 249, 251, 253, 254] as well as the insightful reviews provided in Refs. [5, 18, 55, 63, 64, 95, 136, 180, 212]).

Similar to the case of spherical swimmers, physical insight into the phenomenology exhibited by elongated swimmers can be gained from a corresponding squirmer model. For a model spheroidal swimmer moving by small deformations of its surface, Ref. [65] derived an analytic solution to the corresponding Stokes flow, from which the velocity of the swimmer could be calculated. In Ref. [140] it has been pointed out that an exact squirmer model for a spheroidal particle with a prescribed axi-symmetric, tangential slip velocity (active actuation of the fluid) on its surface can be written down by employing an available analytical solution for the axi-symmetric Stokes flow around a spheroidal object [50]. However, the approach has been used in the context of a somewhat restricted model particle, involving an additional fore-aft asymmetry of the surface slip velocity, because of the particular interest, for that work, in the question of “hydrodynamically stealthy” microswimmers. While capturing the self-propulsion velocity of the swimmer, this removes certain characteristics of the flow, *inter alia* those that contribute to the corresponding stresslet [134] and would allow distinguishing between, e.g., “puller” and “pusher” type squirmers. Moreover, the particle stresslet is a key quantity connecting the microscopic dynamics of individual particles in a colloidal suspension with the continuum rheological properties of the suspension. For active particles like bacteria,

the activity-induced stresslet can lead to novel material properties like "superfluidity" and spontaneous flow [147].

We note that also a strongly truncated model, based on an ansatz for the slip velocity in the form of two terms which, in the corresponding limit of a sphere, reproduce the first two modes of the spherical squirmer model of Lighthill and Blake, has been discussed by Ref. [231]. This approach, however, is significantly affected by the fact that — as noticed in Ref. [65] and also discussed here (see Sec. 6.5) — for spheroidal squirmers both their velocity and their stresslet involve significant contributions from the higher order slip modes, in contrast to the case of a spherical squirmer for which only the first two modes contribute to those observables.

In this paper we employ the available analytical solution for axi-symmetric Stokes flow around a spheroidal object [50] to study the velocity and the induced hydrodynamic flow field around a spheroidal squirmer with a tangential slip velocity possessing axial symmetry, but otherwise unconstrained. The model squirmer is introduced in Sec. 6.3. The series representation of the incompressible, axi-symmetric, creeping flow field around a spheroid [50] is succinctly summarized in Sec. 6.4. In Section 6.5 we discuss the velocity and the flow field corresponding to the spheroidal squirmer, with particular emphasis on illustrating the contributions from the modes of various order. Additionally, in Sec. 6.5.1 we discuss the straightforward extension of these results to deriving the flow field around a chemically active self-phoretic spheroid (for a similar mapping in the case of spherical particles see Ref. [157]). The final Sect. 6.6 is devoted to a summary of the results and to the conclusions of the study.

6.3 Model

The model system we consider is that of a spheroidal, rigid and impermeable particle immersed in an incompressible, unbounded, quiescent Newtonian liquid through which it moves due to a prescribed "slip velocity" (active actuation) at its surface (see Fig. 6.1). The slip velocity \mathbf{v}_s , which is tangential to the surface Σ of the particle (i.e., $\mathbf{n} \cdot \mathbf{v}_s \equiv 0$ on Σ , with \mathbf{n} denoting the outer (into the fluid) normal to Σ), is assumed to preserve the axial symmetry and to be constant in time, but it is otherwise arbitrary. The surface slip \mathbf{v}_s is part of the model and thus it is a given function (or, alternatively as in, c.f., Sec. 6.5.1, it is determined as the solution of a separate problem). There are no external forces or torques acting on either the particle or the liquid.

Due to the surface actuation, a hydrodynamic flow around the particle is induced and the particle sets in motion; we assume that the linear size L of the particle, the viscosity μ and the density ϱ of the liquid, and the magnitude $|\mathbf{v}_s|$ of the slip velocity are such that the Reynolds number $\text{Re} := \varrho |\mathbf{v}_s| L / \mu$ is very small. Accordingly, after a short transient time a steady state hydrodynamic flow is induced around the particle and the particle translates steadily with velocity \mathbf{U} (with respect to a fixed system of coordinates, the "laboratory frame"). (Owing to the axial symmetry, in the absence of thermal fluctuations, which are neglected in this work,

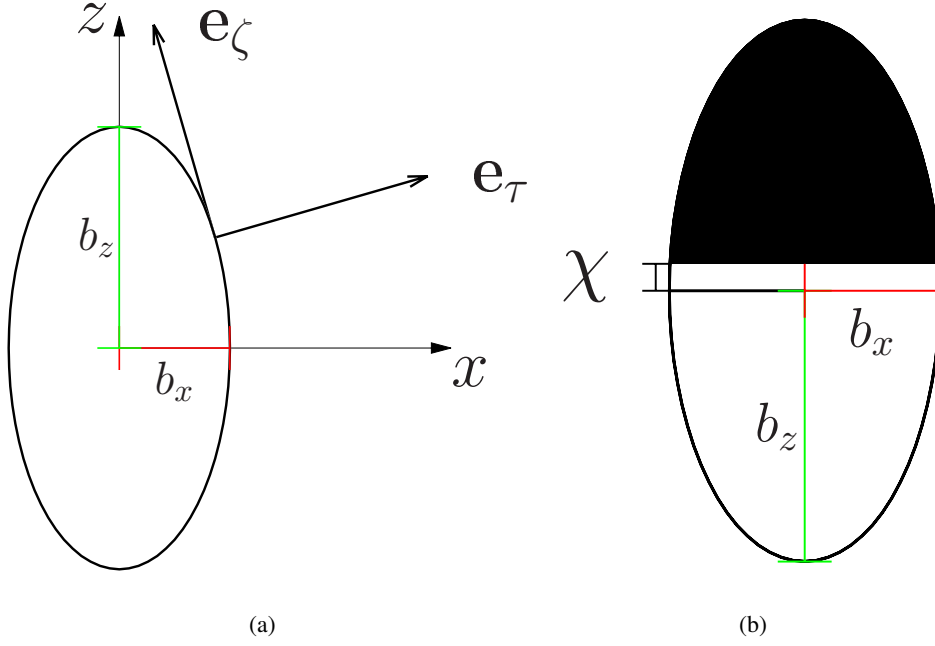


Figure 6.1: (a) Two-dimensional (2d) cut of a prolate spheroidal particle with semi-major axis b_z and semi-minor axis b_x ; also shown are the x and z axes of the co-moving system of coordinates and the unit vectors \mathbf{e}_τ and \mathbf{e}_ζ of the prolate spheroidal coordinate system; (b) 2d cut of a chemically-active self-phoretic particle; the chemically active part is the cap-like region shown in white, while the rest of the surface (black) is chemically inert. The quantity χ (“coverage”) denotes a certain measure for the extent of the active part (see Sec. 6.5.1 in the main text).

there is no rigid-body rotation of the particle in this model.)

The analysis is more conveniently carried out in a system of coordinates attached to the particle (co-moving system). This is chosen with the origin at the center of the particle and such that the z -axis is along the axis of symmetry of the particle (thus $\mathbf{U} = U\mathbf{e}_z$). The semi-axis of the particle are accordingly denoted by b_z and b_x (see Fig. 6.1); their ratio $r_e = \frac{b_x}{b_z}$ is called the aspect ratio and determines the slenderness of the particle. The values $r_e < 1$, $r_e = 1$, and $r_e > 1$ correspond to prolate, spherical, and oblate shapes, respectively.

In the co-moving system of coordinates, the flow \mathbf{v} and the velocity \mathbf{U} are determined as the solution of the Stokes equations

$$\nabla \cdot \boldsymbol{\sigma} = 0, \quad \nabla \cdot \mathbf{v} = 0, \quad (6.1)$$

where

$$\boldsymbol{\sigma} := -p \mathcal{I} + \mu [\nabla \mathbf{v} + (\nabla \mathbf{v})^T], \quad (6.2)$$

is the Newtonian stress tensor, with p denoting the pressure (enforcing incompressibility), \mathcal{I} denoting the unit tensor, and $()^T$ denoting the transpose, subject to:

– the boundary conditions (BC)

$$\mathbf{v}|_\Sigma = \mathbf{v}_s, \quad (6.3a)$$

and

$$\mathbf{v}(|\mathbf{r}| \rightarrow \infty) \rightarrow -\mathbf{U}. \quad (6.3b)$$

– the force balance condition (overdamped motion of the particle in the absence of external forces)

$$\int_{\Sigma} \boldsymbol{\sigma} \cdot \mathbf{n} d\Sigma = 0. \quad (6.4)$$

The hydrodynamic flow \mathbf{v}_{lab} in the laboratory frame, if desired, is then obtained as $\mathbf{v}_{\text{lab}}(\mathbf{P}) = \mathbf{v}(\mathbf{P}) + \mathbf{U}$, with \mathbf{P} denoting the observation point.

The boundary-value problem above can be straightforwardly solved numerically by using, e.g., the Boundary Element Method (BEM) (see, e.g., Refs. [104, 111, 221, 240]) as well as analytically. In the following, we shall focus on the analytical solution of this problem; the corresponding numerical solutions obtained by the BEM are presented in Appendix 6.7.5 and used as a means of testing the convergence of the series representation of the analytical solution. Before proceeding, we note that we will focus the discussion on the case of prolate shapes, i.e., $r_e < 1$ (see Fig. 6.1(a)); the case of an oblate squirmer ($r_e > 1$) can be obtained from the results for the prolate shapes via a certain mapping (see, e.g., Ref. [140] and Appendix 6.7.1), while the case of a sphere is obtained from the results corresponding to a prolate spheroid by taking the limit $r_e \rightarrow 1^-$.

6.4 Hydrodynamic flow and velocity of a prolate squirmer

The calculation of the hydrodynamic flow \mathbf{v} induced by the squirmer and of the velocity \mathbf{U} of the squirmer are most conveniently carried out by employing the modified prolate spheroidal coordinates ($1 \leq \tau \leq \infty, -1 \leq \xi \leq 1, 0 \leq \phi \leq 2\pi$) as in Ref. [50]. These are defined in the co-moving system of reference, which has the origin in the center of the particle, and are related to the Cartesian coordinates via [50]

$$\begin{aligned} \tau &= \frac{1}{2c} (\sqrt{x^2 + y^2 + (z+c)^2} + \sqrt{x^2 + y^2 + (z-c)^2}), \\ \xi &= \frac{1}{2c} (\sqrt{x^2 + y^2 + (z+c)^2} - \sqrt{x^2 + y^2 + (z-c)^2}), \\ \varphi &= \arctan\left(\frac{y}{x}\right), \end{aligned} \quad (6.5)$$

where $c = \sqrt{b_z^2 - b_x^2}$ is a purely geometric quantity which ensures smooth convergence into spherical coordinates in the limit $b_x \rightarrow b_z$. The unit vectors \mathbf{e}_τ and \mathbf{e}_ξ (see Fig. 6.1) are related to the ones of the Cartesian coordinates via

$$\begin{aligned} \mathbf{e}_\tau &= \left(\frac{2\tau \cdot \sqrt{1-\xi^2}}{\sqrt{\tau^2-1}} \mathbf{e}_x + \xi \mathbf{e}_z \right) \cdot \frac{\sqrt{\tau^2-1}}{\sqrt{\tau^2-\xi^2}}, \\ \mathbf{e}_\xi &= \left(\frac{2\xi \cdot \sqrt{\tau^2-1}}{\sqrt{1-\xi^2}} \mathbf{e}_x + \tau \mathbf{e}_z \right) \cdot \frac{\sqrt{1-\xi^2}}{\sqrt{\tau^2-\xi^2}}, \end{aligned} \quad (6.6)$$

and the corresponding Lamé metric coefficients are given by

$$\begin{aligned} h_\zeta &= c \frac{\sqrt{\tau^2 - \zeta^2}}{\sqrt{1 - \zeta^2}}, \\ h_\tau &= c \frac{\sqrt{\tau^2 - \zeta^2}}{\sqrt{\tau^2 - 1}}, \\ h_\varphi &= c \sqrt{\tau^2 - 1} \sqrt{1 - \zeta^2}. \end{aligned} \quad (6.7)$$

The iso-surfaces $\tau = \text{const}$ are confocal prolate spheroids with common center O; the surface of the particle corresponds to

$$\tau_0 = \frac{b_z}{c} = \frac{1}{\sqrt{1 - r_e^2}} > 1, \quad (6.8)$$

and the values $\tau > \tau_0$ ($1 \leq \tau < \tau_0$) correspond to the exterior (interior) of the prolate ellipsoid, respectively. The coordinate ζ takes the values $\zeta = \pm 1$ at the $z = \pm b_z$ apexes, respectively, and $\zeta = 0$ on the equatorial ($x - y$ plane cut) circle. Note that, as shown in Fig. 6.1(a), \mathbf{e}_τ coincides with the normal \mathbf{n} while \mathbf{e}_ζ and \mathbf{e}_ϕ span the tangent plane.

6.4.1 Velocity of the squirmer

The velocity of the squirmer can be determined from Eqs. (6.1) - (6.4) as a linear functional of the axi-symmetric slip velocity $\mathbf{v}_s = v_s(\zeta)\mathbf{e}_\zeta$ without explicitly solving for the flow \mathbf{v} . This follows via a straightforward application of the Lorentz reciprocal theorem [93, Chapter 3-5]. For the case of the prolate spheroid with $\mathbf{U} = U\mathbf{e}_z$, this renders (for details see, e.g., Refs. [134, 140, 196])

$$U = -\frac{\tau_0}{2} \int_{-1}^1 d\zeta \sqrt{\frac{1 - \zeta^2}{\tau_0^2 - \zeta^2}} v_s(\zeta). \quad (6.9)$$

Therefore, \mathbf{U} can be considered as known; accordingly, the boundary value problem defined by Eqs. (6.1) - (6.4) is specified and the solution \mathbf{v} can be determined.

6.4.2 Stokes stream function and hydrodynamic flow

Since the boundary value problem defined by Eqs. (6.1) - (6.3) has axial symmetry, one searches for an axisymmetric solution $\mathbf{v}(\mathbf{r})$ expressed in terms of a Stokes stream function $\psi(\mathbf{r})$ as $\mathbf{v}(\mathbf{r}) = \nabla \times \frac{\psi(\mathbf{r})}{h_\varphi} \mathbf{e}_\varphi$ [93, Chapter 4]; this renders

$$v_\tau(\tau, \zeta) = \frac{1}{h_\zeta h_\varphi} \frac{\partial \psi}{\partial \zeta}, \quad (6.10)$$

$$v_\zeta(\tau, \zeta) = -\frac{1}{h_\tau h_\varphi} \frac{\partial \psi}{\partial \tau}. \quad (6.11)$$

The general “semiseparable” solution for the stream function in prolate coordinates has been derived by Ref. [50] in the form of a series representation

$$\begin{aligned}\psi(\tau, \zeta) = & g_0(\tau)G_0(\zeta) + g_1(\tau)G_1(\zeta) \\ & + \sum_{n=2}^{\infty} [g_n(\tau)G_n(\zeta) + h_n(\tau)H_n(\zeta)].\end{aligned}\quad (6.12)$$

where G_n and H_n are the Gegenbauer functions of the first and second kind, respectively (see Ref. [4]). The functions $g_n(\tau)$ and $h_n(\tau)$ are given by certain linear combinations of $G_k(\tau)$ and $H_k(\tau)$, the coefficients of which are fixed by the corresponding boundary conditions (see below).

The general solution above is applied to our particular system as follows. Noting that for our system the solution $\mathbf{v}(\mathbf{r})$ should be bounded (i.e., $|\mathbf{v}(\mathbf{r})| < \infty$ everywhere), none of the terms involving the Gegenbauer functions of the second kind $H_n(\zeta)$, which are divergent along the z -axis (i.e., $\zeta = \pm 1$) [93, Chapter 4-23], can be present in the solution; accordingly, $h_n(\tau) \equiv 0$ for all $n \geq 2$. Furthermore, due to the same requirement of bounded magnitude of the flow, the terms involving the Gegenbauer functions of the first kind $G_0(\zeta) = 1$ and $G_1(\zeta) = -\zeta$ also cannot be present in the solution because they lead to divergences of v_ζ at $\zeta = \pm 1$ (see Eqs. (6.11) and (6.7)); accordingly, $g_0(\tau) \equiv 0$ and $g_1(\tau) \equiv 0$. Therefore, for our system only the functions $g_{n \geq 2}$ will be of interest; these are given by [50]

$$\begin{aligned}g_2(\tau) = & \frac{C_2}{6}G_1(\tau) + C_4H_4(\tau) + D_2H_2(\tau) \\ & + F_2G_2(\tau) + E_4G_4(\tau) \\ g_3(\tau) = & -\frac{C_3}{90}G_0(\tau) + C_5H_5(\tau) + D_3H_3(\tau) \\ & + F_3G_3(\tau) + E_5G_5(\tau) \\ g_{n \geq 4}(\tau) = & C_{n+2}H_{n+2}(\tau) + C_nH_{n-2}(\tau) + D_nH_n(\tau) \\ & + F_nG_n(\tau) + E_{n+2}G_{n+2}(\tau) + E_nG_{n-2}(\tau),\end{aligned}\quad (6.13)$$

where the constants $\{C_n, D_n\}_{n \geq 2}$, $\{E_n\}_{n \geq 4}$, and $\{F_n\}_{n \geq 2}$, are fixed, as noted above, by requiring that the solution satisfies the BCs, Eqs. (6.3), and the force balance condition, Eq. (6.4).

Since the hydrodynamic force is proportional to the coefficient C_2 (see $g_2(\tau)$) [140], the force balance (Eq. (6.4)) implies

$$C_2 = 0. \quad (6.14a)$$

The boundary condition at infinity (Eq. (6.3b)) implies the asymptotic behavior of the stream function

$$\psi(\tau \rightarrow \infty, \zeta) \propto \frac{1}{2}Uc^2(\tau^2 - 1)(1 - \zeta^2);$$

by noting the asymptotic behaviors $G_n(\tau \gg 1) \propto \tau^n$ and $H_n(\tau \gg 1) \propto \tau^{-(n+1)}$ [4], this implies that the functions $g_{n \geq 2}(\tau)$ cannot have contributions from terms involving the

Gegenbauer functions $G_n(\tau)$ of index $n > 2$, i.e.,

$$E_n = 0, \quad n = 4, 5, \dots \quad \text{and} \quad F_n = 0, \quad n = 3, 4, \dots \quad (6.14b)$$

Furthermore, in order to exactly match the asymptotic $(\tau^2 - 1)(1 - \zeta^2)$ form and its prefactor, it is necessary that

$$F_2 = -2c^2 U. \quad (6.14c)$$

The impenetrability of the surface and Eq. (6.10) imply that $\psi(\tau_0, \zeta)$ is a constant; since $\psi(\tau_0, \pm 1) = 0$ as $G_n(\zeta = \pm 1) = 0$, one concludes that $\psi(\tau_0, \zeta) \equiv 0$ and thus

$$g_n(\tau_0) = 0, \quad n = 2, 3, \dots \quad (6.14d)$$

Finally, the tangential slip velocity condition at the surface of the particle (Eq. (6.3a)) together with: the expression for v_ζ in Eq. (6.11), the orthogonality of the Gegenbauer functions $G_{n \geq 2}(\zeta)$ (see Appendix 6.7.2), and the relation between the Gegenbauer functions $G_{n \geq 2}(\zeta)$ and the associated Legendre polynomials $P_{n \geq 1}^1(\zeta)$ (see the Appendix 6.7.2) leads to

$$\left. \frac{dg_n}{d\tau} \right|_{\tau=\tau_0} = c^2 \left(n - \frac{1}{2} \right) \int_{-1}^{+1} d\zeta (\tau_0^2 - \zeta^2)^{1/2} v_s(\zeta) P_{n-1}^1(\zeta),$$

$$n = 2, 3, \dots \quad (6.14e)$$

For given $v_s(\zeta)$, and with U determined by Eq. (6.9), Eqs. (6.14d) and (6.14e) provide a system of linear equations determining all the remaining unknown coefficients $\{C_{n \geq 3}, D_{n \geq 2}\}$, as detailed in the Appendix 6.7.3.

6.5 Squirmer and squirming modes

The form of Eq. (6.14e) suggests (for the expansion of the slip velocity \mathbf{v}_s) the functions

$$V_n(\zeta) := (\tau_0^2 - \zeta^2)^{-1/2} P_n^1(\zeta), \quad (6.15)$$

as a suitable basis over the space of square integrable functions $f(\zeta)$ satisfying $f(\zeta = \pm 1) = 0$ (note that V_n has a parametric dependence on $\tau_0 > 1$). Defining, in this space, the weighted scalar product

$$\langle f_1(\zeta), f_2(\zeta) \rangle_{w(\zeta)} := \int_{-1}^{+1} d\zeta w(\zeta) f_1(\zeta) f_2(\zeta), \quad (6.16)$$

and choosing the weight as

$$w(\zeta) = \tau_0^2 - \zeta^2 > 0, \quad (6.17)$$

one infers (from the known properties of the associated Legendre polynomials) that indeed the set $\{V_n\}_{n \geq 1}$ is an orthogonal basis,

$$\langle V_n(\zeta), V_m(\zeta) \rangle_{w(\zeta)} = \frac{n(n+1)}{n+1/2} \delta_{n,m}. \quad (6.18)$$

Accordingly, the slip velocity function $\mathbf{v}_s = v_s(\zeta) \mathbf{e}_\zeta$ has a unique representation in terms of a series in the functions $\{V_n\}_{n \geq 1}$,

$$v_s(\zeta) = \tau_0 \sum_{n \geq 1} B_n V_n(\zeta). \quad (6.19)$$

The coefficients of the expansion are written in the form above to ensure that in the limit of a sphere ($b_x \rightarrow b_z$, i.e. $\tau_0 \rightarrow \infty$) one arrives at the usual form employed for a spherical squirmer, i.e., that of an expansion in associated Legendre polynomials $P_n^1(\cos \vartheta)$ (see, e.g., Ref. [25, 102]). This can be seen by noticing that in the limit $\tau_0 \rightarrow \infty$ one has $\tau_0(\tau_0^2 - \zeta^2)^{-1/2} P_n^1(\zeta) \rightarrow P_n^1(\zeta)$ and that $b_x \rightarrow b_z$ implies $\zeta \rightarrow \cos(\vartheta)$; accordingly, it follows that, in the limit of the shape approaching that of a sphere, $\tau_0 V_n(\zeta) \mathbf{e}_\zeta \rightarrow -P_n^1(\cos \vartheta) \mathbf{e}_\vartheta$ and the expansion in Ref. [25] is matched identically upon changing $B_n \rightarrow \frac{2}{n(n+1)} B_n$.

With the representation of the slip velocity in terms of the function V_n , Eq. (6.19), upon exploiting the orthogonality relation (Eq. (6.18)) the boundary condition in Eq. (6.14e) renders the simple relations

$$\left. \frac{\partial g_n(\tau)}{\partial \tau} \right|_{\tau=\tau_0} = \tau_0 c^2 n(n-1) B_{n-1}, \quad n = 2, 3, \dots \quad (6.20)$$

For a given slip velocity, thus a given set of amplitudes B_n of the slip modes $V_n(\zeta)$, Eqs. (6.14d) and (6.20) evaluated for $n \geq 1$ provide a system of coupled linear equations for the last unknown coefficients in the stream function, $C_{n \geq 3}$ and $D_{n \geq 2}$. Inspection of this system reveals that it splits into two subsystems of coupled equations, one involving only the coefficients of even index, $n = 2k$, and the other one involving only the coefficients of odd index $n = 2k + 1$ (see Appendix 6.7.3). Furthermore, from Eq. (6.20) it can be inferred that in the case that the slip velocity is given by a pure slip mode $V_{n_0}(\zeta)$, i.e., $B_n = \delta_{n,n_0}$ for $n \geq 1$, then the parity of n_0 selects one of the two subsystems. If n_0 is even, then all the coefficients C_k and D_k of even index k vanish and the stream function, Eq. (6.12), involves only the functions g_k of odd index k , while for odd n_0 all the coefficients C_k and D_k of odd index k vanish and the stream function, Eq. (6.12), involves only the functions g_k of even index k . Finally, we note that a pure slip mode $V_{n_0}(\zeta)$ selects, as discussed above, either the odd or even number terms in the series representation of the the stream function, Eq. (6.12), but not only a single squirmer mode, as it is the case for the spherical squirmer. Accordingly, even simple distributions of active slip velocities on the surface of the particle can give rise to quite complex hydrodynamic flows around the squirmer.

With these general results, we can proceed to the discussion of prolate squirmers. We will

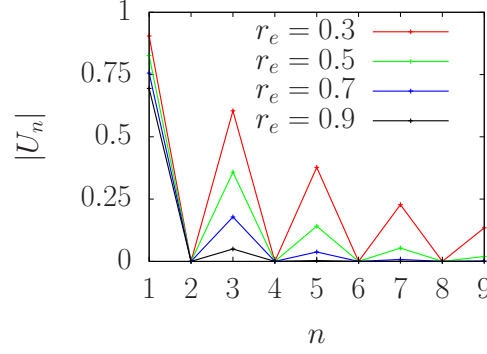


Figure 6.2: The absolute value $|U_n|$ (Eq. (6.21)) of the contribution of the slip modes $n = 1, 3, 5, 7$ to the velocity of a prolate spheroid for aspect ratios $r_e = 0.3, 0.5, 0.7, 0.9$. The lines represent only a guide to the eye.

focus on the usual quantities employed to characterize an axisymmetric squirmer [25, 65, 145], i.e., the velocity U of the squirmer, the magnitude S of the stresslet associated with the squirmer (which determines the far-field hydrodynamic flow of the squirmer), and the general characteristics of the hydrodynamic flow $\mathbf{v}(\mathbf{r})$ around the squirmer.

By combining Eqs. (6.14e), (6.19), (6.18), and (6.15), and noting that the polynomials $P_n^1(x)$ are even (odd) functions of x for n odd (even), one arrives at

$$\begin{aligned}
 U(\tau_0) &= \frac{\tau_0^2}{2} \sum_{n \geq 1, n \text{ odd}} B_n \int_{-1}^1 dx \frac{P_1^1(x) P_n^1(x)}{\tau_0^2 - x^2} \\
 &= \sum_{n \geq 1, n \text{ odd}} B_n U_n(\tau_0).
 \end{aligned} \tag{6.21}$$

Accordingly, it follows that (a) a squirmer may exhibit self-motility (i.e., $U \neq 0$) only if the slip velocity involves at least an odd index n slip mode V_n ; (b) in contrast to the case of a spherical squirmer, for which the velocity is determined solely by the slip mode $n = 1$ irrespective of the details of the slip velocity \mathbf{v}_s , for a spheroidal squirmer all the slip modes of odd index contribute to the velocity (see also Fig. 6.2); consequently, (c) spheroidal squirmers with $B_1 = 0$ can be self-motile (due to contributions from other odd index slip modes), and spheroidal squirmers with $B_1 \neq 0$ can yet be non-motile if the contributions from other slip modes of odd index n precisely balance the contribution of the mode B_1 (which clearly pinpoints the shortcomings of a model with only two slip modes as in Ref. [231]).

In terms of the dependence on the slenderness parameter r_e (which determines the value of τ_0 , see Eq. (6.8)), there are two findings. (d) for every slip mode n , the contribution $|U_n|$ (in absolute value) is a decreasing function of r_e (see Fig. 6.2); second, (e) while at low values of the aspect ratio the contributions $|U_n|$ of the $n > 1$ slip modes are significant, the contributions from the modes $n \geq 3$ decay steeply with increasing r_e and become negligible, compared to $|U_1|$ (which remains non-zero), as the aspect ratio r_e of the spheroid approaches that of a sphere ($r_e \rightarrow 1^-$). This ensures a smooth transition into the spherical case, where,

as previously mentioned, higher mode squirmers are not motile and $U \propto B_1$. Finally, we note that, by comparison with the expression in Eq. (6.14c), one infers that the series in the last line of Eq. (6.21) is proportional to the coefficient F_2 in the expansion of the stream function.

In what concerns the stresslet $S(\tau)$, which (similarly to the case of a spherical squirmer) allows classification into pullers (positive stresslet, $S > 0$), pushers (negative stresslet, $S < 0$), and neutral swimmers (vanishing stresslet, $S = 0$), we note that it can also be expressed in terms of the slip velocity $u_s(\zeta)$ as [134]:

$$\begin{aligned} S &= -\frac{2A\mu}{F(r_e^{-1})J(r_e^{-1})} \int_{-1}^1 u_s(\zeta) \zeta \sqrt{\frac{r_e^{-2}(1-\zeta^2)}{\zeta^2 + r_e^{-2}(1-\zeta^2)}} d\zeta \\ &= \sum_{n \geq 1, n \text{ even}} \mu B_n S_n(\tau_0) \end{aligned} \quad (6.22)$$

where A denotes the surface area of the spheroid and

$$\begin{aligned} F(x) &= \frac{1}{(x^2 - 1)^2} \left(-3x^2 + \frac{x(1 + 2x^2)}{\sqrt{1 - x^2}} \cos^{-1}(x) \right), \\ J(x) &= 1 + \frac{x^2}{\sqrt{x^2 - 1}} \cos^{-1}\left(\frac{1}{x}\right). \end{aligned}$$

As in the case of the velocity, there are certain significant differences from the case of a spherical squirmer (see Fig. 6.3): (a) a necessary condition for a prolate squirmer to exhibit a nonvanishing stresslet is that at least one even ($k = 2n$) mode V_k contributes to the slip velocity; (b) as for the velocity U (where more than a single mode contributes), the stresslet depends on all even squirmer modes; hence, (c) the stresslet contribution of $B_2 \neq 0$ can be offset or even inverted by other even, active modes $B_k \neq 0$; (d) At a given aspect ratio r_e , the contribution (in absolute value) $|S_{2n}|$ is a decreasing function of n ; and (e) while for elongated shapes (small values r_e) the contributions $|S_n|$ from the slip modes $n \geq 4$ are significant,

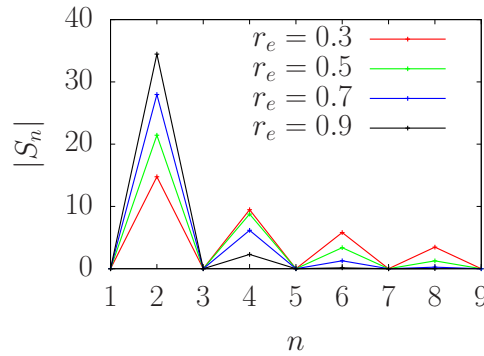


Figure 6.3: The absolute value $|S_n|$ (Eq. (6.22)) of the contribution of the slip modes $n = 1, 3, 5, 7$ to the stresslet of a prolate squirmer for aspect ratios $r_e = 0.3, 0.5, 0.7, 0.9$. The lines represent only a guide to the eye. This figure has been updated compared to the published version.

these contributions are steeply decreasing towards zero with increasing r_e towards the value 1^- . In contrast, $|S_2|$ is increasing with r_e . As in the case of the velocity, this behavior ensures the smooth transition to the case of a spherical shape, where $S \propto B_2$.

Since the stresslet is, by definition, the amplitude of the r^{-2} far-field term in the flow field (in the lab frame) of the squirmer, the series in the last line of Eq. (6.22) can be connected with one of the coefficients in the expansion of the stream function as follows. In the laboratory frame, which is related to the one (ψ_{particle}) in the co-moving frame via

$$\psi_{\text{lab}} = \psi_{\text{particle}} + \frac{1}{2}U_0(1 - r_e^2)(\tau^2 - 1)(1 - \zeta^2), \quad (6.23)$$

the slowest decaying term with the distance τ from the squirmer is $-\frac{C_3}{90}G_0(\tau)G_3(\zeta)$; by Eq. (6.10), this term leads to a contribution $\sim C_3/\tau^2$ to the flow. Accordingly, $S \propto C_3$ and the pusher or puller squirmers ($S \neq 0$) indeed exhibit the expected far-field hydrodynamics, while for the neutral squirmers ($S = 0$) the far-field flow necessarily decays at least as $\sim 1/\tau^3$.

Turning now to the flow field around the prolate squirmer, we will discuss separately the flow fields generated by the first few pure slip modes, i.e., the cases $B_n = \delta_{n,n_0}$ with $n_0 = 1, 2, 3, 4$; these flows are shown, in the laboratory frame, in Fig. 6.4. From the discussion above, we know that only a subset (either the odd index ones, if n_0 is even, or vice versa) of the terms in the series representation, Eq. (6.12), of the stream functions contributes to the flow. Since the metric factors are even functions of ζ , while $G_n(\zeta)$ is an odd (even) function of ζ when n is odd (even), the flow has the following fore-aft symmetries. For n_0 odd, the stream function involves the functions G_k of index k an even number, and thus $\psi(\tau, \zeta) = \psi(\tau, -\zeta)$; this implies $v_\tau(\tau, \zeta) = -v_\tau(\tau, -\zeta)$ and $v_\zeta(\tau, \zeta) = v_\zeta(\tau, -\zeta)$ (see figures 6.5 and 6.6); i.e., the z - (x -) flow components are fore-aft (anti)symmetric (see Fig. 6.4), and, accordingly, it contributes to the motility because it provides a “fore to back” streaming. Vice versa, for n_0 an even number one has $v_\tau(\tau, \zeta) = v_\tau(\tau, -\zeta)$ and $v_\zeta(\tau, \zeta) = -v_\zeta(\tau, -\zeta)$, i.e., the x - (z -) flow component are fore-aft symmetric (see Fig. 6.4); consequently, they cannot be associated to a motile particle.

Finally, we note that the similar analysis and results for the case of an oblate squirmer can be obtained from the available ones for a prolate squirmer via a simple transformation of the coordinates system and of the stream function (i.e., a mapping), as discussed in the Appendix 6.7.1. As an illustration of using this mapping, the results shown in Fig. 6.4, corresponding to a prolate squirmer, have been used to determine the flows around the corresponding (i.e., of slenderness parameters $r'_e = 1/r_e$) oblate squirmers induced by the pure slip modes $B_n = \delta_{n,n_0}$ with $n_0 = 1, 2, 3, 4$; these are shown in Fig. 6.9. The analysis of the velocity U and stresslet S (see Figs. 6.7 and 6.8) for oblate spheroids leads to conclusions that are similar with those drawn in the case of prolate shapes. The only significant difference is that now for oblate squirmers the contributions of from the higher orders n slip modes decay to zero with *decreasing* aspect ratio $r_e \rightarrow 1^+$; again, this ensures a smooth transition to the case of a spherical shape, where only B_1 or B_2 are relevant.

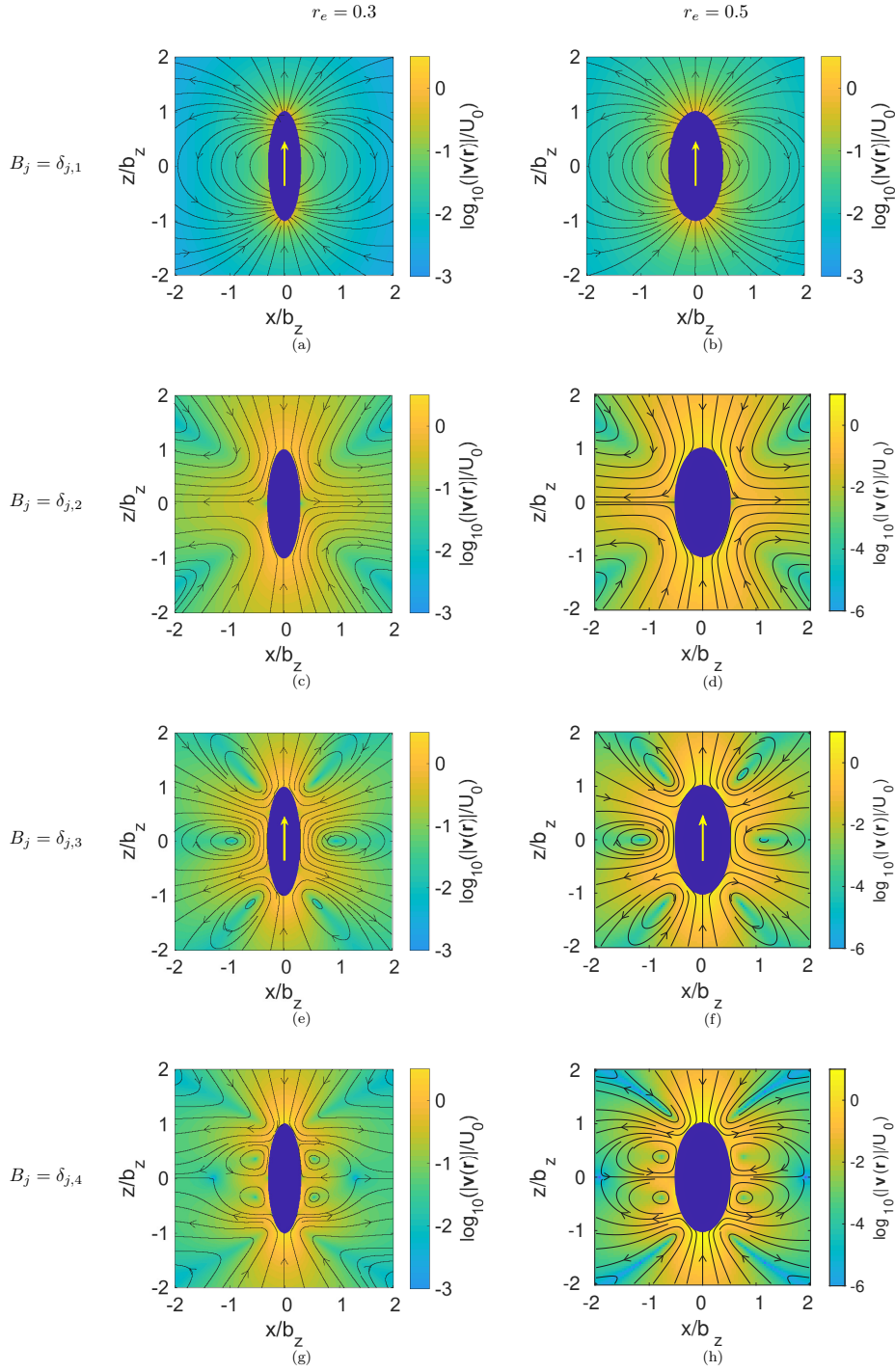


Figure 6.4: The flow field (streamlines and velocity magnitude (color coded background)) induced by a prolate spheroid with $B_n = \delta_{n,n_0}$ for (top to bottom) $n_0 = 1, 2, 3, 4$ and aspect ratio $r_e = 0.3$ (left column) and $r_e = 0.5$ (right column), respectively. The results are shown in the laboratory frame and are obtained by using the series representation of the stream function (see the main text). The arrows on the particles indicate the directions of their motion.

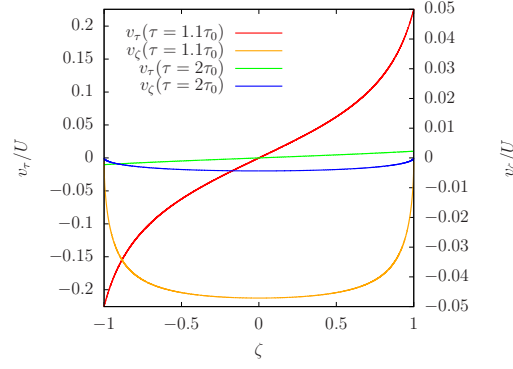


Figure 6.5: Velocity components v_τ and v_ζ on the iso-surfaces $\tau = 1.1\tau_0$ and $\tau = 2\tau_0$ near a prolate spheroid with $B_n = \delta_{n,1}$.

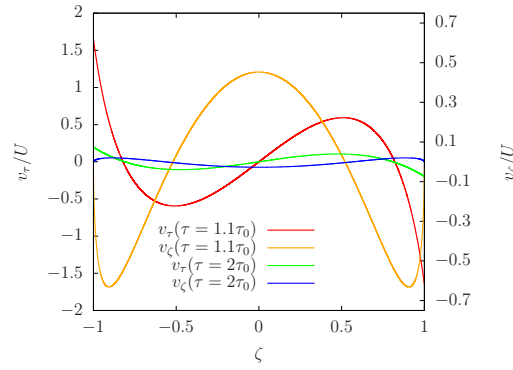


Figure 6.6: Velocity components v_τ and v_ζ on the iso-surfaces $\tau = 1.1\tau_0$ and $\tau = 2\tau_0$ near a prolate spheroid with $B_n = \delta_{n,3}$.

6.5.1 Self-phoretic particle

Squirmer with a wide range of active slip modes occur naturally in the context of model self-phoretic particles. One of the often employed realizations of such systems consists of micrometer-sized silica or polystyrene spherical particles partially coated with a Pt layer and immersed in an aqueous peroxide solution [16, 96, 221]. The catalytic decomposition of the peroxide at the Pt side creates gradients in the chemical composition of the suspension; as in the case of classic phoresis [7], these gradients, in conjunction with the interaction between the colloid and the various molecular species in solution, give rise to self-phoretic motility [80]. The mechanism of steady-state motility can be intuitively understood in terms of the creation of a so-called phoretic slip velocity tangential to the surface of the particle [7, 51, 81]. For such chemically active, axi-symmetric, spherical particles in unbounded solutions, the approximation of phoretic slip velocity leads to a straightforward mapping [157, 194] onto a squirmer model; accordingly, the translational velocity of the particle and the hydrodynamic flow around the particle in terms of the phoretic slip can be directly inferred from the corresponding results in Ref. [25].

A similar mapping can be developed from a spheroidal, self-phoretic colloid to a spheroidal

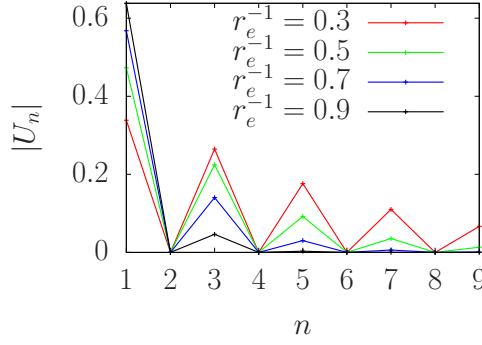


Figure 6.7: The absolute value $|U_n|$ of the contribution of the slip modes $n = 1, 3, 5, 7$ to the velocity of an oblate squirmer for aspect ratios $r_e^{-1} = 0.3, 0.5, 0.7, 0.9$. The lines represent only a guide to the eye. This figure has been updated compared to the published version.

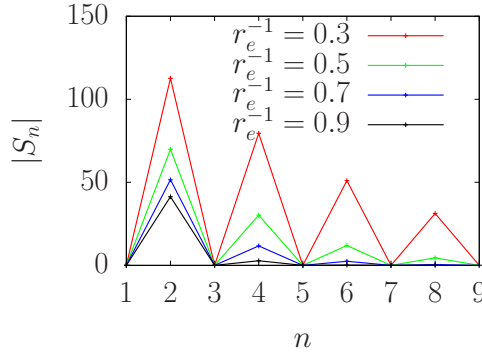


Figure 6.8: The absolute value $|S_n|$ of the contribution of the slip modes $n = 1, 3, 5, 7$ to the stresslet of an oblate squirmer for aspect ratios $r_e^{-1} = 0.3, 0.5, 0.7, 0.9$. The lines represent only a guide to the eye. This figure has been updated compared to the published version.

squirmer model for spheroidal, chemically active colloids. Following Ref. [196] the slip velocity of such particles can be written as

$$v_S(\mathbf{r}_P) = \sum_{l \geq 0} \frac{b}{c} c_l(\chi) Q_l(\tau_0) P_l^1(\zeta) (\tau_0^2 - \zeta^2)^{-\frac{1}{2}}, \quad (6.24)$$

where b is the so-called phoretic mobility (for simplicity, here assumed to be a constant) over the surface of the particle, and $Q_l(\tau)$ denotes the Legendre polynomial of the second kind [4]. The coverage $\chi = h - 1$ is defined in terms of the height of the active cap (measured, from the bottom apex, in units of b_z), i.e., $\chi = -1$ corresponds to a chemically inactive spheroid and $\chi = +1$ corresponds to all the surface being active. The coverage dependent coefficients $c_l(\chi)$ (see Ref. [196]) describe the decoration of the surface of the particle by the chemically active element (e.g., Pt in the example discussed above) as an expansion in Legendre polynomials $P_l(\zeta)$. Knowledge of these parameters allows us to formulate a slip

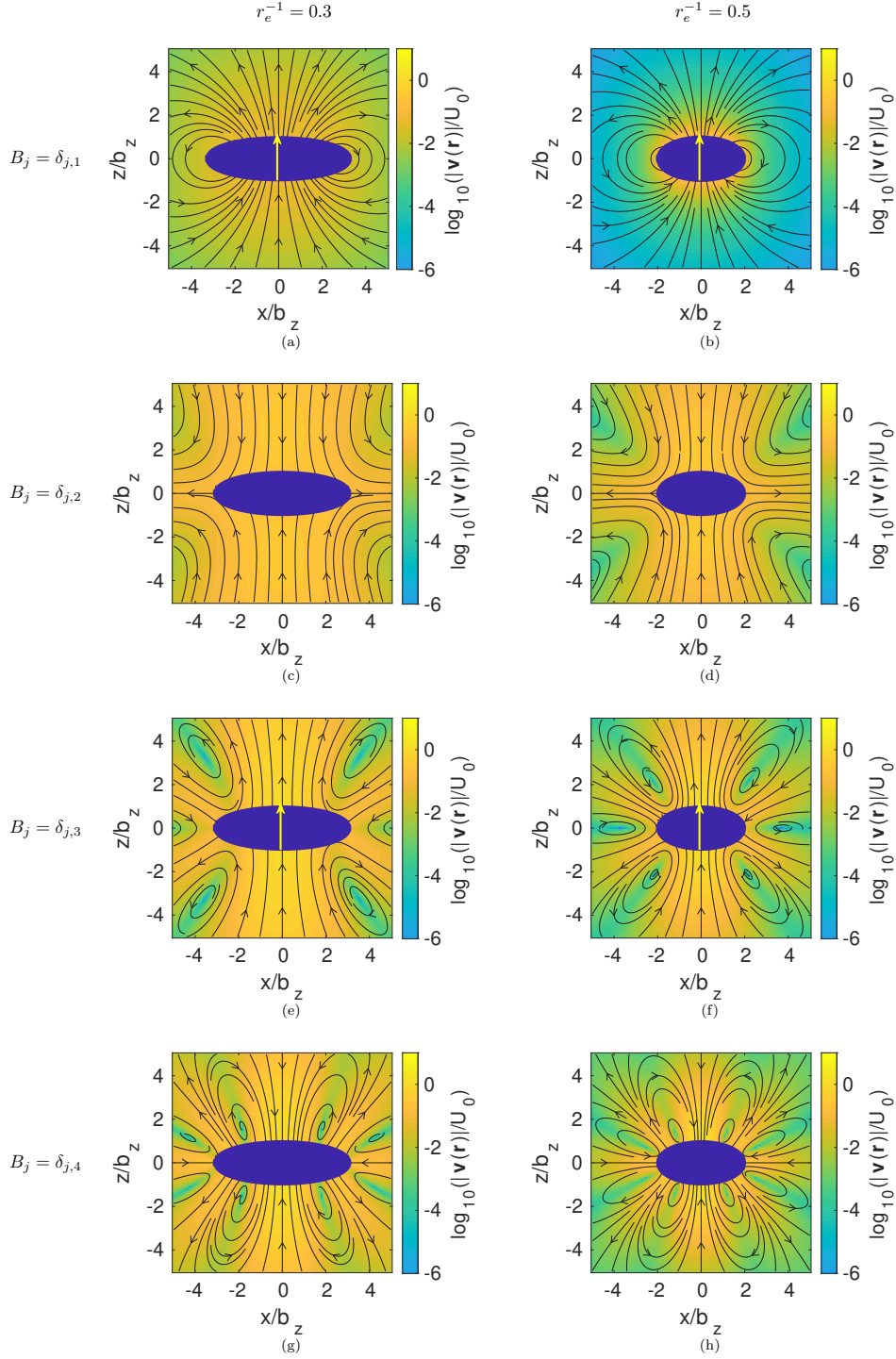


Figure 6.9: The flow field (streamlines and velocity magnitude (color coded background)) induced by an oblate squirmer with $B_n = \delta_{n,n_0}$ for (top to bottom) $n_0 = 1, 2, 3, 4$ and aspect ratio $r_e^{-1} = 0.3$ (left column) and $r_e^{-1} = 0.5$ (right column), respectively. The results are shown in the laboratory frame and are obtained by using the mapping discussed in the main text and the flows of the corresponding prolate squirmers shown in Fig. 6.4. The arrows on the particles indicate the directions of their motion.

velocity boundary condition similar to (6.20), i.e.

$$\left. \frac{\partial g_n(\tau)}{\partial \tau} \right|_{\tau=\tau_0} = \tau_0 c^2 n(n-1) \tilde{B}_{n-1}; \quad (6.25)$$

by identifying the effective squirmer modes $\tilde{B}_l = \frac{b}{c \cdot \tau_0} c_l Q_l(\tau_0)$, the desired mapping is achieved. As an illustration of this mapping, we show in Fig. 6.10 (left column) the flow fields for particles with parameters $r_e = 0.3, 0.5$ and $\chi = 0, -0.3$, respectively, and compare with the corresponding results obtained by direct numerical solutions obtained using BEM [198]. (Note that, if necessary, the accuracy of the analytical estimate can be systematically improved simply by increasing the order of the truncation in the series expansion of the stream function (see the Appendix 6.7.4)).

6.6 Summary and conclusion

We have studied in detail the most general axi-symmetric spheroidal squirmer and we have shown that, in analogy with the situation for spherical shapes [157], model chemically active, self-phoretic colloids can be mapped onto squirmers. By using the semiseparable ansatz derived in Ref. [50] for the stream function, and representing the active slip (squirming) velocity of the squirmer in a suitable basis (Eq. (6.19), chosen such that in the limit of a spherical shape it smoothly transforms into the usually employed expansion for the classical spherical squirmer [25], the velocity of the squirmer, the stresslet of the squirmer, and the hydrodynamic flow around the squirmer have been determined analytically (Sec. 6.5). The corresponding series representations have been validated by cross-checking against direct numerical calculations, obtained by using the BEM, of the flow around the squirmer (Appendix 6.7.5).

The main conclusion emerging from the study is that for spheroidal squirmers (or self-phoretic particles) the squirming modes beyond the second are, in general, as important as the first two ones in what concerns the contributions to the velocity and stresslet of the particle (and, implicitly, to the flow field around the particle, even in the far-field). The velocity is contributed by all the odd-index components (but none of the even-index ones) of the slip velocity; accordingly, in contrast with the case of spherical squirmers, it is possible to have spheroidal squirmers with a non-zero first mode and yet not motile, as well as ones missing the first slip mode and yet motile. Similarly, the stresslet value is contributed by all the even-index slip modes; thus, distinctly from the case of spherical squirmers, one can have pushers/pullers even if the second slip mode is vanishing, as well as neutral squirmers in spite of a non-vanishing second slip mode. Finally, even a single slip mode leads to a large number of non-vanishing terms in the series expansion of the stream function, and thus spheroidal squirmers with simple distributions of slip on their surface can lead to very complex flows around them (see Figs. 6.4 and 6.9).

This raises the interesting speculative question as whether the spheroidal shape is providing an evolutionary advantage; i.e., with small modifications of the squirming pattern, e.g.,

switching from a sole B_1 mode to a sole B_3 mode, a microorganism could maintain its velocity unchanged but dramatically alter the topology of the flow around it (compare the first and third rows in Fig. 4). In other words, compared to a squirmer with spherical shape, for which multiple modes must be simultaneously activated in order to change the structure of the flow, a spheroidal squirmer possesses simple means for acting in hydrodynamic disguise, which can be advantageous as either predator or prey.

6.7 Appendices

6.7.1 Oblate spheroids

The similarity between oblate and prolate spheroids allows us to obtain the flow field around an oblate microswimmer of aspect ratio $r'_e > 1$ as a series in the oblate coordinates by using a mapping from the results, in prolate coordinates, corresponding to a prolate microswimmer with aspect ratio $r_e = 1/r'_e < 1$ (and vice versa).

The oblate spheroidal coordinate system is defined by

$$\begin{aligned}\lambda &= \frac{1}{2\bar{c}}(\sqrt{x^2 + y^2 + (z - i\bar{c})^2} + \sqrt{x^2 + y^2 + (z + i\bar{c})^2}), \\ \zeta &= \frac{1}{-2i\bar{c}}(\sqrt{x^2 + y^2 + (z - i\bar{c})^2} - \sqrt{x^2 + y^2 + (z + i\bar{c})^2}), \\ \varphi &= \arctan\left(\frac{y}{x}\right),\end{aligned}$$

with $0 \leq \lambda \leq \infty$ and $\bar{c} = \sqrt{r_e'^2 - 1}$, and the corresponding Lamé metric coefficients are given by

$$\begin{aligned}h_\zeta &= \bar{c} \frac{\sqrt{\lambda^2 + \zeta^2}}{\sqrt{1 - \zeta^2}}, \quad h_\lambda = \bar{c} \frac{\sqrt{\lambda^2 + \zeta^2}}{\sqrt{\lambda^2 + 1}}, \\ h_\varphi &= \bar{c} \sqrt{\lambda^2 + 1} \sqrt{1 - \zeta^2}.\end{aligned}\tag{6.26}$$

Noting that the oblate coordinates and the metric factors can be obtained from the expressions of the corresponding prolate coordinates via the transformations [50]

$$\tau \rightarrow i\lambda \quad c \rightarrow -i\bar{c},\tag{6.27}$$

one concludes that the equation and boundary conditions obeyed by the stream function in oblate coordinates in the domain outside the oblate of aspect ratio $r'_e = 1/r_e$ can be obtained, by using the same transformation, from the ones in prolate coordinates outside a prolate of aspect ratio r_e . Accordingly, it follows that $\psi_{\text{obl}, r'_e = 1/r_e}(\lambda, \zeta) = \psi_{\text{pro}, r_e}(\tau = i\lambda, \zeta)$. The flow

field then follows as the curl of the stream function, i.e.,

$$\mathbf{v}_{\text{obl},r'_e}(\lambda, \xi, \varphi) = \nabla \times \left(\frac{\psi_{\text{obl},r'_e}(\lambda, \xi)}{h_\varphi} \mathbf{e}_\varphi \right). \quad (6.28)$$

6.7.2 Gegenbauer functions

The Gegenbauer functions of first kind G_n , are also known as the Gegenbauer polynomials C_n^α with parameter $\alpha = -1/2$ [4]; they are defined in terms of the Legendre polynomials P_n as

$$G_n(x) = \frac{1}{2n-1} (P_{n-2}(x) - P_n(x)) , \quad (6.29a)$$

and fulfill the orthogonality relation

$$\int_{-1}^1 \frac{G_n(x)G_m(x)}{1-x^2} dx = \frac{2}{n(n-1)(2n-1)} \delta_{n,m} \quad n, m \geq 2. \quad (6.30)$$

The Gegenbauer functions can be related to the associated Legendre polynomials P_n^1 , which are defined in terms of the Legendre polynomials P_n as

$$(1-x^2)^{1/2} P_l^1 = -(1-x^2) \frac{d}{dx} P_l(x).$$

Using the relations $\frac{x^2-1}{n} \frac{d}{dx} P_n(x) = xP_n(x) - P_{n-1}(x)$ and $(n+1)P_{n+1}(x) = (2n+1)xP_n(x) - nP_{n-1}(x)$, one arrives at the following relation between the l -th associated Legendre polynomial and the $l+1$ -th Gegenbauer function.

$$(1-x^2)^{1/2} P_l^1 = -(l^2 + l) G_{l+1}(x)$$

6.7.3 Decoupling of the even- and odd-index modes in the stream function expansion

The coefficients C_n and D_n appear in the functions $g_k(\tau)$, entering the series expansion of the stream function at various indexes k (e.g., $C_{n \geq 4}$ appears at both $k = n-2$ and $k = n$); thus the infinite system of linear equations is strongly coupled. However, since the even and odd terms are not entering the same equations, the system splits into two decoupled subsystems, which are solved by using different methods.

The first subsystem consists of the even numbered terms in the series expansion of $\psi(\tau, \xi)$ and the set of conditions (Eqs. (6.14a), (6.14c), (6.14d) and (6.20)). Because each of the Eqs. (6.14a) and (6.14c) fix one of the even index coefficients (i.e., C_2 and F_2), the Eqs. (6.14d) and (6.20) evaluated at $n = 2$ involve only two unknowns, C_4 and D_2 , and thus can be solved as a sub-subsystem. With C_4 and D_2 known, the rest of the coefficients, up to the order N_{max} at which the system is truncated (i.e., B_k is set to zero for $k > N_{\text{max}}$), are solved iteratively by noting that Eqs. (6.14d) and (6.20) evaluated at $k = n$ involve only two unknowns, the rest of the coefficients being already determined in the previous iterations up to $k = n-2$.

The second subsystem includes all odd-index terms in the series expansion of $\psi(\tau, \zeta)$ and Eqs. (6.14d) and (6.20). Complementing the previous case, only the even squirmer modes contribute. However, unlike in the case of the first subsystem, there are no lower level decouplings; accordingly, this subsystem is solved in the standard manner by truncation at the cut-off N_{max} (above which all the coefficients are set to zero) and inversion of the resulting finite system of linear equations.

The choice of N_{max} is done by varying the value of the cut-off and testing the changes in the coefficients. For the cases we analyzed in this work, a value $N_{max} = 16$ was found to be sufficient.

6.7.4 Example of effects of too strong truncations for the case self-phoretic particles

To show the importance of the higher orders in the case of a self-phoretic swimmer, we compare the analytic results for keeping different numbers of squirmer modes B_n in figure 6.11. Even for an aspect ratio $r_e = 0.8$ (i.e., close to a spherical shape), the higher orders have significant influence on the flow field around the particle: e.g., compare the occurrence of a region of high magnitude flow near the point $(0, -1.5)$ (behind the particle) instead of the correct location at near the point $(0, 1.5)$ (in front of the particle).

6.7.5 Quantitative comparison to BEM

In figures 6.12 - 6.14 we present a more detailed comparison of the results obtained by using the series representation (top row) with numerical results obtained by using the BEM to directly solve the governing equations (second row). In addition, the relative error, defined as

$$\Delta v = \frac{\sqrt{(v_{x,ana} - v_{x,num})^2 + (v_{z,ana} - v_{z,num})^2}}{\frac{1}{2}(\sqrt{v_{x,ana}^2 + v_{z,ana}^2} + \sqrt{v_{x,num}^2 + v_{z,num}^2})} \quad (6.31)$$

is shown in the bottom row. The comparison confirms the expected quantitative agreement, with regions of significant relative error ($\Delta v > 10^{-1}$) corresponding precisely to the regions where the flow is anyway very weak ($|\frac{v(r)}{U}| < 10^{-3}$).

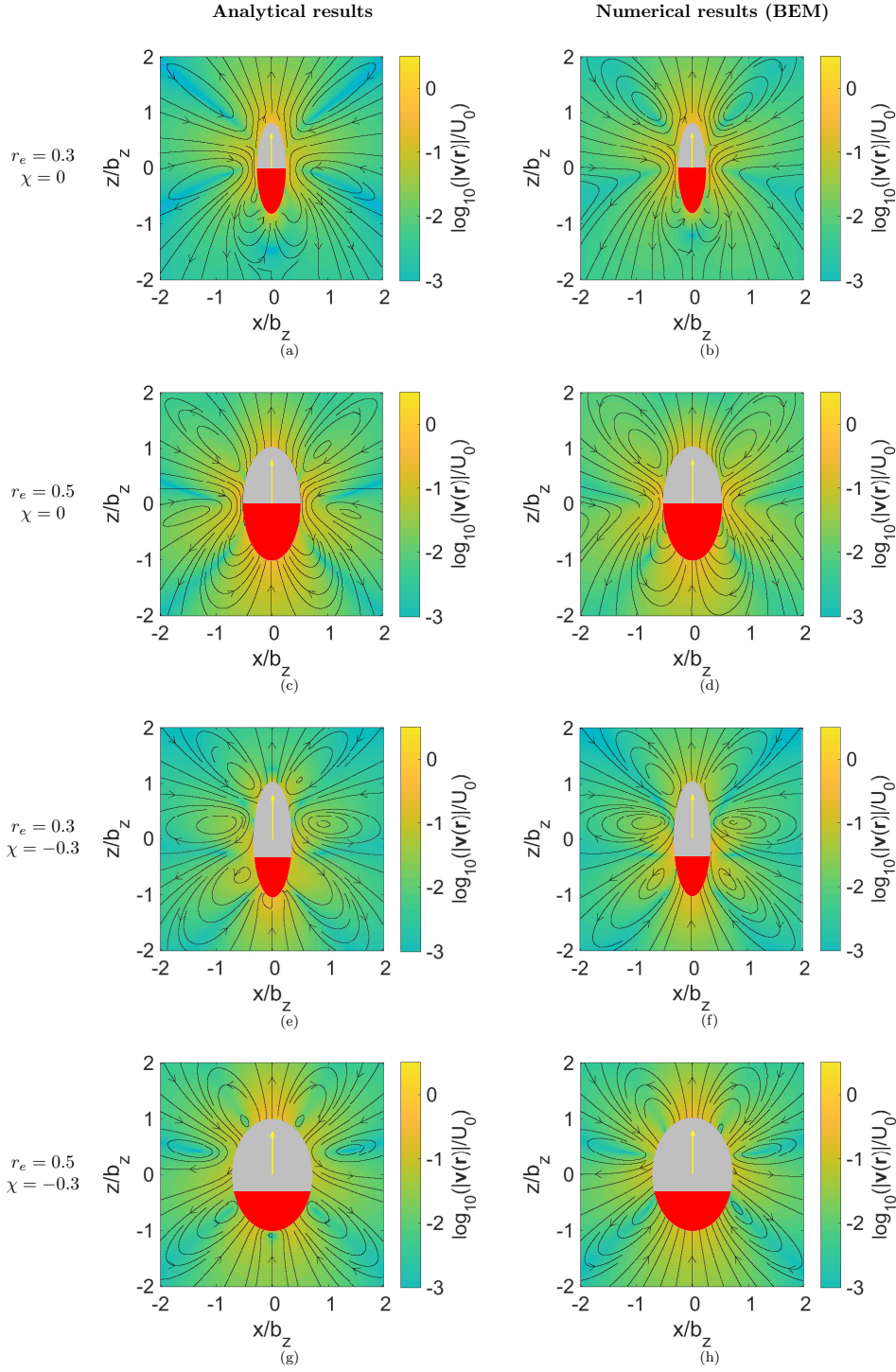


Figure 6.10: The flow field (streamlines and velocity magnitude (color coded background)) induced by a chemically active prolate particle moving by self-phoresis, calculated either analytically via the stream function (left column) or numerically, i.e., by directly solving the corresponding Laplace and Stokes equations using the BEM [198] (right). The results shown correspond to the cases of half ($\chi = 0$, top two rows) and less than half ($\chi = -0.3$, bottom two rows) coverage, and two values, $r_e = 0.3$ and $r_e = 0.5$, of the aspect ratio, respectively. The arrows on the particles indicate the directions of their motion. The red area depicts the chemically active region. The motion of the particle and the direction of the flow corresponds to the choice $b < 0$; the characteristic velocity U_0 is defined as in Ref. [196]

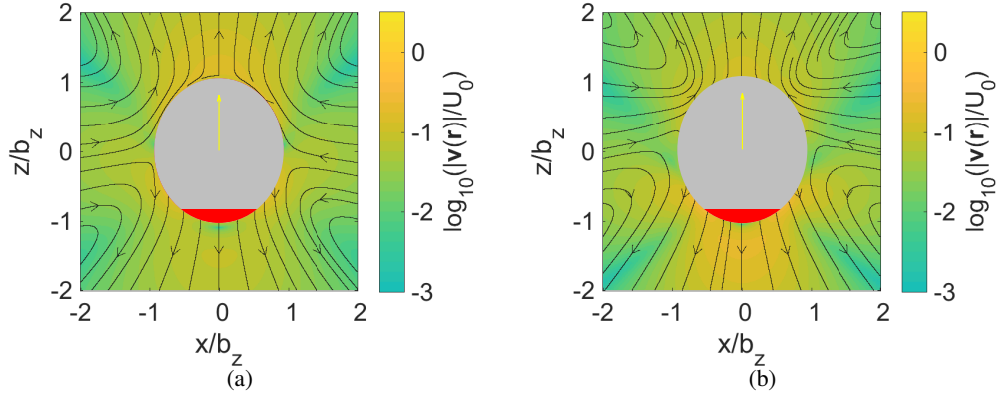


Figure 6.11: The flow field around a self-phoretic particle ($\chi = 0.8$, $r_e = 0.9$) when keeping the first (a) two and (b) eight terms (effective squirmer modes) in the series expansion of the stream function. The red area depicts the chemically active region.

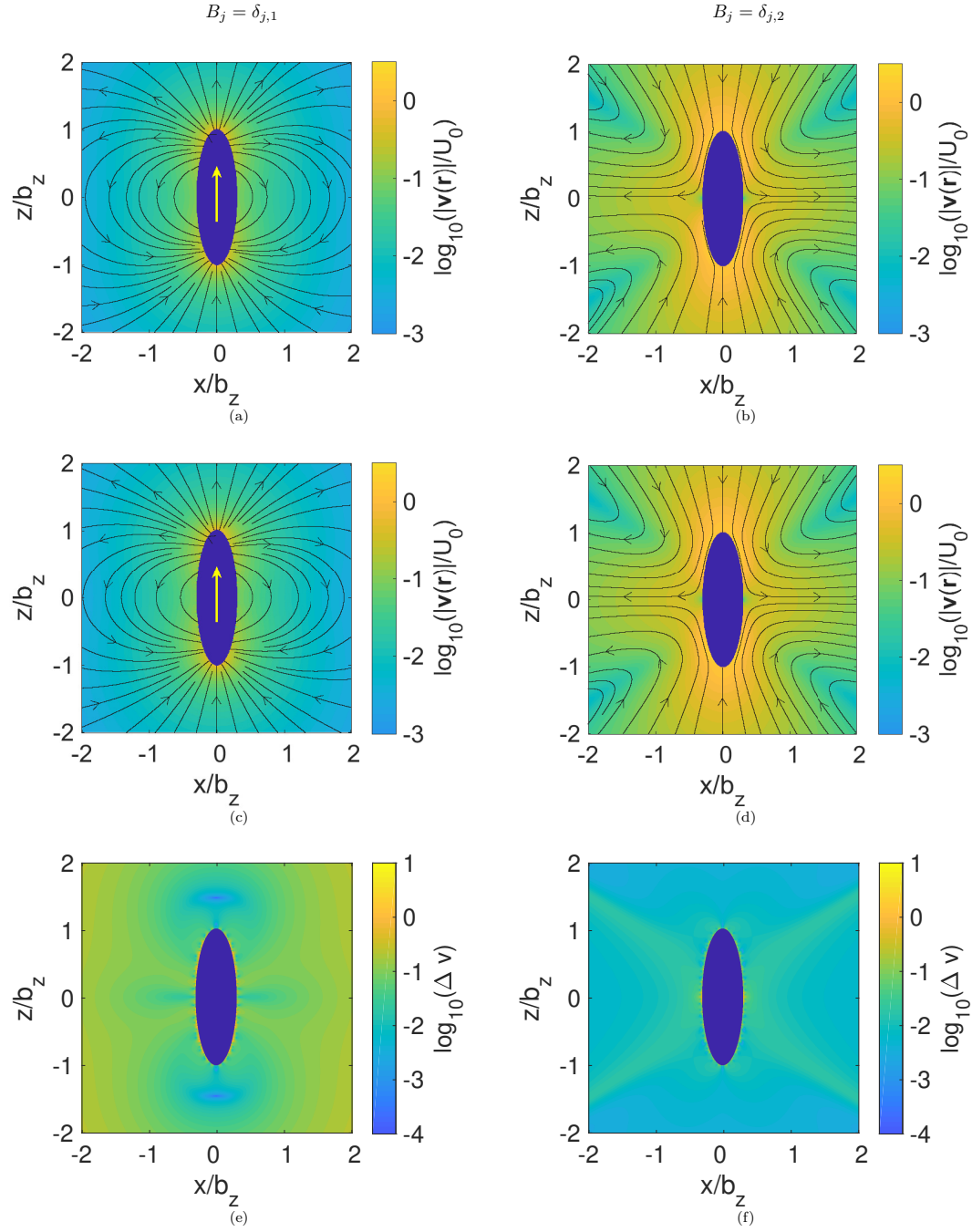


Figure 6.12: The flow field around a prolate spheroid with $r_e = 0.3$; in the left column only the first slip mode is active, and on the right column only the second slip mode is active. In both cases the analytical results are shown in the top row, the numerical results (BEM [198]) in the middle row, and the relative error between the two (Eq. (6.31)) in the bottom row.

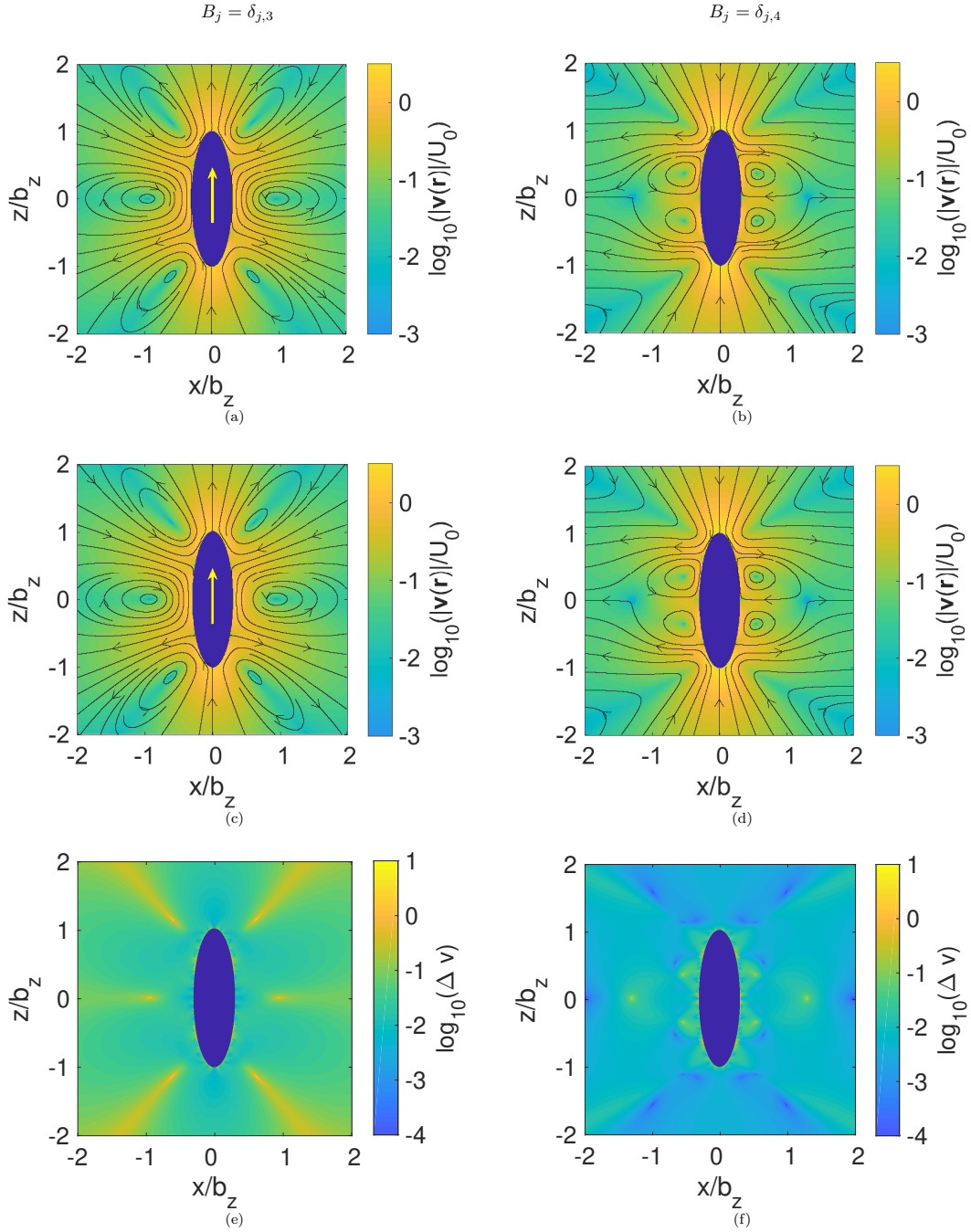


Figure 6.13: The flow field around a prolate spheroid with $r_e = 0.3$; in the left column only the third slip mode is active, and on the right column only the fourth slip mode is active. In both cases the analytical results are shown in the top row, the numerical results (BEM [198]) in the middle row, and the relative error between the two (Eq. (6.31)) in the bottom row.

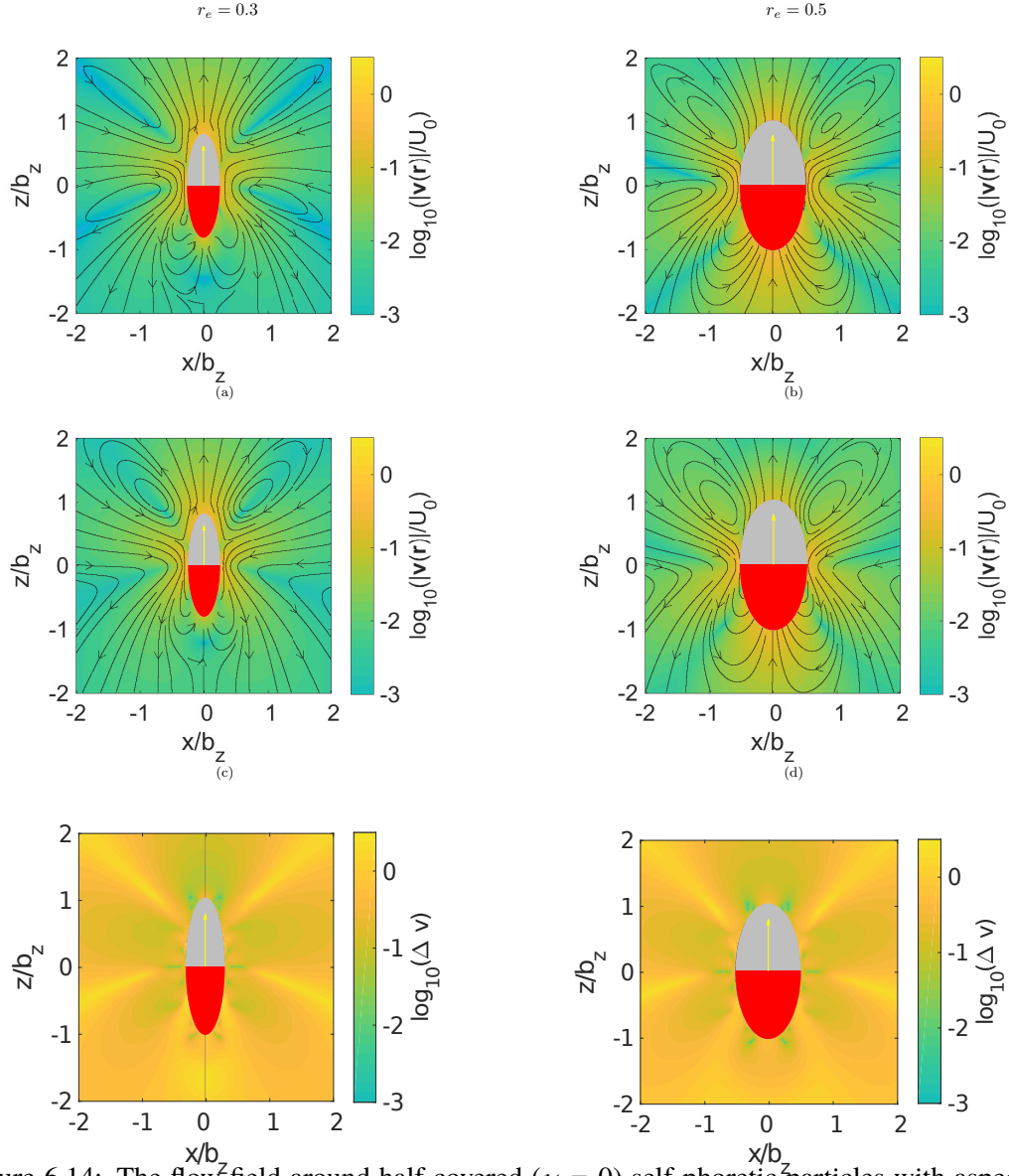


Figure 6.14: The flow field around half covered ($\chi = 0$) self-phoretic particles with aspect ratio $r_e = 0.3$ (left) and $r_e = 0.5$ (right). In both cases the analytical results are shown in the top row, the numerical results (BEM [198]) in the middle row, and the relative error between the two (Eq. (6.31)) in the bottom row. The red area depicts the chemically active region.

CHAPTER 7

SHAPE-INDUCED PAIRING OF SPHEROIDAL SQUIRMERS

7.1 Arrested-motility states in populations of shape-anisotropic active Janus particles [107]

Together with our experimental collaborators from the Argonne National Laboratory, we published “Arrested-motility states in populations of shape-anisotropic active Janus particles” in the peer-reviewed journal *Science Advances* in 2022. In their laboratory they are able to produce discoidal microswimmers and measure them under a variety of flow and field conditions. In particular, their metallo-dielectric Janus particles consist of a thin coating of metal deposited onto a dielectric core. When energized by an AC electric field, they can self-propel through liquid via an electrokinetic mechanism called induced charge electrophoresis (ICEP). A particularly interesting behavior they observed, was the formation of stable, stationary pairs above a planar wall (see Fig. 7.1).

After being approached to provide theoretical insight into the system, we analyzed the

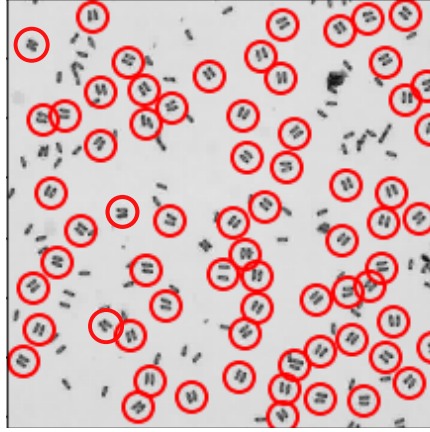


Figure 7.1: Microscopy image showing pair formation in systems of disk-shaped active Janus colloids. Pairs are identified by red circles. Scale bar, $40\mu\text{m}$. The figure has been reprinted from [107].

system with numerical and analytical methods. We found qualitative agreement between our calculations performed with the boundary element method and the experimental observations (see Fig. 7.2). Furthermore, the calculations predict a vortex in the fluid following the particle (see Fig. 7.3 (a)). This can be verified by adding tracer particles into the experimental system (see Fig. 7.3 (b)).

Another major result of the theoretical analysis is that the hydrodynamic interaction between two particles dominates the pair formation. This means that the particles behave as effective squirmers. This, and the strong similarity between the discoidal particles and oblate spheroids, makes this system an ideal candidate to apply the extended squirmer model presented in the

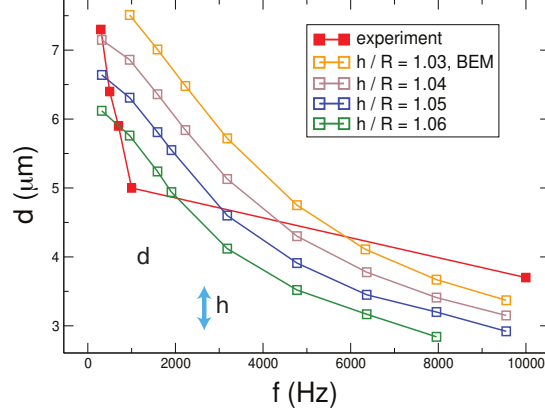


Figure 7.2: Steady separation of two particles as a function of frequency. Closed symbols show the experimental results; open symbols show the results of numerical calculations. The figure has been reprinted from [107].

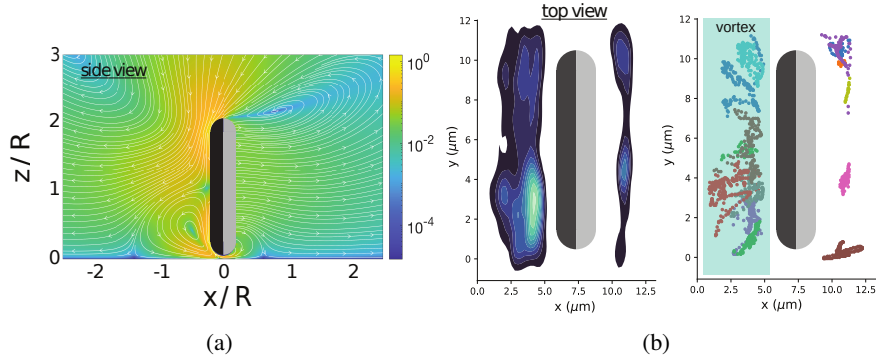


Figure 7.3: (a) Side view of the flow field in the vicinity of a Janus discoid in the DC limit ($f \rightarrow 0$). The discoid center is located at $(0, 0, 1.06R)$, and the flow field is shown in the symmetry plane $y = 0$. A solid wall is located at $z = 0$. The metal and insulating “faces” of the particle are shown in black and grey, respectively. The color field encodes the magnitude of the fluid velocity, $|\mathbf{u}(\mathbf{x})|/U_0$. A large vortex is located behind the particle and near the wall. Streamlines start and end on the front and rear of the particle, respectively, reflecting the fact the particle is moving to the right. (b) Experimental data showing the probability distribution (left) and trajectories (right) of tracer particles in the vicinity of a Janus particle. Tracers in the rear vortex move with the particle as they execute recirculating motions in the vortex. The figure has been reprinted from [107].

previous chapter. We will use the spheroidal squirmer model to perform a complete stability analysis for the pair formation discussed in [107] and predict further stable, but motile, pair configurations.

The work summarized in this chapter is currently also in preparation for submission to a peer reviewed journal.

7.2 Introduction

Self-assembly [214], clustering [38, 189] and particle motility alignment [31, 32, 89, 110, 113, 128] are among the most researched and discussed topics in the active matter community. Not only do these phenomena provide an interesting test case to show the consequences of microscopic properties, but they are also an essential step for many if not most envisioned real world applications, e.g. targeted drug delivery and lab-on-a-chip devices. Whether we want to transport a cancer drug directly to the cells to minimize side effects or turn a micromotor, a single, uncoordinated microswimmer would not be able to have a sufficient impact.

One microscopic parameter that has proven to be very important is geometry. Shape can impact the swimming speed of an active particle, the power required to achieve that speed, and the flow field sourced by the particle [48, 159, 188, 233, 258, 260]. Additionally, collisions between rod-like particles can lead to nematic ordering in an active suspension [15]. In view of the importance of particle shape, we have recently extended the popular squirmer model, first introduced by Lighthill [145] and Blake [25], to spheroidal shapes [191]. Originally, the squirming model was developed as a simple tool to describe the motion and behavior of ciliated, spherical microorganisms [49, 59, 149, 158]. However, it has since found applications well beyond its initial purpose. For instance, interfacially-driven active colloids (e.g., self-electrophoretic [247], self-diffusiophoretic [97], and self-thermophoretic [30] swimmers) can often be approximated as “effective squirmers”. Instead of modeling the wide range of different propulsion mechanisms in detail, a slip velocity on the microswimmers surface is prescribed [193]. This slip determines the two major swimming properties, speed U and stresslet S (see next section 2.8) directly [138, 227]. As an example that justifies this approach, in recent experiments, it was observed that metallo-dielectric Janus discoids, energized by AC fields, tend to form “head-to-head” bound pairs [107]. Our numerical modeling of the detailed propulsion mechanism (induced charge electrophoresis [122, 226]) revealed that hydrodynamic interactions dominated interactions between particles, i.e., the particles indeed behaved as effective squirmers.

For interfacially-driven microswimmers, a second means of controlling their motion is offered by breaking symmetries of the slip velocity. This symmetry breaking can imposed, as when a self-phoretic particle is designed to have non-axisymmetric surface chemistry [8, 146], or can emerge *in situ*, e.g., due to effects of confinement [122, 239] or symmetry-breaking external fields [195, 226]. So far, applications of the squirmer model have mostly been restricted to axisymmetric surface slip, although more general slip has been considered for spherical squirmers [66, 75, 169, 179].

In this work, we develop a general framework to study the consequences of particle shape and non-axisymmetry of the surface slip for interactions between interfacially-driven microswimmers. Analytical predictions in a far-field, “point-particle” model are supported by detailed

numerical calculations using the squirmer model. We show that both non-spherical shape and breaking of the axisymmetry are necessary conditions to form stable “head-to-head” particle pairs. These immotile bound states are held together purely by (far-field) hydrodynamic interactions. Our analysis thus completes the approach taken in our previous work [107]. Similarly, we find that motile “head-to-tail” bound pairs can be stable only when the particles are non-spherical (although they can be axisymmetric.) Overall, we find good agreement between our analytical predictions and the numerical calculations, suggesting that our framework offers a promising new approach for studying hydrodynamic interactions in heterogeneous active suspensions.

7.3 Minimal model

In order to gain some insight into the possibility of pair formation, we consider a minimal model in which swimmer α is modeled as a point-like particle with instantaneous swimming direction $\widehat{d}^{(\alpha)}$. In isolation, swimmer $\alpha \in \{1, 2\}$ has self-propulsion velocity $U_s^{(\alpha)} \geq 0$. However, each swimmer disturbs the flow around it, affecting other swimmers in its vicinity. Accordingly, for the velocity of swimmer α , we write:

$$\mathbf{U}^{(\alpha)} = U_s^{(\alpha)} \widehat{d}^{(\alpha)} + \mathbf{u}(\mathbf{x}_\alpha). \quad (7.1)$$

In the second term, the swimmer is passively advected by the ambient flow, evaluated at its position \mathbf{x}_α . (The finite size of the swimmer is neglected.) For the rotation of the swimmer, we write the Jeffrey equation [211]

$$\dot{\widehat{d}}^{(\alpha)} = \left(\mathcal{I} - \widehat{d}^{(\alpha)} \widehat{d}^{(\alpha)} \right) \cdot \left(\Gamma_\alpha \mathbf{E}(\mathbf{x}_\alpha) + \mathbf{W}(\mathbf{x}_\alpha) \right) \cdot \widehat{d}^{(\alpha)}. \quad (7.2)$$

Here, Γ_α is a shape parameter that is zero for a sphere, positive for a prolate spheroid that has its major axis aligned with $\widehat{d}^{(\alpha)}$, and negative for an oblate spheroid that has its minor axis aligned with $\widehat{d}^{(\alpha)}$. The tensors $\mathbf{E}(\mathbf{x}_\alpha)$ and $\mathbf{W}(\mathbf{x}_\alpha)$ represent the fluid rate-of-strain and vorticity, respectively, evaluated at \mathbf{x}_α , where $\mathbf{E} = \frac{1}{2} (\nabla \mathbf{u} + \nabla \mathbf{u}^T)$ and $\mathbf{W} = \frac{1}{2} (\nabla \mathbf{u} - \nabla \mathbf{u}^T)$.

To model the flow disturbance, we associate an active “stresslet” with each swimmer. In general, the stresslet provides the leading-order contribution of a force- and torque-free microswimmer to the surrounding flow field. It can be obtained from the surface traction on the swimmer as follows [125]:

$$S_{ij}^{(\alpha)} = \frac{1}{2} \int_{S_\alpha} [\sigma_{ik} n_k x_j + \sigma_{jk} n_k x_i] dS - \frac{1}{3} \int_{S_\alpha} \sigma_{lk} n_k x_l dS \delta_{ij}, \quad (7.3)$$

which is symmetric and traceless by construction. Here, the integral is taken over the surface S_α of particle α , \widehat{n} points from the surface of the particle into the surrounding fluid, and $\boldsymbol{\sigma} = -p\mathcal{I} + \mu(\nabla \mathbf{u} + \nabla \mathbf{u}^T)$ is the stress tensor for a Newtonian fluid. The velocity field from a

stresslet located at the origin is given by:

$$u_i = \frac{1}{8\pi\mu} \left(\frac{x_i \delta_{jk}}{r^3} - \frac{3x_i x_j x_k}{r^5} \right) S_{jk}^{(\alpha)}, \quad (7.4)$$

where μ is the solution viscosity, r is distance from origin, and x_i is a location in the solution. For a swimmer with an *axisymmetric* surface actuation, the stresslet can be written as

$$\mathbf{S}^{(\alpha)} = \sigma_0^{(\alpha)} \left(\widehat{d}^{(\alpha)} \widehat{d}^{(\alpha)} - \frac{\mathcal{I}}{3} \right), \quad (7.5)$$

where \mathcal{I} is the identity tensor [209]. The parameter $\sigma_0^{(\alpha)}$ specifies the “pusher” or “puller” character of the swimmer: for negative (resp., positive) $\sigma_0^{(\alpha)}$, the swimmer is a pusher (resp., puller).

However, not all microswimmers have axisymmetric actuation. For instance, a common model system in active matter are metallo-dielectric particles that are energized by an AC electric field and swim through a mechanism known as induced charge electrophoresis (ICEP) [226]. Even if the distribution of metal and dielectric material on the particle surface is axisymmetric, the electric field will break axisymmetry (if it is not itself aligned with the particle’s axis of symmetry.) Thus, we consider the following as a more general stresslet, written in a frame aligned with the principal axes \widehat{c} , \widehat{d} , and \widehat{e} of $\mathbf{S}^{(\alpha)}$:

$$\mathbf{S}^{(\alpha)} = S_{cc}^{(\alpha)} \widehat{c}\widehat{c} + S_{dd}^{(\alpha)} \widehat{d}\widehat{d} + S_{ee}^{(\alpha)} \widehat{e}\widehat{e}, \quad (7.6)$$

with $\text{tr}(\mathbf{S}^{(\alpha)}) = 0$. Since $\mathbf{S}^{(\alpha)}$ is symmetric, its principal axes are orthogonal, and without loss of generality, we define $\widehat{c} \times \widehat{d} = \widehat{e}$. For simplicity, we assume that the direction of propulsion of an isolated particle is \widehat{d} , i.e., aligned with a principal axis of the stresslet. Indeed, this assumption is realized and motivated by an isolated ICEP particle with spheroidal shape and axisymmetric metal coverage, swimming in unbounded solution. If the electric field is in the \widehat{z} direction and the particle axis of symmetry is given by \widehat{d} , the particle will rotate to orient its axis of symmetry \widehat{d} to be perpendicular to \widehat{z} . After re-orientation, particle will swim strictly in the \widehat{d} direction with a steady velocity, with a stresslet tensor in the form of Eq. 7.6. Additionally, we note that Eq. 7.6 reduces to Eq. 7.5 when $S_{dd}^{(\alpha)} = 2/3\sigma_0$ and $S_{cc}^{(\alpha)} = S_{ee}^{(\alpha)} = -\sigma_0/3$.

In the following, we restrict our consideration to two microswimmers moving in the $x - y$ plane, and examine the possibility of obtaining stable bound states. For two swimmers in unbounded fluid, the instantaneous configuration of the system is completely specified by three degrees of freedom: the center-to-center distance d and the angles ϕ_1 and ϕ_2 , where ϕ_α is the angle between \widehat{d}^α and a fixed axis (see Fig. 7.4). For convenience, we specify that the position of swimmer 1 is instantaneously at the origin, $\mathbf{r}_1 = (0, 0, 0)$, and that swimmer 2 has position $\mathbf{r}_2 = (x_2, y_2, 0)$. We construct \dot{x} , \dot{y} , $\dot{\phi}_1$, and $\dot{\phi}_2$ as functions of x , y , ϕ_1 , and ϕ_2 , and look for fixed point configurations at which these functions evaluate to zero. A fixed point represents a bound pair. Additionally, we perform linear stability analysis to find the

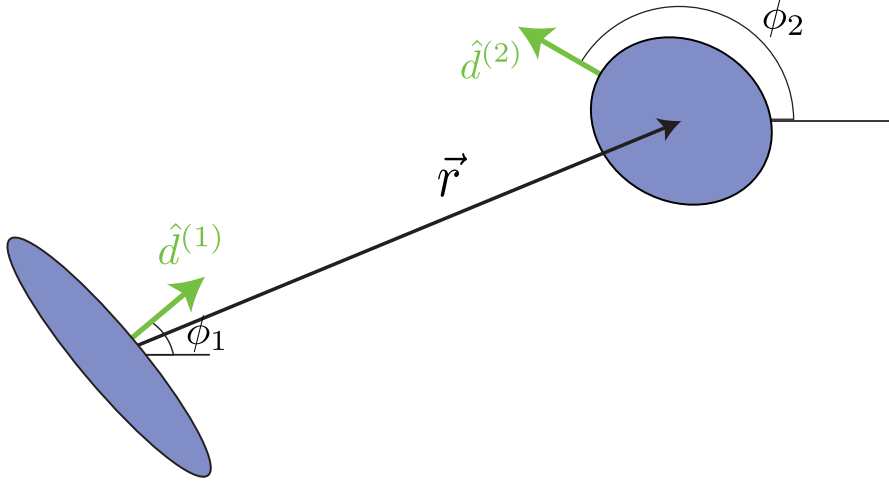


Figure 7.4: Schematic illustration of two spheroids, including their swimming directions $\hat{d}^{(1)}$ and $\hat{d}^{(2)}$, angles ϕ_1 and ϕ_2 and separation vector \mathbf{r} .

conditions under which a bound pair is stable against perturbations in any of the coordinates. For simplicity, we restrict our examination to pairs in which the particle swimming directions are aligned with the center-to-center vector.

Overall, the minimal model is analytically tractable and yields a wealth of predictions, as discussed below. However, owing to the severity of the approximations made in this model, it is desirable to compare these predictions against numerical results from a more realistic hydrodynamic model that accounts for the finite size of the particle and does not truncate the particle-generated flow field to the leading-order term.

7.4 Squirmer model

We consider N spheroidal particles in unbounded Newtonian fluid, where $N = 1$ or $N = 2$. Following Ref. 191, for particle α , we take the length of the semi-axis of symmetry to define $b_y^{(\alpha)}$, and the length of the other semi-axes to define $b_x^{(\alpha)}$. Thus, each particle has an aspect ratio $r_e^{(\alpha)}$ defined by $r_e = b_x/b_y$, with $r_e < 1$ for an prolate spheroid, $r_e = 1$ for a sphere, and $r_e > 1$ for an oblate spheroid. The quantity Γ_α is related to $r_e^{(\alpha)}$ by $\Gamma = (1 - r_e^2)/(1 + r_e^2)$. The characteristic size of the particle, $L_0^{(\alpha)}$, is chosen as $b_z^{(\alpha)}$.

The geometric centroid of particle α is located at position \mathbf{x}_α . The flow $\mathbf{u}(\mathbf{x})$ is governed by the Stokes equation, $-\nabla p + \mu \nabla^2 \mathbf{u} = 0$, where $p(\mathbf{x})$ is the pressure field, and the incompressibility condition $\nabla \cdot \mathbf{u} = 0$. On the surface of each particle α , the flow obeys the boundary condition $\mathbf{u}(\mathbf{x}) = \mathbf{U}^{(\alpha)} + \mathbf{\Omega}^{(\alpha)} \times (\mathbf{x} - \mathbf{x}_\alpha) + \mathbf{v}_s^{(\alpha)}(\mathbf{x})$. Here, $\mathbf{v}_s^{(\alpha)}(\mathbf{x})$, the so-called slip velocity, provides the surface actuation for self-propulsion, as discussed below. Additionally, the flow obeys $|\mathbf{u}| \rightarrow 0$ as $|\mathbf{x}| \rightarrow \infty$. The particles are individually force-free and torque-free, such that $\int_{S_\alpha} \boldsymbol{\sigma} \cdot \hat{\mathbf{n}} dS = 0$ and $\int_{S_\alpha} (\mathbf{x} - \mathbf{x}_\alpha) \times \boldsymbol{\sigma} \cdot \hat{\mathbf{n}} dS = 0$.

For each swimmer, the surface slip $\mathbf{v}_s^{(\alpha)}$ is fixed in a body frame attached to, and co-moving with, the swimmer. It is specified via a set of squirming mode amplitudes. In previous work (see chapter 6), we generalized the axisymmetric squirming modes to spheroidal particles. These amplitudes are denoted by B_i , with $i \geq 1$ [191]. In this chapter, in order to break axisymmetry, we develop a new squirming mode $\tilde{B}^{(\alpha)}$ inspired by the slip profile of ICEP particles. This squirming mode has a non-axisymmetric slip distribution

$$\mathbf{v}_s^{(\alpha)}(\mathbf{x}) = \tilde{B}^{(\alpha)} [\text{sign}(z)(\cos(\varphi)\hat{e}_\xi - \hat{e}_\varphi(\hat{e}_\xi \cdot \hat{e}_y)) - \text{sign}(x)(\sin(\varphi)\hat{e}_\xi - \hat{e}_\varphi(\hat{e}_\xi \cdot \hat{e}_x))] \cdot H(y) \quad (7.7)$$

and its stresslet tensor can not be simplified into the form 7.5. $H(y)$ is the Heaviside step function, \hat{e}_φ and \hat{e}_ξ are the two surface tangential basis vectors in the spheroidal coordinate system. Only \hat{e}_ξ is axisymmetric and thus, the above defined slip mode is tangential but non-axisymmetric.

We briefly discuss the case of an isolated squirmer ($N = 1$). From solution of the governing

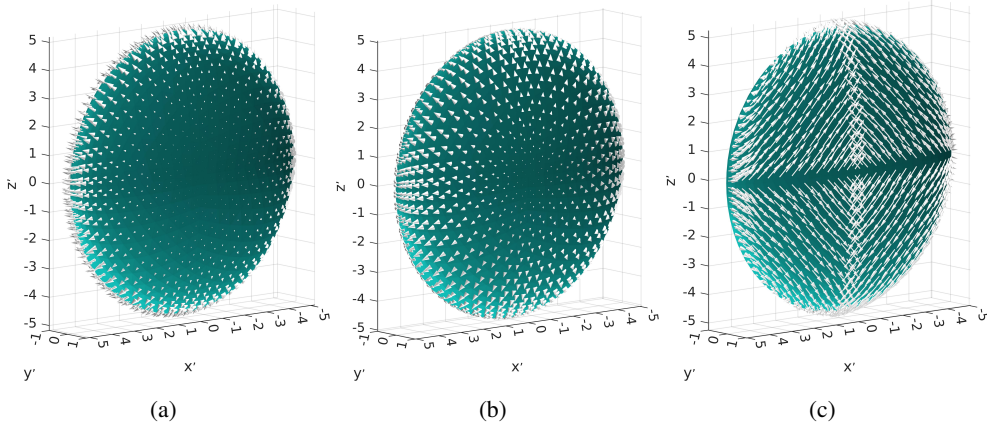


Figure 7.5: Assigned slip velocities for an oblate squirmer with aspect ratio $r_e = 5$. (a) and (b) are axisymmetric and (c) has a purely non-axisymmetric slip velocity following the definition in Eq. 7.7. (a) Shows a motile colloid with squirming mode amplitudes $B_n = \delta_{n,1}$ and $\tilde{B} = 0$. (b) and (c) are stationary particles with amplitudes (b) $B_n = \delta_{n,2}$, $\tilde{B} = 0$, and (c) $B_n = 0$, $\tilde{B} = 1$.

equations, we obtain U_s for a given geometric aspect ratio and set of squirming mode amplitudes. Additionally, the stresslet can be calculated using Eq. 7.3. Due to the linearity of the Stokes equation, the contribution of each squirming mode can be calculated individually and superposed. For the axisymmetric squirming modes, Fig. 7.8 show how the set B_i are related to $U_s^{(\alpha)}$ and $\sigma_0^{(\alpha)}$. Likewise, for the non-axisymmetric mode, we show $S_{cc}^{(\alpha)}$, $S_{dd}^{(\alpha)}$ and $S_{ee}^{(\alpha)}$ as a function of aspect ratio in Fig. 7.11. It is important to note that this squirming mode has no contribution to $S_{dd}^{(\alpha)}$ or $U_s^{(\alpha)}$, but only to the desired anti-symmetric values for $S_{cc}^{(\alpha)}$ and $S_{ee}^{(\alpha)}$.

For $N = 2$, we solve for the particle velocities numerically, using the boundary element method (BEM) [199]. We obtain complete particle trajectories by coupling the BEM to a

rigid body dynamics engine. For simplicity, we assume that $L_0^{(1)} = L_0^{(2)}$. (However, we note that the “point-particle” model has no inherent length scale. Given that $S_{ij} \sim L_0^3$ and $U_s \sim L_0^2$ for a squirmer, differences in particle size can be straightforwardly accommodated in our theoretical model.)

7.5 Head-to-head pairing

We look for solutions of the minimal model with $(x, y, \phi_1, \phi_2) = (d, 0, 0, \pi)$. We obtain

$$d = \sqrt{\frac{-3(S_{dd}^{(1)} + S_{dd}^{(2)})}{8\pi\mu(U_s^{(1)} + U_s^{(2)})}}. \quad (7.8)$$

Given that $U_s^{(\alpha)} > 0$, to obtain a finite separation $d > 0$, it is required that $(S_{dd}^{(1)} + S_{dd}^{(2)}) < 0$. In other words, the pair must have a net “pusher” character. Intuitively, for a head-to-head pair, self-propulsion would tend to bring the pair into contact; the hydrodynamic interaction must therefore “push” the particles apart. In section 7.8.1, we present a detailed linear stability analysis. In brief, translation in the center-to-center direction decouples from lateral translation and from rotations, and the bound state is stable if the following conditions are met. For stability against displacements in x , we need $(S_{dd}^{(1)} + S_{dd}^{(2)}) < 0$; from Eq. 7.8, this is already required. Concerning the coupled dynamics in y, ϕ_1 , and ϕ_2 , full results are presented in section 7.8.1. Here, for simplicity, we consider the results for identical swimmers, i.e., $U_s^{(1)} = U_s^{(2)} = U$, $\mathbf{S}^{(1)} = \mathbf{S}^{(2)} = \mathbf{S}$, and $\Gamma_1 = \Gamma_2 = \Gamma$. We obtain the requirements $\Gamma < -1/3$ and $[S_{cc}(-1 + \Gamma) + S_{dd}(1 + 2\Gamma)][S_{cc}(-1 + \Gamma) - S_{dd}(1 + 4\Gamma)] < 0$, given that $S_{dd} < 0$ (as required from above).

Notably, the requirement $\Gamma < -1/3$ corresponds to an oblate particle shape. This requirement recalls the system of discoidal ICEP particles investigated in Ref. 107. However, intriguingly, head-to-head pairing cannot be obtained for *axisymmetric* swimmers, i.e., swimmers with a stresslet given by Eq. 7.5. Setting $S_{dd} = 2\sigma_0/3$ and $S_{cc} = S_{ee} = -\sigma_0/3$, with $\sigma_0 < 0$, the second requirement reduces to $(1 + 9\Gamma) > 0$. This requirement cannot be reconciled with the requirement that $\Gamma < -1/3$. Thus, the present work clarifies and extends the (incomplete) analysis of Ref. 107, which had assumed an axisymmetric stresslet and did not carry out a full linear stability analysis. Here, we have shown that the non-axisymmetric character of the surface slip for ICEP particles is a key ingredient in the stable pairing observed in Ref. 107. To investigate further the necessary deviation from axisymmetry, we consider stresslet tensors of the form

$$\mathbf{S} = \mathbf{S}_{ax} + \sigma_0 \delta (\widehat{c\bar{c}} - \widehat{e\bar{e}}), \quad (7.9)$$

where \mathbf{S}_{ax} is equal to the right hand side of Eq. 7.5, and the perturbation δ is a dimensionless number. We note that for non-axisymmetric squirming mode $\tilde{B} \propto \delta$. We obtain the requirements $\Gamma < -1/3$ (as before) and $(-1 + 3\Gamma(-3 + \delta) - 3\delta)(1 + \Gamma + \delta(-1 + \Gamma)) < 0$. Notably, these requirements are independent of U_0 and σ_0 .

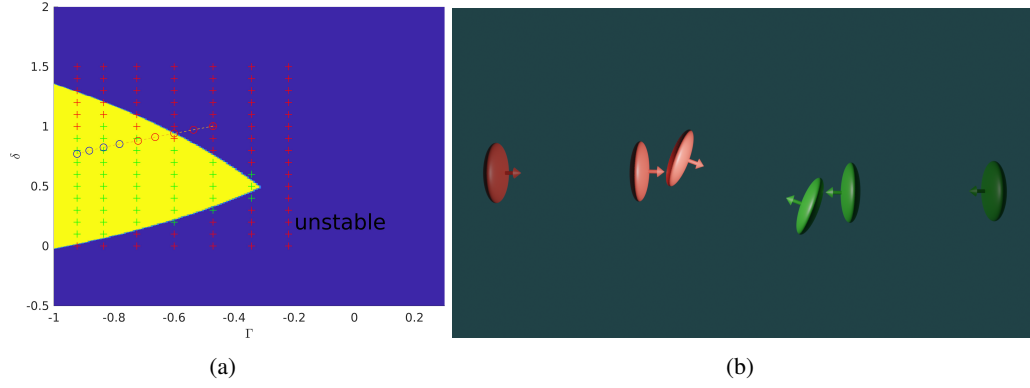


Figure 7.6: (a) Phase map for head-to-head pairs with fixed squirming modes $B_1 = 0.1$ and $B_2 = -1$ and varying δ and Γ . The background colors show the stability predicted by our model and the symbols represent numerical calculations done with BEM. The red symbols indicate particle pairs without a stable head-to-head separation. The crosses represent data including the non-axisymmetric squirming mode (Eq. 7.7), whereas the calculations using the ICEP effective squirmer model (see 7.8.7) are indicated with circles. The latter data is also connected by a dashed line as a guide to the eye. (b) Top down view of a sample trajectory for $\tilde{B} = 1.6833$ and $\Gamma = -0.8349$. The particles are initial separated by $x_{\text{initial}} = 2$ and $y_{\text{initial}} = 55$.

In Fig. 7.6 (a), the background color shows the predicted phase map in the space defined by Γ and δ . Additionally, we also show two types of numerical data. The crosses represent squirmers with the above introduced non-axisymmetric squirming mode. This mode introduces the desired perturbation δ to the stresslet tensor in a controllable manner (see Fig. 7.11). The circles show the results for an effective squirmer model for ICEP particles. The theoretical predictions and numerical results agree very well with each other, and discrepancies are mainly limited to the edge between the stable and unstable regions. The one area of significant mismatch between the theory and numerics is for Γ values close to $\Gamma = -1$, i.e. oblate spheroids with very large aspect ratios r_e . All particles are normalized by setting $b_y = 1$ and do not have a constant volume. Oblate shaped particles with a large aspect ratio are thus much larger than the other particles tested. This causes more significant error due to the point particle assumption in our theory, and explains the discrepancy for these particles. In Fig. 7.6 (b), we show how a stable pair can form between two identical swimmers. We choose particles with an aspect ratio $r_e = 3.3333$ and squirming modes $B_1 = 0.1$, $B_2 = -1$ and $\tilde{B} = 1.6833$. For these parameters we calculate S_{cc} , S_{dd} , and S_{ee} , and U_0 , and create the trajectory with a rigid body dynamics engine. The particles are initialized with opposing swimming directions $\hat{d}^{(\alpha)} \parallel \hat{e}_y$ and an offset orthogonal to it $x_{2,\text{initial}} = 2$. The particles swim towards each other without any noticeable deviation from their free space velocity. Only when the distance between them approaches the predicted separation distance d does this behavior change. Both particles slow down rapidly and their rotation becomes significant. The particles rotate towards their center-to-center line and only stop once their swimming directions are in line with it. In this configuration all twelve velocity components are zero and the particles have formed a stable, stationary pair.

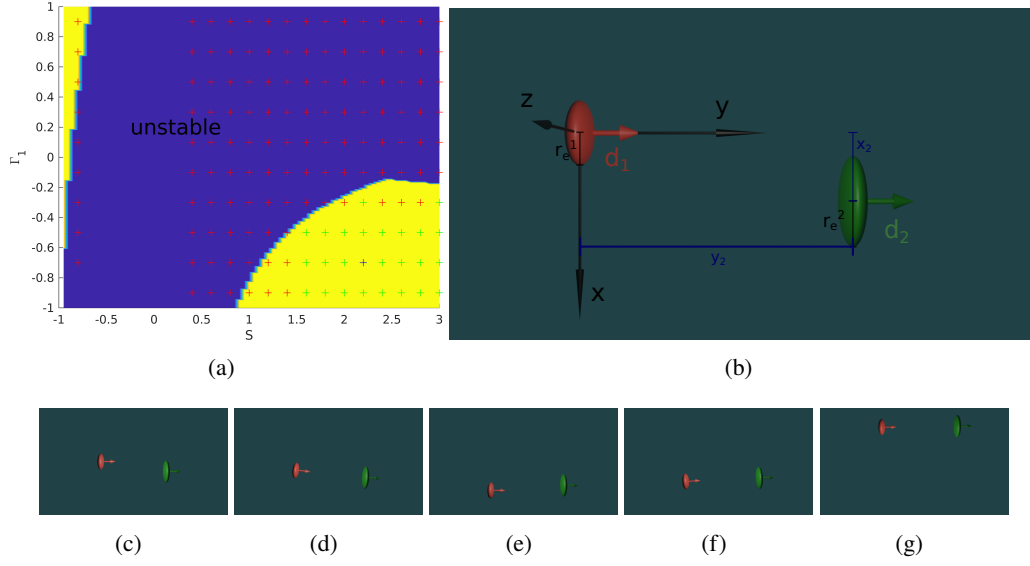


Figure 7.7: (a) Phase space for head-to-tail pairs with fixed geometric parameter $\Gamma_2 = -0.8$ and velocity ratio $U = 0.8$ and varying S and Γ_1 . The background colors show the stability predicted by our model and the symbols represent numerical calculations done with BEM. The red symbols indicate particle pairs without a stable head-to-tail separation. (b) Top-down view of a head-to-tail pair. The coordinates, separation distances x_2 and y_2 , aspect ratios $r_e^{(\alpha)}$ and swimming directions $\hat{d}^{(\alpha)}$ are also shown. (c)-(g) Top-down view of a sample trajectory for $S = 2.2$ and $\Gamma_1 = -0.7$ in five steps. This pair is represented by a blue cross in the phase space. The particles are initial separated by $x_{2,\text{initial}} = 3$ and $y_{2,\text{initial}} = 20$.

7.6 Head-to-tail pairs

Now we look for solutions of the minimal model with $(x, y, \phi_1, \phi_2) = (d, 0, 0, 0)$. We obtain

$$d = \sqrt{\frac{3(S_{dd}^{(1)} + S_{dd}^{(2)})}{8\pi\mu(U_s^{(2)} - U_s^{(1)})}}. \quad (7.10)$$

Notably, the two particles must have unequal speeds U_s to be separated by a finite distance $d > 0$. The bound pair moves with a steady speed

$$V = U_s^{(1)} + \frac{S_d^{(2)}(U_s^{(2)} - U_s^{(1)})}{S_d^{(1)} + S_d^{(2)}}. \quad (7.11)$$

Regarding stability against displacements in x , we again obtain the condition $(S_{dd}^{(1)} + S_{dd}^{(2)}) < 0$. Thus, from Eq. 7.10, we infer that the leading particle must be slower than the trailing particle, $U_s^{(1)} > U_s^{(2)}$. Concerning stability against displacements in the other coordinates, we obtain the requirements $S_{dd}^{(2)}(1 + 3\Gamma_1) + S_{dd}^{(1)}(1 + \Gamma_2) > 0$ and Eq. 7.21.

In contrast to the head-to-head case, we can obtain stable pairing for axisymmetric squirmers. However, the particles cannot be identical; they must at least have dissimilar self-propulsion speeds $U_s^{(\alpha)}$ (see Eq. 7.10). We obtain the requirements $\sigma_0^{(1)} + \sigma_0^{(2)} + 3(\sigma_0^{(2)}\Gamma_1 + \sigma_0^{(1)}\Gamma_2) > 0$

and Eq. 7.25. Due to their axisymmetry these stable pairs are not restricted to quasi 2D.

The phase space is four dimensional, defined by $S = \frac{\sigma_0^{(2)}}{\sigma_0^{(1)}}$, $V = \frac{U_s^{(2)}}{U_s^{(1)}}$, Γ_1 , and Γ_2 . For the section of the phase space in Fig. 7.7 (a), we fix the velocity ratio $V = 0.8$ and geometry of the leading particle $\Gamma_2 = -0.8$, but vary Γ_1 and the stresslet ration S . For both particles, only the first and second squirmering mode are non-zero, and determine $U_s^{(\alpha)}$ and $\sigma_0^{(\alpha)}$ respectively. Our theoretical model again agrees very well with the numerical calculation for axisymmetric spheroidal squirmers. There are two areas of significant disagreement. Similar to the head-to-head pairs one is for very oblate particles with a very large aspect ratio and thus volume. And the other one is the slim area bordering $S = -1$. At $S = -1$ the pair loses its net pusher characteristic, and as the stresslet ratio approaches this value the predicted distance d decreases to zero. This is in contrast to the far field assumption, used in our model, explaining the discrepancy between theory and numerical calculations.

For the sample trajectory in Fig. 7.7 (c-g) we choose $S = 2.2$ and $\Gamma_1 = -0.7$ and the initial separation $x_{2,\text{initial}} = 3$ and $y_{2,\text{initial}} = 20$. Both particles immediately start to rotate towards their center-to-center axis. The trailing particle, which is closer to the leading particle than Eq. (7.10) predicts, does so much faster. The center-to-center axis and the two swimming directions do not converge monotonically. Instead the trailing particle overcorrects and the rotations changes sign. In contrast, the center-to-center distance does slowly approach the predicted value. As the relative translational velocity decreases, so does the magnitude of the overcorrection. After several of these decaying oscillations all velocity components align and the pair forms a stable, co-moving pair. In this configuration the separation distance agrees with our prediction Eq. 7.10.

7.7 Conclusions

We have shown that non-spherical active particles can form bound pairs through hydrodynamic interactions alone. Our minimal model revealed that shape plays a critical role in this pairing by inducing a coupling between particle orientation and the rate-of-strain component of the particle-generated flows.

A surprising finding of our work is that squirmers with non-axisymmetric surface slip may be capable of pairing behaviors that are *not* obtainable for squirmers with axisymmetric slip. These predictions could be tested using spheroidal particles that move by induced charge electrophoresis (ICEP). In recent work, we have shown that the effective squirmer model can be an excellent approximation for the interaction of these particles, including in the presence of bounding surfaces [107]. When we considered ICEP "effective squirmers, we restricted our consideration to the DC limit, but the frequency of the driving AC field will also quantitatively impact the active stresslet and self-propulsion velocity, which can be addressed in future work.

We restricted our consideration to microswimmers moving in the plane containing their

center-to-center vector (denoted the xy plane). We note that for non-axisymmetric particles defined by Eq. 7.9, a 90° rotation of both particles around their \hat{d} axes will invert the sign of δ . Therefore, when head-to-head bound states, aligned with the y -direction, are stable against perturbations in the xy plane, they will be unstable against perturbations in the yz plane. However, the quasi-two-dimensional assumption (motion restricted to the xy plane) is realized in most active matter experiments, including on ICEP particles. Concerning head-to-tail pairing of axisymmetric particles, the bound states that are stable in the xy plane are, in fact, stable against general three-dimensional motions, owing to rotational symmetry. Our findings concerning head-to-tail pairing also suggest the possibility of engineering moving “trains” of many bound particles. However, for this application, the condition that the leading particle must be slower than the trailing particle is too restrictive. In future work, one could investigate how near-field hydrodynamics interactions (i.e., interactions that decay with distance more quickly than the stresslet), not considered in our minimal model, could replace this condition by acting to slow down the leading particle in a bound pair. Finally, we restricted our attention to bound states in which the particles’ orientations are aligned with the center-to-center vector. This could be relaxed, potentially leading to bound states with circular trajectories.

7.8 Appendix

7.8.1 Minimal model: Linear stability analysis

For a pair of spheroids, the three degrees of freedom ϕ_1 , ϕ_2 , and $|\mathbf{r}|$ are schematically illustrated in Fig. 7.4. We choose to measure ϕ_1 and ϕ_2 with respect to the x -axis in the laboratory frame.

For a fixed point, the Jacobian is constructed as follows:

$$\mathbf{J} = \begin{pmatrix} \frac{\partial \dot{x}}{\partial x} & \frac{\partial \dot{x}}{\partial y} & \frac{\partial \dot{x}}{\partial \phi_1} & \frac{\partial \dot{x}}{\partial \phi_2} \\ \frac{\partial \dot{y}}{\partial x} & \frac{\partial \dot{y}}{\partial y} & \frac{\partial \dot{y}}{\partial \phi_1} & \frac{\partial \dot{y}}{\partial \phi_2} \\ \frac{\partial \dot{\phi}_1}{\partial x} & \frac{\partial \dot{\phi}_1}{\partial y} & \frac{\partial \dot{\phi}_1}{\partial \phi_1} & \frac{\partial \dot{\phi}_1}{\partial \phi_2} \\ \frac{\partial \dot{\phi}_2}{\partial x} & \frac{\partial \dot{\phi}_2}{\partial y} & \frac{\partial \dot{\phi}_2}{\partial \phi_1} & \frac{\partial \dot{\phi}_2}{\partial \phi_2} \end{pmatrix}_{x=d, y=0, \phi_1=0, \phi_2=\pi}. \quad (7.12)$$

The Jacobian can be obtained numerically, by approximating the partial derivatives using finite differences, or analytically, as shown below.

Substituting Eq. (7.4) into Eqs. (7.1) and (7.2) we gain expressions for \dot{x} , \dot{y} , $\dot{\phi}_1$ and $\dot{\phi}_2$ in terms of x , y , ϕ_1 and ϕ_2 , as well as Γ_α , $U_s^{(\alpha)}$, S_{ii} and d . d is fixed by Eqs. (7.8) and (7.10) for head-to-head and head-to-tail pairs respectively. In the following we discuss the influence the three particle parameters Γ_α , $U_s^{(\alpha)}$ and S_{ii} have on the stability of the discovered fix points.

7.8.2 Head-to-head bound state

From the governing dynamical system, we analytically obtain the Jacobian

$$\mathbf{J} = \begin{pmatrix} \frac{3(S_{dd}^{(1)} + S_{dd}^{(2)})}{4\pi\mu d^3} & 0 & 0 & 0 \\ 0 & -\frac{3(S_{dd}^{(1)} + S_{dd}^{(2)})}{8\pi\mu d^3} & -U_s^{(1)} & -U_s^{(2)} \\ 0 & -\frac{3(S_{dd}^{(2)}(1-4\Gamma_1) + S_{cc}^{(2)}(-1+\Gamma_1))}{8\pi\mu d^4} & -\frac{9S_{dd}^{(2)}\Gamma_1}{8\pi\mu d^3} & \frac{3(S_{cc}^{(2)} - S_{dd}^{(2)})(-1+\Gamma_1)}{8\pi\mu d^3} \\ 0 & -\frac{3(S_{dd}^{(1)}(1-4\Gamma_2) + S_{cc}^{(1)}(-1+\Gamma_2))}{8\pi\mu d^4} & \frac{3(S_{cc}^{(1)} - S_{dd}^{(1)})(-1+\Gamma_2)}{8\pi\mu d^3} & -\frac{9S_{dd}^{(1)}\Gamma_2}{8\pi\mu d^3} \end{pmatrix}. \quad (7.13)$$

Noting, from the zeroes in the first row and first column, that translations in the x direction decouple from translations in y and rotations, we immediately conclude the first requirement for stability: $(S_{dd}^{(1)} + S_{dd}^{(2)}) < 0$. Next, we consider the densely populated 3×3 submatrix obtained by removing the first row and first column of \mathbf{J} . The characteristic equation of this submatrix is:

$$\lambda^3 + A\lambda^2 + B\lambda = 0, \quad (7.14)$$

with

$$A = \frac{3(S_{dd}^{(1)} + S_{dd}^{(2)}) + 9S_{dd}^{(2)}\Gamma_1 + 9S_{dd}^{(1)}\Gamma_2}{8\pi\mu d^3} \quad (7.15)$$

and

$$B = \frac{-3U_s^{(1)}(S_{dd}^{(2)}(1-4\Gamma_1) + S_{cc}^{(2)}(-1+\Gamma_1)) - 3U_s^{(2)}(S_{dd}^{(1)}(1-4\Gamma_2) + S_{cc}^{(1)}(-1+\Gamma_2))}{8\pi\mu d^4} + \frac{27(S_{dd}^{(2)}\Gamma_1 + S_{dd}^{(1)}\Gamma_2)(S_{dd}^{(1)} + S_{dd}^{(2)}) + 81S_{dd}^{(1)}S_{dd}^{(2)}\Gamma_1\Gamma_2 - 9(S_{cc}^{(1)} - S_{dd}^{(1)})(S_{cc}^{(2)} - S_{dd}^{(2)})(-1+\Gamma_1)(-1+\Gamma_2)}{64\pi^2\mu^2d^6} \quad (7.16)$$

It is immediately apparent that one of the eigenvalues is $\lambda = 0$. This is to be expected, since, for convenience, we considered more coordinates (four) than were needed to specify the state of the system (three). The $\lambda = 0$ eigenvalue therefore corresponds to a symmetry of the dynamical system. Factoring out this eigenvalue, we obtain

$$\lambda^2 + A\lambda + B = 0. \quad (7.17)$$

Although we could solve for λ , we instead apply the Routh-Hurwitz stability criterion to determine the two remaining requirements for dynamical stability. For a quadratic characteristic equation, the Routh-Hurwitz criterion specifies that a necessary and sufficient condition for stability is that all coefficients of the equation are positive. In other words, we require $A > 0$ and $B > 0$. The requirement on A gives

$$(S_{dd}^{(1)} + S_{dd}^{(2)}) + 3(S_{dd}^{(2)}\Gamma_1 + S_{dd}^{(1)}\Gamma_2) > 0. \quad (7.18)$$

For a pair of identical particles, the requirement $A > 0$ reduces to $\Gamma < -1/3$, and the requirement $B > 0$ reduces to $[S_{cc}(-1 + \Gamma) + S_{dd}(1 + 2\Gamma)][S_{cc}(-1 + \Gamma) - S_{dd}(1 + 4\Gamma)] < 0$. For a pair of identical *axisymmetric* squirmers, the requirement $B > 0$ further reduces to $(1 + \Gamma)(1 + 9\Gamma) > 0$. Given that $-1 < \Gamma < 1$ by definition, this requirement finally reduces to $\Gamma > -1/9$. Thus, for axisymmetric squirmers, we obtain incompatible requirements.

7.8.3 Head-to-tail bound state

The Jacobian matrix for the head-to-tail bound state is identical to the Jacobian for the head-to-head bound state, except that the entry in the second row, fourth column in $U_s^{(2)}$. Thus, the first requirement for stability is again $(S_{dd}^{(1)} + S_{dd}^{(2)}) < 0$. As before, the characteristic equation reduces to Eq. 7.17. Moreover, the coefficient A is again

$$A = \frac{3(S_{dd}^{(1)} + S_{dd}^{(2)}) + 9S_{dd}^{(2)}\Gamma_1 + 9S_{dd}^{(1)}\Gamma_2}{8\pi\mu d^3}, \quad (7.19)$$

giving the condition

$$(S_{dd}^{(1)} + S_{dd}^{(2)}) + 3(S_{dd}^{(2)}\Gamma_1 + S_{dd}^{(1)}\Gamma_2) > 0. \quad (7.20)$$

The coefficient B is nearly identical to Eq. 7.16, but differs in the sign of the second term in the numerator of the fraction with d^4 in the denominator:

$$B = \frac{-3U_s^{(1)}(S_{dd}^{(2)}(1 - 4\Gamma_1) + S_{cc}^{(2)}(-1 + \Gamma_1)) + 3U_s^{(2)}(S_{dd}^{(1)}(1 - 4\Gamma_2) + S_{cc}^{(1)}(-1 + \Gamma_2))}{8\pi\mu d^4} + \frac{27(S_{dd}^{(2)}\Gamma_1 + S_{dd}^{(1)}\Gamma_2)(S_{dd}^{(1)} + S_{dd}^{(2)}) + 81S_{dd}^{(1)}S_{dd}^{(2)}\Gamma_1\Gamma_2 - 9(S_{cc}^{(1)} - S_{dd}^{(1)})(S_{cc}^{(2)} - S_{dd}^{(2)})(-1 + \Gamma_1)(-1 + \Gamma_2)}{64\pi^2\mu^2 d^6} \quad (7.21)$$

Head-to-tail bound states of axisymmetric squirmers.

For non-identical *axisymmetric* squirmers, the condition $A > 0$ becomes

$$\sigma_0^{(1)} + \sigma_0^{(2)} + 3(\sigma_0^{(2)}\Gamma_1 + \sigma_0^{(1)}\Gamma_2) > 0. \quad (7.22)$$

The condition $B > 0$ becomes, using the “net pusher” criterion,

$$\begin{aligned} & \left(-2(\Gamma_2 - 1)\sigma_1^2 + (\Gamma_2 + \Gamma_1)(9\Gamma_2 + 7) - 1 \right) \sigma_0^{(2)}\sigma_0^{(1)} + 4\Gamma_1\sigma_0^{(2)2} \Big) U_s^{(2)} \\ & - \left(\Gamma_2\sigma_0^{(1)} \left((9\Gamma_1 + 7)\sigma_0^{(2)} + 4\sigma_0^{(1)} \right) + (\Gamma_1 - 1)\sigma_0^{(2)} \left(\sigma_0^{(1)} - 2\sigma_0^{(2)} \right) \right) U_s^{(1)} < 0. \end{aligned} \quad (7.23)$$

Defining the parameters $S \equiv \sigma_0^{(2)}/\sigma_0^{(1)}$ and $V \equiv U_s^{(2)}/U_s^{(1)}$, with $V \geq 0$, we obtain

$$\text{sgn}(\sigma_0^{(1)}) [1 + S + 3(S\Gamma_1 + \Gamma_2)] > 0 \quad (7.24)$$

and

$$\begin{aligned} \Gamma_2((S-2)V - 7S - 4) + \Gamma_1 S(4SV + 2S + 9\Gamma_2(V-1) + 7V - 1) \\ - S(2S + V - 1) + 2V < 0. \end{aligned} \quad (7.25)$$

In addition, the “net pusher” criterion can be expressed in term of S :

$$\text{sgn}\left(\sigma_0^{(1)}\right)(1+S) < 0. \quad (7.26)$$

These expressions make clear that the phase boundary exists in a space defined by four parameters: Γ_1 , Γ_2 , S , and V .

It is instructive to fix Γ_1 , Γ_2 , and $\text{sgn}\left(\sigma_0^{(1)}\right)$, and consider the two-dimensional phase subspace defined by V and S . First, we note that Eqs. 7.24 and 7.26 do not involve V , and place numerical bounds on S . Then, considering Eq. 7.25, we note that it can be written in the form

$$f_1(S) + f_2(S)V < 0, \quad (7.27)$$

where $f_1(S)$ and $f_2(S)$ are functions of S . Depending on the numerical bounds on S , satisfaction of the condition given in Eq. 7.27 may or may not depend on the value of V . As a concrete example, we consider $\text{sgn}\left(\sigma_0^{(1)}\right) = -1$, $\Gamma_1 = -0.7$, and $\Gamma_2 = 0.2$. From Eq. 7.26, we obtain $S > -1$. From Eq. 7.24, we obtain a stricter lower bound, $S > 1.46$. Eq. 7.25 gives $(-0.8 + 1.56S - 3.4S^2) + (1.6 - 6.96S - 2.8S^2)V < 0$. Both terms in parentheses are negative for $S > 1.46$. Therefore, the condition is satisfied for all $V > 0$, and the phase boundary reduces to a line $S = 1.46$ in (V, S) space.

7.8.4 A no-cargo theorem for head-to-tail bound states.

In the framework of the theory, it is not possible to have a stable bound state in which one of the particles is an inert cargo with no self-propulsion and no active stresslet. First, given the criterion $U_s^{(1)} > U_s^{(2)}$, it is clear that the trailing particle cannot be an inert cargo. Now we consider the possibility that particle 2 is inert, i.e., that $U_s^{(2)} = 0$, $S_{cc}^{(2)} = 0$, $S_{dd}^{(2)} = 0$, and $S_{ee}^{(2)} = 0$. Eq. 7.20 gives:

$$S_{dd}^{(1)}(1 + 3\Gamma_2) > 0. \quad (7.28)$$

Since the pair must be a net squirmer, $S_{dd}^{(1)} < 0$, so that $\Gamma_2 < -1/3$. Similarly, using $S_{dd}^{(1)} < 0$, the criterion $B > 0$ yields $\Gamma_2 > 0$. We therefore obtain a contradiction.

7.8.5 Velocity and stresslet of axisymmetric spheroidal squirmer

For axisymmetric particles we follow the spheroidal squirmers model presented in ref. 191 with slip velocities defined by

$$v_s(\zeta)\widehat{e}_\zeta = \tau_0(\tau_0^2 - \zeta^2)^{-1/2}P_n^1(\zeta)\widehat{e}_\zeta. \quad (7.29)$$

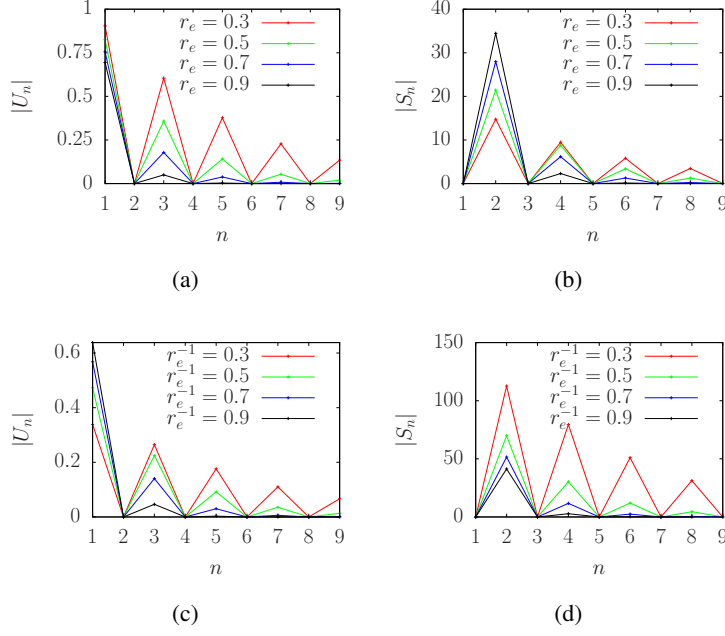


Figure 7.8: (a) The absolute value $|U|$ of the contribution of the slip modes $n = 1, 3, 5, 7$ to the velocity of a prolate squirmer for aspect ratios $r_e = 0.3, 0.5, 0.7, 0.9$. (b) The absolute value $|S|$ of the contribution of the slip modes $n = 1, 3, 5, 7$ to the stresslet of a prolate squirmer for aspect ratios $r_e = 0.3, 0.5, 0.7, 0.9$. (c) The absolute value $|U|$ of the contribution of the slip modes $n = 1, 3, 5, 7$ to the velocity of an oblate squirmer for aspect ratios $r_e^{-1} = 0.3, 0.5, 0.7, 0.9$. (d) The absolute value $|S|$ of the contribution of the slip modes $n = 1, 3, 5, 7$ to the stresslet of an oblate squirmer for aspect ratios $r_e^{-1} = 0.3, 0.5, 0.7, 0.9$. The lines represent only a guide to the eye.

ζ and τ are spheroidal coordinates. The free space velocity U_0 and stresslet $S_0 = \frac{3}{2}\sigma_0$ for each individual particle only depends on its aspect ratio r_e and squirming amplitudes B_n .

In Fig. 7.9 we compare the analytic results for the velocity $|U_n|$ and $|S_n|$ induced by B_1 and B_2 squirmer modes to numeric calculations done with BEM.

7.8.6 Separation distance

The second main prediction of our model besides the stability of the pairs is their separation distance d . d can even be calculated for two particles which are only stable against perturbations in the direction of propulsion. In Fig. 7.10 we show how our prediction compares against the distance calculated with the BEM. Similar to the stability analysis we generally get very good agreement, but have two areas of significant disagreement. Both for oblate particles, as well as for small distances d , our prediction is consistently smaller than the results of our numeric calculations.

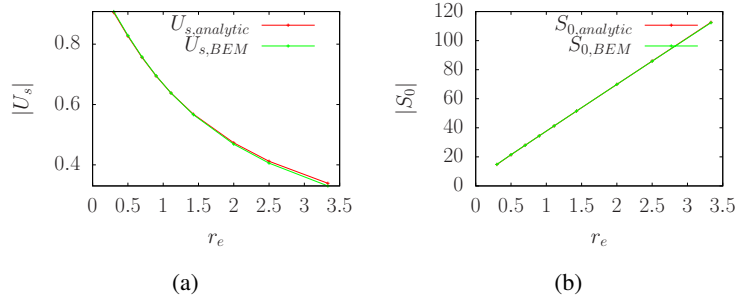


Figure 7.9: (a) Comparison between the analytically predicted and the numerically calculated velocity $|U_s|$ over a range of aspect ratios r_e . For these calculations, only B_1 is non zero. (b) Comparison between the analytic predicted and the numerically calculated stresslet magnitude $|S_0|$ over a range of aspect ratios r_e . For these calculations only B_2 is non zero.

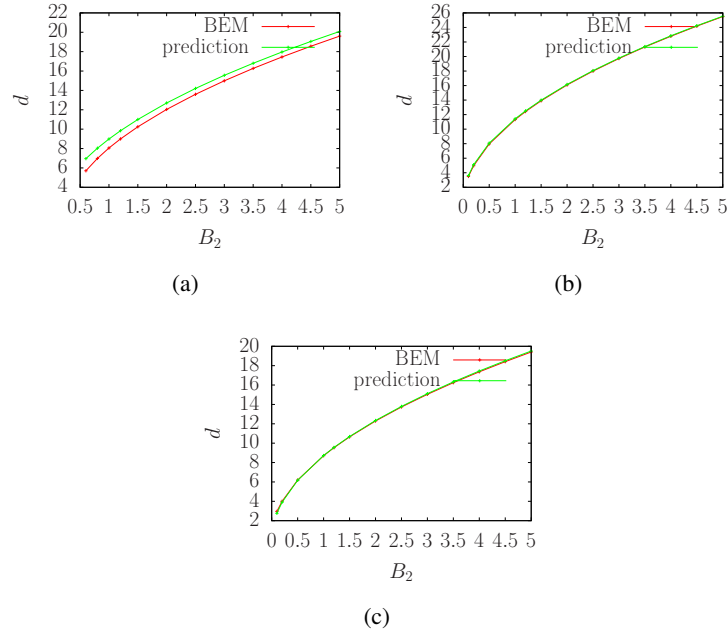


Figure 7.10: Comparison between the predicted and the calculated (BEM) separation distance for head- to-tail pairs. The velocities $U_s^{(2)} = 0.2$ and $U_s^{(1)} = 0.25$ are fixed in all cases. We show three different geometries (a) $r_e^{(1)} = 1.1055$ and $r_e^{(2)} = 3$, (b) $r_e^{(1)} = 1.1055$ and $r_e^{(2)} = 1.1055$, (c) $r_e^{(1)} = 0.5774$ and $r_e^{(2)} = 0.5774$.

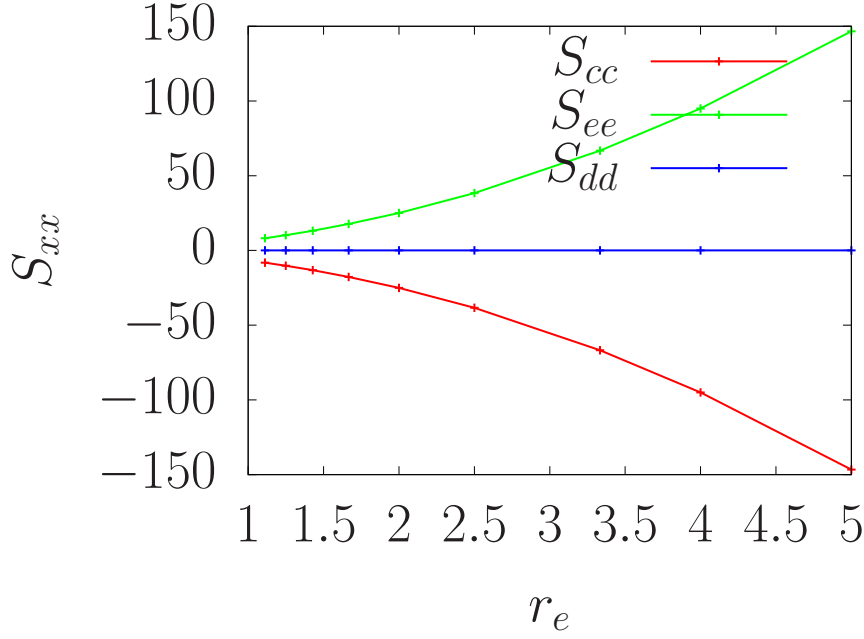


Figure 7.11: The S_{dd} , S_{cc} and S_{ee} contributions for a squirmer with constant asymmetric mode $\tilde{B} = 1$ for changing aspect ratio r_e . The lines represent only a guide to the eye.

7.8.7 Induced charge electrophoresis

Effective squirmer model for ICEP particles. In order to model the interaction of particles with non-axisymmetric actuation, we first consider a single spheroidal Janus particle moving by ICEP in unbounded solution. The particle consists of a dielectric core with half of its surface covered by metal. The metal coverage is axisymmetric, and the particle aspect ratio is defined as above. A uniform electric field $\mathbf{E} = E_0 \hat{\mathbf{z}}$ is perpendicular to the particle axis $\hat{\mathbf{d}}$: $\hat{\mathbf{z}} = \hat{\mathbf{e}}$. In the DC limit, the time-averaged electrostatic potential ϕ obeys $\nabla^2 \phi = 0$, as well as the boundary conditions $\hat{\mathbf{n}} \cdot \nabla \phi = 0$ on the surface of the particle, and $\phi \rightarrow -E_0 z$ as $|\mathbf{x}| \rightarrow \infty$. As described in the SI and Refs. 122 and 107, the surface slip can be obtained from the surface potential. Turning to the dynamics of interacting pairs, we fix $\mathbf{v}_s^{(\alpha)}$ to be the distribution for an isolated particle, i.e., we neglect electrostatic interactions between particles. Due to the constant surface slip, the particles in this model can be regarded as non-axisymmetric squirmers. The flow obeys the same equations as for the axisymmetric squirmers.

7.8.8 Non-axisymmetric squirmer model

In Fig. 7.11 we show the three diagonal components of the stresslet tensor for varying aspect ratio r_e . S_{dd} and U_s are zero for all aspect ratios, and S_{cc} and S_{ee} decrease and increase with with equation magnitude and opposite sign.

CHAPTER 8

CONCLUSION

The work presented in this thesis focuses on both convex (spheroidal) and concave (helical and toroidal) variations to the common spherical shape of active microswimmers. The concave surfaces are especially noteworthy for chemically active microswimmers. They facilitate the accumulation of the product molecules in specific, controllable areas beyond what is possible for convex geometries. Thus, the helix and torus shapes were investigated in particular for self-diffusiophoretic particles.

The helical geometry breaks the symmetry of the particle so completely, that both motion in all three translational directions, as well as rotations around all three axes, are accessible with simple catalytic coatings. Numeric calculations with the boundary element method (BEM) and the extended slender body theory developed for the concentration field agree very well and show the importance of circumferential variations in the concentration field. The variations are quasi-sinusoidal and both the amplitude and phase change depending on the geometric and chemical parameters. Moreover, circumferential variations in concentration do not require a circumferential variation in activity profile. The circumferential changes in the concentration field produce circumferential slips, which are a main factor in allowing for the additional degrees of freedom in the particle motion. The other important factor are contributions from the two ends. While they are dominated by the tangential and circumferential slip contributions for long helices, they are especially important for ones with a small length or pitch. Remarkably, even when the two ends point in opposite direction, motion perpendicular to the center axis is still possible. Not all sections of the helix with opposite normal vectors are an equal distance from the center, causing the spatially decaying concentration field to break the symmetry and causing net perpendicular motion.

Their wide range of motions makes helical self-diffusiophoretic microswimmers a prime option for many real world applications. However, beforehand several questions need to be answered. Among them are: How do they behave close to a wall, and are there stable configurations similar to those for spheres (i.e. sliding or hovering states)? How are they reacting to an external gradient or flow? And how do they interact if multiple helices are close to each other?

The second shapes of interest are spheroids. Despite being more similar to the basic sphere, and even when limited to axisymmetric, tangential slip velocities, the spheroid shape also allows for additional freedom. In this cases, the propulsion in free space is again limited to a one dimensional translation (assuming axisymmetric actuation), but how this motion is achieved is much more flexible. For spheroidal particles, an extension to the traditional squirmer model was presented. This model does not need to assume a specific propulsion mechanism and instead uses the more general slip velocity as its starting point. It can thus be applied to both biological and artificial microswimmers, i.e. ciliated microorganisms and self-diffusiophoretic Janus particles. The resulting fully analytic solution to the hydrodynamic

stokes problem shows that many swimming modes propel the particle, instead of only the first in the spherical case. A similar switch affects the stresslet. Instead of only the second mode contributing, all even modes do so. The analytic model again agree with the numerical calculations with BEM very well. These results give rise to several questions: Do bacteria and other motile microorganisms, many of whom have elongated, prolate shaped bodies, use this to their advantage? By not being limited to one swimming mode, they can change the flow field in their immediate and distant surroundings easier and without also changing their swimming speed. This could allow them to adapt their nutrient uptake or perform hydrodynamic camouflage more easily, granting an evolutionary advantage. Similarly, this flexibility might be a key part in designing artificial microswimmers optimized for specific tasks.

During the second half of my PhD studies, I focused on the intriguing questions: How does the shape of particles influence their interactions? And can changing the geometry of the particles facilitate the self-organizing into complex structures without the need for an external field or relying on steric exclusion? In chapters 5 and 7 the existence of co-moving pairs of self-diffusiophoretic toruses and spheres, and spheroidal squirmers is predicted respectively. In both cases the shape of the particles plays an essential role.

In the purely hydrodynamic model (Chapter 7) for spheroidal microswimmers, the geometry is essential in determining whether the fixed points are stable or not. This holds true both for the co-moving head-to-tail pairs, as well as the stationary head-to-head pairs. For the latter configuration it was also shown that a breaking of the axisymmetry is essential. Additionally, the model also predicts that spheres can not form such stable pairs. This explains, at least in part, why a new class of clusters has only recently been described [107].

For the self-diffusiophoretic sphere and torus pair (6) an interesting additional case exists. The sphere can move through the torus and escape on the other side without ever forming a pair. This opens the possibility to design "lock-and-key" interactions. One possible application for those could be velocity gates separating slow moving from fast moving active spheres.

For both systems the natural next step will be to add additional particles and test if they form long, stable chains of particles. These would be of both intellectual interest and incredible usefulness. Such a train of particles would ease the collective navigation for large groups of microswimmers, and also has been shown to increase the transport capabilities by an order of magnitude[110]. In this context, many more questions would be relevant: How stable is the combined swimming direction compared to that of a single particle? Can the combined swimming speed be controlled and, if yes, how? Is a controlled break up at the target location possible? How densely can the particles be packed in such structures? Are there other geometries with similar behavior?

In this thesis, the importance of shape for a wide range of microswimmers is discussed and shown. Geometries beyond the basic sphere enable many more possibilities for the design of active colloids and are a prime candidate for many applications. These possibilities naturally come with many open questions still to be answered. In particular, the topic of interacting

active colloids will remain a top priority within the active matter community.

BIBLIOGRAPHY

- [1] Cambridge university press & assessment, rights & permissions, faq. <https://www.cambridge.org/about-us/rights-permissions/faqs/>. Accessed: 2023-03-08.
- [2] National committee for fluid mechanics films. <http://web.mit.edu/hml/ncfmf.html>. Accessed: 2023-03-09.
- [3] This robot can walk and swim - inside you. <https://www.nytimes.com/video/science/1000000005660722/this-robot-can-walk-and-swim-inside-you.html>. Accessed: 2023-03-12.
- [4] M. Abramowitz and I. A. Stegun. *Handbook of mathematical functions: with formulas, graphs, and mathematical tables*. Dover, 1970.
- [5] R. Aditi Simha and S. Ramaswamy. Hydrodynamic fluctuations and instabilities in ordered suspensions of self-propelled particles. *Physical Review Letters*, 89:058101, 2002.
- [6] J. L. Anderson. Colloid transport by interfacial forces. *Ann. Rev. Fluid Mech.*, 21:61–99, 1989.
- [7] J.L. Anderson. Colloid transport by interfacial forces. *Annual Review of Fluid Mechanics*, 21(1):61–99, 1989.
- [8] RJ Archer, AI Campbell, and SJ Ebbens. Glancing angle metal evaporation synthesis of catalytic swimming janus colloids with well defined angular velocity. *Soft Matter*, 11(34):6872–6880, 2015.
- [9] J. Arlt, V. A. Martinez, A. Dawson, T. Pilizota, and W. C. K. Poon. Painting with light-powered bacteria. *Nature Communications*, 9:768, 2018.
- [10] Pragya Arora, A. K. Sood, and Rajesh Ganapathy. Emergent stereoselective interactions and self-recognition in polar chiral active ellipsoids. *Science Advances*, 7(9):eabd0331, 2021.
- [11] A. Aubret, M. Youssef, S. Sacanna, and J. Palacci. Targeted assembly and synchronization of self-spinning microgears. *Nature Phys.*, 14:1114–1118, 2018.
- [12] Antoine Aubret, Mena Youssef, Stefano Sacanna, and Jérémie Palacci. Targeted assembly and synchronization of self-spinning microgears. *Nature Physics*, 14(11):1114–1118, 2018.
- [13] R. D. Baker, T. Montenegro-Johnson, A. D. Sediako, M. J. Thomson, A. Sen, E. Lauga, and I. S. Aranson. Shape-programmed 3d printed swimming microtori for the transport of passive and active agents. *Nat. Comm.*, 10:4932, 2019.

- [14] M. Ballerini, N. Cabibbo, R. Candelier, A. Cavagna, E. Cisbani, I. Giardina, V. Lecomte, A. Orlandi, G. Parisi, A. Procaccini, M. Viale, and V. Zdravkovic. Interaction ruling animal collective behavior depends on topological rather than metric distance: Evidence from a field study. *Proceedings of the National Academy of Sciences*, 105(4):1232–1237, January 2008. Publisher: National Academy of Sciences Section: Biological Sciences.
- [15] Markus Bär, Robert Großmann, Sebastian Heidenreich, and Fernando Peruani. Self-propelled rods: Insights and perspectives for active matter. *Annual Review of Condensed Matter Physics*, 11:441–466, 2020.
- [16] L. Baraban, M. Tasinkevych, M. N. Popescu, S. Sánchez, S. Dietrich, and O. G. Schmidt. Transport of cargo by catalytic janus micro-motors. *Soft Matter*, 8:48, 2012.
- [17] M. Z. Bazant. Induced-charge electrokinetic phenomena: Theory and microfluidic applications. *Phys. Rev. Lett.*, 92:066101, 2004.
- [18] C. Bechinger, R. Di Leonardo, H. Löwen, C. Reichhardt, G. Volpe, and G. Volpe. Active particles in complex and crowded environments. *Reviews of Modern Physics*, 88:045006, 2016.
- [19] C. Bechinger, R. Di Leonardo, H. Löwen, C. Reichhardt, G. Volpe, and G. Volpe. Active particles in complex and crowded environments. *Reviews of Modern Physics*, 88(4):045006, November 2016. Publisher: American Physical Society.
- [20] S. Beladi-Mousavi, S. Hermanova, Y. Ying, J. Plutnar, and M. Pumera. A maze in plastic wastes: autonomous motile photocatalytic microrobots against microplastics. *ACS Applied Materials & Interfaces*, 13(21):25102–25110, 2021.
- [21] A.P. Berke, L. Turner, H.C. Berg, and E. Lauga. Hydrodynamic attraction of swimming microorganisms by surfaces. *Phys. Rev. Lett.*, 101:038102, 2008.
- [22] S. Bianchi, F. Saglimbeni, and R. Di Leonardo. Holographic imaging reveals the mechanism of wall entrapment in swimming bacteria. *Physical Review X*, 7:011010, 2017.
- [23] S. Bianchi, V. C. Sosa, G. Vizsnyiczai, and R. Di Leonardo. Brownian fluctuations and hydrodynamics of a microhelix near a solid wall. *Sci. Rep.*, 10:4609, 2020.
- [24] J. R. Blake. *J. Fluid Mech.*, 46:199–208, 1971.
- [25] J.R. Blake. A spherical envelope approach to ciliary propulsion. *Journal of Fluid Mechanics*, 46(1):199–208, 1971.
- [26] A. Boymelgreen, T. Balli, T. Miloh, and G. Yossifon. Active colloids as mobile microelectrodes for unified label-free selective cargo transport. *Nature communications*, 9(1):1–8, 2018.

- [27] A. Boymelgreen, G. Yossifon, and T. Miloh. Propulsion of Active Colloids by Self-Induced Field Gradients. *Langmuir*, 32(37):9540–9547, September 2016. Publisher: American Chemical Society.
- [28] A. Boymelgreen, G. Yossifon, and T. Miloh. Propulsion of active colloids by self-induced field gradients. *Langmuir*, 32(37):9540–9547, 2016.
- [29] Alicia M Boymelgreen, Tov Balli, Touvia Miloh, and Gilad Yossifon. Active colloids as mobile microelectrodes for unified label-free selective cargo transport. *Nature communications*, 9(1):760, 2018.
- [30] Andreas P Bregulla and Frank Cichos. Flow fields around pinned self-thermophoretic microswimmers under confinement. *The Journal of chemical physics*, 151(4):044706, 2019.
- [31] A. Bricard, J. Caussin, D. Das, C. Savoie, V. Chikkadi, K. Shitara, O. Chepizhko, F. Peruani, D. Saintillan, and D. Bartolo. Emergent vortices in populations of colloidal rollers. *Nature Communications*, 6(1):7470, June 2015. Number: 1 Publisher: Nature Publishing Group.
- [32] A. Bricard, J. Caussin, N. Desreumaux, O. Dauchot, and D. Bartolo. Emergence of macroscopic directed motion in populations of motile colloids. *Nature*, 503(7474):95–98, November 2013.
- [33] A. Bricard, J.B. Caussin, N. Desreumaux, O. Dauchot, and D. Bartolo. Emergence of macroscopic directed motion in populations of motile colloids. *Nature*, 503:95–98, 2013.
- [34] A. Brooks, S. Sabrina, and K. Bishop. Shape-directed dynamics of active colloids powered by induced-charge electrophoresis. *Proceedings of the national academy of sciences*, 115(6):E1090–E1099, 2018.
- [35] A. M. Brooks, S. Sabrina, and K. J. M. Bishop. Shape-directed dynamics of active colloids powered by induced-charge electrophoresis. *Proc. Nat. Acad. Sci.*, 115:E1090–E1099, 2018.
- [36] S. Brown and R. Johnstone. Cooperation in the dark: signalling and collective action in quorum-sensing bacteria. *Proceedings of the Royal Society of London. Series B: Biological Sciences*, 268(1470):961–965, May 2001. Publisher: Royal Society.
- [37] B. Burke and C.L. Stewart. Life at the edge: the nuclear envelope and human disease. *Nature Reviews Molecular Cell Biology*, 3(8):575, 2002.
- [38] I. Buttinoni, J. Bialké, F. Kümmel, H. Löwen, C. Bechinger, and T. Speck. Dynamical clustering and phase separation in suspensions of self-propelled colloidal particles. *Physical review letters*, 110(23):238301, 2013.

- [39] Ivo Buttinoni, Julian Bialké, Felix Kümmel, Hartmut Löwen, Clemens Bechinger, and Thomas Speck. Dynamical clustering and phase separation in suspensions of self-propelled colloidal particles. *Phys. Rev. Lett.*, 110:238301, 2013.
- [40] T. Bäuerle, A. Fischer, T. Speck, and C. Bechinger. Self-organization of active particles by quorum sensing rules. *Nature Communications*, 9(1):3232, August 2018. Number: 1 Publisher: Nature Publishing Group.
- [41] A. Campbell and S. Ebbens. Gravitaxis in spherical janus swimming devices. *Langmuir*, 29(46):14066–14073, 2013.
- [42] A. Campbell and S. Ebbens. Gravitaxis in spherical janus swimming devices. *Langmuir*, 29(46):14066–14073, 2013.
- [43] A. I. Campbell and S. J. Ebbens. Gravitaxis in spherical janus swimming devices. *Langmuir*, 29:14066–14073, 2013.
- [44] J. Castro and Y. Feisel. Eruption of ultralow-viscosity basanite magma at cumbre vieja, la palma, canary islands. *Nature communications*, 13(1):3174, 2022.
- [45] Michael E Cates and Julien Tailleur. Motility-induced phase separation. *Annu. Rev. Condens. Matter Phys.*, 6(1):219–244, 2015.
- [46] S. Chattopadhyay, R. Moldovan, C. Yeung, and X. L. Wu. Swimming efficiency of bacterium *Escherichia coli*. *Proc. Natl. Acad. Sci.*, 103:13712–13717, 2006.
- [47] R. Cortez, L. Fauci, and A. Medovikov. The method of regularized stokeslets in three dimensions: Analysis, validation, and application to helical swimming. *Phys. Fluids*, 17:031504, 2005.
- [48] Abdallah Daddi-Moussa-Ider, Babak Nasouri, Andrej Vilfan, and Ramin Golestanian. Optimal swimmers can be pullers, pushers or neutral depending on the shape. *Journal of Fluid Mechanics*, 922:R5, 2021.
- [49] C. Darveniza, T. Ishikawa, T. J. Pedley, and D. R. Brumley. Pairwise scattering and bound states of spherical microorganisms. *Phys. Rev. Fluids*, 7:013104, Jan 2022.
- [50] G. Dassios, M. Hadjinicolaou, and A.C. Payatakes. Generalized eigenfunctions and complete semiseparable solutions for stokes flow in spheroidal coordinates. *Quarterly of Applied Mathematics*, 52(1):157–191, 1994.
- [51] B.V. Derjaguin, Yu.I. Yalamov, and A.I. Storozhilova. Diffusiophoresis of large aerosol particles. *Journal of Colloid and Interface Science*, 22:117 – 125, 1966.
- [52] Nidhi M Diwakar, Golak Kunti, Touvia Miloh, Gilad Yossifon, and Orlin D Velev. Ac electrohydrodynamic propulsion and rotation of active particles of engineered shape and asymmetry. *Current Opinion in Colloid & Interface Science*, page 101586, 2022.

- [53] Viet Sang Doan, Dong-Ook Kim, Craig Snoeyink, Ying Sun, and Sangwoo Shin. Shape-and orientation-dependent diffusiophoresis of colloidal ellipsoids. *arXiv preprint arXiv:2302.11749*, 2023.
- [54] C. Dombrowski, L. Cisneros, S. Chatkaew, R. E. Goldstein, and J. O. Kessler. Self-concentration and large-scale coherence in bacterial dynamics. *Physical Review Letters*, 93:098103, 2004.
- [55] A. Doostmohammadi, J. Ignés-Mullol, J. M. Yeomans, and F. Sagués. Active nematics. *Nature Communications*, 9:3246, 2018.
- [56] M. T. Downton and H. Stark. Simulation of a model microswimmer. *Journal of Physics: Condensed Matter*, 21(20):204101, 2009.
- [57] K. Drescher, R. E. Goldstein, N. Michel, M. Polin, and I. Tuval. Direct measurement of the flow field around swimming microorganisms. *Physical Review Letters*, 105(16):168101, 2010.
- [58] K. Drescher, K. C. Leptos, I. Tuval, T. Ishikawa, T. J. Pedley, and R. E. Goldstein. Dancing volvox: hydrodynamic bound states of swimming algae. *Physical Review Letters*, 102(16):168101, 2009.
- [59] Knut Drescher, Kyriacos C. Leptos, Idan Tuval, Takuji Ishikawa, Timothy J. Pedley, and Raymond E. Goldstein. Dancing volvox: Hydrodynamic bound states of swimming algae. *Phys. Rev. Lett.*, 102:168101, 2009.
- [60] O. du Roure, A. Lindner, E. N. Nazockdast, and M. J. Shelley. Dynamics of flexible fibers in viscous flows and fluids. *Ann. Rev. Fluid Mech.*, 51:539–572, 2019.
- [61] P. Eastham and K. Shoele. Axisymmetric squirmers in stokes fluid with nonuniform viscosity. *Phys. Rev. Fluids*, 5:063102, 2020.
- [62] S. J. Ebbens and J. R. Howse. In pursuit of propulsion at the nanoscale. *Soft Matter*, 6(4):726–738, 2010.
- [63] S.J. Ebbens and J.R. Howse. In pursuit of propulsion at the nanoscale. *Soft Matter*, 6:726–738, 2010.
- [64] J. Elgeti, R.G. Winkler, and G. Gompper. Physics of microswimmers – single particle motion and collective behavior: a review. *Reports on Progress in Physics*, 78:056601, 2015.
- [65] B.U. Felderhof. Stokesian swimming of a prolate spheroid at low reynolds number. *European Journal of Mechanics-B/Fluids*, 60:230–236, 2016.
- [66] BU Felderhof and RB Jones. Stokesian swimming of a sphere at low reynolds number by helical surface distortion. *Physics of Fluids*, 28(7):073601, 2016.

- [67] N. Figueroa-Morales, G.L. Mino, A. Rivera, R. Caballero, E. Clement, E. Altshuler, and A. Lindner. Living on the edge: transfer and traffic of e. coli in a confined flow. *Soft Matter*, 11:6284–6293, 2015.
- [68] Y. Fily, S. Henkes, and C. Marchetti. Freezing and phase separation of self-propelled disks. *Soft matter*, 10(13):2132–2140, 2014.
- [69] Y. Fily and C. Marchetti. Athermal phase separation of self-propelled particles with no alignment. *Physical review letters*, 108(23):235702, 2012.
- [70] G. T. Fortune, A. Worley, A. B. Sendova-Franks, N. Franks, K. C. Leptos, E. Lauga, and R. E. Goldstein. The fluid dynamics of collective vortex structures of plant-animal worms. *J. Fluid Mech.*, 914:A20, 2021.
- [71] G. Frangipane, D. Dell’Arciprete, S. Petracchini, C. Maggi, F. Saglimbeni, S. Bianchi, G. Vizsnyiczai, M.L. Bernardini, and R. Di Leonardo. Dynamic density shaping of photokinetic e. coli. *eLife*, 7:e36608, 2018.
- [72] Arkava Ganguly and Ankur Gupta. Going in circles: Slender body analysis of a self-propelling bent rod. *Physical Review Fluids*, 8(1):014103, 2023.
- [73] S. Gangwal, O. Cayre, M. Bazant, and O. Velev. Induced-Charge Electrophoresis of Metallodielectric Particles. *Physical Review Letters*, 100(5):058302, February 2008. Publisher: American Physical Society.
- [74] W. Gao and J. Wang. The environmental impact of micro/nanomachines: a review. *American Chemical Society Nano*, 8(4):3170–3180, 2014.
- [75] Somdeb Ghose and R. Adhikari. Irreducible representations of oscillatory and swirling flows in active soft matter. *Phys. Rev. Lett.*, 112:118102, 2014.
- [76] A. Ghosh and P. Fischer. Controlled propulsion of artificial magnetic nanostructured propellers. *Nano Lett.*, 9:2243–2245, 2009.
- [77] J. G. Gibbs. Shape- and material-dependent self-propulsion of photocatalytic active colloids, interfacial effects, and dynamic interparticle interactions. *Langmuir*, 36:6938–6947, 2020.
- [78] J. G. Gibbs and P. Fischer. Active colloidal microdrills. *ChemComm*, 51:4192, 2015.
- [79] W. Gilpin, V.N. Prakash, and M. Prakash. Vortex arrays and ciliary tangles underlie the feeding–swimming trade-off in starfish larvae. *Nature Physics*, 13(4):380, 2017.
- [80] R. Golestanian, T. B. Liverpool, and A. Ajdari. Propulsion of a molecular machine by asymmetric distribution of reaction products. *Physical Review Letters*, 94:220801, 2005.

- [81] R. Golestanian, T.B. Liverpool, and A. Ajdari. Designing phoretic micro-and nano-swimmers. *New Journal of Physics*, 9(5):126, 2007.
- [82] G. Gonnella, D. Marenduzzo, A. Suma, and A. Tiribocchi. Motility-induced phase separation and coarsening in active matter. *Comptes Rendus Physique*, 16(3):316–331, 2015.
- [83] I.O. Götze and G. Gompper. Mesoscale simulations of hydrodynamic squirmer interactions. *Physical Review E*, 82(4):041921, 2010.
- [84] I.S. Gradshteyn and I.M. Ryzhik. *Table of integrals, series, and products*. Academic Press, 2014.
- [85] J. Gray and G. J. Handcock. The propulsion of sea-urchin spermatozoa. *J. Exp. Biol.*, 32:802–814, 1955.
- [86] J.S. Guasto, R. Rusconi, and R. Stocker. Fluid mechanics of planktonic microorganisms. *Annual Review of Fluid Mechanics*, 44:373–400, 2012.
- [87] B. Ten Hagen, F. Kümmel, R. Wittkowski, D. Takagi, H. Löwen, and C. Bechinger. Gravitaxis of asymmetric self-propelled colloidal particles. *Nature communications*, 5(1):4829, 2014.
- [88] K. Han, G. Kokot, S. Das, R. Winkler, F. Gompper, and A. Snezhko. Reconfigurable structure and tunable transport in synchronized active spinner materials. *Science Advances*, 6(12):eaaz8535, March 2020. Publisher: American Association for the Advancement of Science Section: Research Article.
- [89] K. Han, G. Kokot, O. Tovkach, A. Glatz, I. Aranson, and A. Snezhko. Emergence of self-organized multivortex states in flocks of active rollers. *Proceedings of the National Academy of Sciences*, 117(18):9706–9711, 2020.
- [90] Koohee Han, Gašper Kokot, Oleh Tovkach, Andreas Glatz, Igor S Aranson, and Alexey Snezhko. Emergence of self-organized multivortex states in flocks of active rollers. *Proceedings of the National Academy of Sciences*, 117(18):9706–9711, 2020.
- [91] M. Han, J. Yan, S. Granick, and E. Luijten. Effective temperature concept evaluated in an active colloid mixture. *Proceedings of the National Academy of Sciences*, 114(29):7513–7518, July 2017. Publisher: National Academy of Sciences Section: Physical Sciences.
- [92] M. Han, J. Yan, S. Granick, and E. Luijten. Effective temperature concept evaluated in an active colloid mixture. *Proceedings of the National Academy of Sciences*, 114(29):7513–7518, 2017.
- [93] J. Happel and H. Brenner. *Low Reynolds number hydrodynamics: with special applications to particulate media*, volume 1. Springer Science & Business Media, 2012.

- [94] Babak Vajdi Hokmabad, Akinori Nishide, Prashanth Ramesh, Carsten Krüger, and Corinna C Maass. Spontaneously rotating clusters of active droplets. *Soft matter*, 18(14):2731–2741, 2022.
- [95] Y. Hong, D. Velegol, N. Chaturvedi, and A. Sen. Biomimetic behavior of synthetic particles: From microscopic randomness to macroscopic control. *Physical Chemistry Chemical Physics*, 12:1423, 2010.
- [96] J. R. Howse, R. A. L. Jones, A. J. Ryan, T. Gough, R. Vafabakhsh, and R. Golestanian. Self-motile colloidal particles: From directed propulsion to random walk. *Physical Review Letters*, 99:048102, 2007.
- [97] Jonathan R Howse, Richard AL Jones, Anthony J Ryan, Tim Gough, Reza Vafabakhsh, and Ramin Golestanian. Self-motile colloidal particles: from directed propulsion to random walk. *Physical review letters*, 99(4):048102, 2007.
- [98] L. Huber, R. Suzuki, T. Krüger, E. Frey, and A. R. Bausch. Emergence of coexisting ordered states in active matter systems. *Science*, 361:255 – 258, 2018.
- [99] Y. Ibrahim, R. Golestanian, and T. B. Liverpool. Shape dependent phoretic propulsion of slender active particles. *Phys. Rev. Fluids*, 3:033101, 2018.
- [100] M.S. Ingber and L.A. Mondy. A numerical study of three-dimensional jeffery orbits in shear flow. *Journal of Rheology*, 38(6):1829–1843, 1994.
- [101] T. Ishikawa and M. Hota. Interaction of two swimming paramecia. *Journal of Experimental Biology*, 209(22):4452–4463, 2006.
- [102] T. Ishikawa and T.J. Pedley. Coherent structures in monolayers of swimming particles. *Physical Review Letters*, 100(8):088103, 2008.
- [103] T. Ishikawa, M. P. Simmonds, and T. J. Pedley. Hydrodynamic interaction of two swimming model micro-organisms. *J. Fluid Mech.*, 568:119–160, 2006.
- [104] K. Ishimoto. Guidance of microswimmers by wall and flow: Thigmotaxis and rheotaxis of unsteady squirmers in two and three dimensions. *Physical Review E*, 96(4):043103, 2017.
- [105] K. Ishimoto and E. A. Gaffney. Squirmer dynamics near a boundary. *Phys. Rev. E*, 88:062702, 2013.
- [106] R.E. Ismagilov, A. Schwartz, N. Bowden, and G.M. Whitesides. Autonomous movement and self-assembly. *Angewandte Chemie*, 114(4):674–676, 2002.
- [107] K. Jaideep, R. Poehnl, A. Sokolov, W. Uspal, and A. Snezhko. Arrested-motility states in populations of shape-anisotropic active janus particles. *Science Advances*, 8(26):eabo3604, 2022.

- [108] J.Deseigne, O. Dauchot, and H. Chaté. Collective motion of vibrated polar disks. *Physical review letters*, 105(9):098001, 2010.
- [109] G. Jeffery. The motion of ellipsoidal particles immersed in a viscous fluid. *Proceedings of the Royal Society of London. Series A, Containing papers of a mathematical and physical character*, 102(715):161–179, 1922.
- [110] D. Jin and L. Zhang. Collective behaviors of magnetic active matter: Recent progress toward reconfigurable, adaptive, and multifunctional swarming micro/nanorobots. *Accounts of Chemical Research*, 55(1):98–109, 2021.
- [111] J.Katuri, W.E. Uspal, J. Simmchen, A. Miguel-López, and S. Sánchez. Cross-stream migration of active particles. *Science Advances*, 4(1):eaao1755, 2018.
- [112] R. E. Johnson. An improved slender-body theory for stokes flow. *J. Fluid Mech.*, 99:411–431, 1980.
- [113] A. Kaiser, A. Snezhko, and I. Aranson. Flocking ferromagnetic colloids. *Science Advances*, 3(2):e1601469, February 2017. Publisher: American Association for the Advancement of Science Section: Research Article.
- [114] Andreas Kaiser, Alexey Snezhko, and Igor S Aranson. Flocking ferromagnetic colloids. *Science advances*, 3(2):e1601469, 2017.
- [115] H. Karani, G. Pradillo, and P. Vlahovska. Tuning the random walk of active colloids: From individual run-and-tumble to dynamic clustering. *Physical review letters*, 123(20):208002, 2019.
- [116] P. Katsamba, S. Michelin, and T. D. Montenegro-Johnson. Slender phoretic theory of chemically active filaments. *J. Fluid Mech.*, 898:A24, 2020.
- [117] J. Katuri, W. Uspal, J. Simmchen, A. Miguel-López, and S. Sánchez. Cross-stream migration of active particles. *Science Advances*, 4(1):eaao1755, January 2018.
- [118] J. Katuri, W. E. Uspal, J. Simmchen, A. Miguel-Lopez, and S. Sanchez. Cross-stream migration of active particles. *Sci. Adv.*, 4:eaao1755, 2018.
- [119] T. Kaya and H. Koser. Characterization of hydrodynamic surface interactions of escherichia coli cell bodies in shear flow. *Physical Review Letters*, 103:138103, Sep 2009.
- [120] T. Kaya and H. Koser. Direct upstream motility in escherichia coli. *Biophysical journal*, 102(7):1514–1523, 2012.
- [121] J. B. Keller and S. I. Rubinow. Slender-body theory for slow viscous flow. *J. Fluid Mech.*, 75:705–714, 1976.

- [122] M. S. Kilic and M. Z. Bazant. Induced-charge electrophoresis near a wall. *Electrophoresis*, 32:614–628, 2011.
- [123] K. Kim, J. Guo, Z. X. Liang, F. Q. Zhu, and D. L. Fan. Man-made rotary nanomotors: a review of recent developments. *Nanoscale*, 8:10471–10490, 2016.
- [124] M. Kim and T. R. Powers. Hydrodynamic interactions between rotating helices. *Phys. Rev. E*, 69:061910, 2004.
- [125] S. Kim and S. Karrila. *Microhydrodynamics: principles and selected applications*. Courier Corporation, 2013.
- [126] L. Koens and E. Lauga. The passive diffusion of *Leptospira interrogans*. *Phys. Biol.*, 11:066008, 2014.
- [127] L. Koens and E. Lauga. The boundary integral formulation of stokes flows includes slenderbody theory. *J. Fluid Mech.*, 850:R1, 2018.
- [128] G. Kokot and A. Snezhko. Manipulation of emergent vortices in swarms of magnetic rollers. *Nature Communications*, 9(1):2344, June 2018. Number: 1 Publisher: Nature Publishing Group.
- [129] C. Kreuter, U. Siems, P. Nielaba, P. Leiderer, and A. Erbe. Transport phenomena and dynamics of externally and self-propelled colloids in confined geometry. *The European Physical Journal Special Topics*, 222(11):2923–2939, 2013.
- [130] N. Kuznetsov, V. Maz’ya, and B. Vainberg. *Linear Water Waves: A Mathematical Approach*. Cambridge University Press, Cambridge, UK, 2004.
- [131] F. Kümmel, B. ten Hagen, R. Wittkowski, I. Buttinoni, R. Eichhorn, G. Volpe, H. Löwen, and C. Bechinger. Circular Motion of Asymmetric Self-Propelling Particles. *Physical Review Letters*, 110(19):198302, May 2013. Publisher: American Physical Society.
- [132] E. Lauga, W. DiLuzio, G. Whitesides, and H. Stone. Swimming in circles: motion of bacteria near solid boundaries. *Biophysical journal*, 90(2):400–412, 2006.
- [133] E. Lauga, W.R. Di Luzio, G. M. Whitesides, and H.A. Stone. Swimming in circles: Motion of bacteria near solid boundaries. *Biophys. J.*, 90:400 – 412, 2006.
- [134] E. Lauga and S. Michelin. Stresslets induced by active swimmers. *Physical Review Letters*, 117(14):148001, 2016.
- [135] E. Lauga and T. R. Powers. The hydrodynamics of swimming microorganisms. *Rep. Prog. Phys.*, 72:096601, 2009.
- [136] E. Lauga and T.R. Powers. The hydrodynamics of swimming microorganisms. *Reports on Progress in Physics*, 72(9):096601, 2009.

- [137] Eric Lauga. *The fluid dynamics of cell motility*, volume 62. Cambridge University Press, 2020.
- [138] Eric Lauga and Sébastien Michelin. Stresslets induced by active swimmers. *Phys. Rev. Lett.*, 117:148001, 2016.
- [139] F. Lavergne, H. Wendehenne, T. Bäuerle, and C. Bechinger. Group formation and cohesion of active particles with visual perception-dependent motility. *Science*, 364(6435):70–74, 2019.
- [140] A.M. Leshansky, O. Kenneth, O. Gat, and J.E. Avron. A frictionless microswimmer. *New Journal of Physics*, 9(5):145, 2007.
- [141] M. P. Lettinga, Z. Dogic, H. Wang, and J. Vermant. Flow behavior of colloidal rodlike viruses in the nematic phase. *Langmuir*, 21(17):8048–8057, 2005.
- [142] G.J. Li and A.M. Ardekani. Hydrodynamic interaction of microswimmers near a wall. *Physical Review E*, 90(1):013010, 2014.
- [143] B. Liebchen and H. Löwen. Synthetic Chemotaxis and Collective Behavior in Active Matter. *Accounts of Chemical Research*, 51(12):2982–2990, December 2018. Publisher: American Chemical Society.
- [144] M. J. Lighthill. *Commun. Pure Appl. Math.*, 5:109–118, 1952.
- [145] M.J. Lighthill. On the squirming motion of nearly spherical deformable bodies through liquids at very small reynolds numbers. *Communications on Pure and Applied Mathematics*, 5(2):109–118, 1952.
- [146] Maciej Lisicki, Shang Yik Reigh, and Eric Lauga. Autophoretic motion in three dimensions. *Soft Matter*, 14:3304–3314, 2018.
- [147] H. M. López, J. Gachelin, C. Douarche, H. Auradou, and E. Clément. Turning bacteria suspensions into superfluids. *Physical Review Letters*, 115:028301, 2015.
- [148] H.A. Lorentz. A general theorem concerning the motion of a viscous fluid and a few consequences derived from it. *Zittingsverslag van de Koninklijke Akademie van Wetenschappen te Amsterdam*, 5:168–175, 1896.
- [149] Vanesa Magar, Tomonobu Goto, and Timothy J Pedley. Nutrient uptake by a self-propelled steady squirmer. *The Quarterly Journal of Mechanics and Applied Mathematics*, 56(1):65–91, 2003.
- [150] C. Maggi, J. Simmchen, F. Saglimbeni, J. Katuri, M. Dipalo, F. De Angelis, S. Sánchez, and R. Di Leonardo. Self-Assembly of Micromachining Systems Powered by Janus Micromotors. *Small*, 12(4):446–451, 2016.

- [151] M. Makino and M. Doi. Separation of propeller-like particles by shear and electric field. *Phys. Rev. Fluids*, 2:064303, 2017.
- [152] Y. Man and E. Lauga. The wobbling-to-swimming transition of rotated helices. *Phys. Fluids*, 25:071904, 2013.
- [153] M. Marchetti, J. Joanny, S. Ramaswamy, T. Liverpool, J. Prost, M. Rao, and R. Simha. Hydrodynamics of soft active matter. *Reviews of Modern Physics*, 85(3):1143–1189, July 2013. Publisher: American Physical Society.
- [154] Marcos, H. C. Fu, T. R. Powers, and R. Stocker. Separation of microscale chiral objects by shear flow. *Phys. Rev. Lett.*, 102:158103, 2009.
- [155] A. Mathijssen, N. Figueroa-Morale, G. Junot, E. Clement, A. Lindner, and A. Zöttl. Oscillatory surface rheotaxis of swimming e. coli bacteria. *Nature Communications*, 10(1):3434, 2019.
- [156] E.M.F. Mauriello, T. Mignot, Z. Yang, and D.R. Zusman. Gliding motility revisited: how do the myxobacteria move without flagella? *Microbiology and Molecular Biology Reviews*, 74(2):229–249, 2010.
- [157] S. Michelin and E. Lauga. Phoretic self-propulsion at finite Peclet numbers. *Journal of Fluid Mechanics*, 747:572–604, 2014.
- [158] Sébastien Michelin and Eric Lauga. Optimal feeding is optimal swimming for all peclet numbers. *Physics of Fluids*, 23(10):101901, 2011.
- [159] Sébastien Michelin and Eric Lauga. Geometric tuning of self-propulsion for janus catalytic particles. *Scientific reports*, 7(1):1–9, 2017.
- [160] M. Miller and B. Bassler. Quorum Sensing in Bacteria. *Annual Review of Microbiology*, 55(1):165–199, October 2001. Publisher: Annual Reviews.
- [161] Y. Mirzae, B. Y. Rubinstein, K. I. Morozov, and A. M. Leshansky. Modeling propulsion of soft magnetic nanowires. *Front. Robot. AI*, 7:152, 2020.
- [162] P. Moon and D. Spencer. *Field theory handbook: including coordinate systems, differential equations and their solutions*. Springer, 2012.
- [163] P. Morse and H. Feshbach. Methods of theoretical physics. *American Journal of Physics*, 22(6):410–413, 1954.
- [164] B. Nasouri, A. Vilfan, and R. Golestanian. Minimum dissipation theorem for microswimmers. *Phys. Rev. Lett.*, 126:034503, 2021.
- [165] D. Nishiguchi and M. Sano. Mesoscopic turbulence and local order in Janus particles self-propelling under an ac electric field. *Physical Review E*, 92(5):052309, November 2015. Publisher: American Physical Society.

- [166] S Oren and I Frankel. Induced-charge electrophoresis of ideally polarizable particle pairs. *Physical Review Fluids*, 5(9):094201, 2020.
- [167] Zhenyu Ouyang, Zhaowu Lin, Jianzhong Lin, Zhaosheng Yu, and Nhan Phan-Thien. Cargo carrying with an inertial squirmer in a newtonian fluid. *Journal of Fluid Mechanics*, 959:A25, 2023.
- [168] G.A. Ozin, I. Manners, S. Fournier-Bidoz, and A. Arsenault. Dream nanomachines. *Advanced Materials*, 17(24):3011–3018, 2005.
- [169] O.S. Pak and E. Lauga. *J. Eng. Math.*, 88:1–28, 2014.
- [170] J. Palacci, S. Sacanna, A. Abramian, F. Barral, K. Hanson, A. Grosberg, D. Pine, and P. Chaikin. Artificial rheotaxis. *Science Advances*, 1(4):e1400214, May 2015. Publisher: American Association for the Advancement of Science Section: Research Article.
- [171] J. Palacci, S. Sacanna, A. Steinberg, D. Pine, and P. Chaikin. Living Crystals of Light-Activated Colloidal Surfers. *Science*, 339(6122):936–940, February 2013. Publisher: American Association for the Advancement of Science Section: Report.
- [172] Jeremie Palacci, Stefano Sacanna, Asher Preska Steinberg, David J Pine, and Paul M Chaikin. Living crystals of light-activated colloidal surfers. *Science*, 339(6122):936–940, 2013.
- [173] M. Palusa, J. de Graaf, A. Brown, and A. Morozov. Sedimentation of a rigid helix in viscous media. *Phys. Rev. Fluids*, 3:124301, 2018.
- [174] J. Park, J. M. Bricker, and J. E. Butler. Cross-stream migration in dilute solutions of rigid polymers undergoing rectilinear flow near a wall. *Physical Review E*, 76(4):040801, 2007.
- [175] D. Patra, S. Sengupta, W. Duan, H. Zhang, R. Pavlick, and A. Sen. Intelligent, self-powered, drug delivery systems. *Nanoscale*, 5(4):1273–1283, 2013.
- [176] W. F. Paxton, S. Sundararajan, T. E. Mallouk, and A. Sen. Chemical locomotion. *Angewandte Chemie International Edition*, 45:5420–5429, 2006.
- [177] W.F. Paxton, K.C. Kistler, C.C. Olmeda, A. Sen, S.K.St. Angelo, Y.Y. Cao, T.E. Mallouk, P.E. Lammert, and V.H. Crespi. Catalytic nanomotors: Autonomous movement of striped nanorods. *Journal of the American Chemical Society*, 126:13424, 2004.
- [178] T. Pedley, D. Brumley, and R. Goldstein. Squirmer with swirl: a model for volvox swimming. *Journal of fluid mechanics*, 798:165–186, 2016.
- [179] T. J. Pedley, D. R. Brumley, and R. E. Goldstein. Squirmer with swirl: a model for volvox swimming. *Journal of Fluid Mechanics*, 798:165–186, 2016.

- [180] T.J. Pedley and J.O. Kessler. Hydrodynamic phenomena in suspensions of swimming microorganisms. *Annual Review of Fluid Mechanics*, 24(1):313–358, 1992.
- [181] C. Peng, I. Lazo, S. Shiyanovskii, and O. Lavrentovich. Induced-charge electro-osmosis around metal and Janus spheres in water: Patterns of flow and breaking symmetries. *Physical Review E*, 90(5):051002, November 2014. Publisher: American Physical Society.
- [182] C. Peng, I. Lazo, S. V. Shiyanovskii, and O. D. Lavrentovich. Induced-charge electro-osmosis around metal and janus spheres in water: Patterns of flow and breaking symmetries. *Phys. Rev. E*, 90:051002(R), 2014.
- [183] F. Peruani, J. Starruß, V. Jakovljevic, L. Søgaaard-Andersen, A. Deutsch, and M. Bär. Collective motion and nonequilibrium cluster formation in colonies of gliding bacteria. *Physical review letters*, 108(9):098102, 2012.
- [184] K. E. Peyer, S. Tottori, F. Qiu, L. Zhang, and B. J. Nelson. Magnetic helical micromachines. *Chem. Eur. J.*, 19:28–38, 2013.
- [185] F. Piazza and D. Grebenkov. Diffusion-influenced reactions on non-spherical partially absorbing axisymmetric surfaces. *Physical Chemistry Chemical Physics*, 21:25896–25906, 2019.
- [186] R. Poehnl, M. Popescu, and W. Uspal. Axisymmetric spheroidal squirmers and self-diffusiophoretic particles. *Journal of Physics: Condensed Matter*, 32(16):164001, 2020.
- [187] R. Poehnl and W. Uspal. Phoretic self-propulsion of helical active particles. *Journal of Fluid Mechanics*, 927:A46, 2021.
- [188] Ruben Poehnl and William Uspal. Phoretic self-propulsion of helical active particles. *Journal of Fluid Mechanics*, 927:A46, 2021.
- [189] O. Pohl and H. Stark. Dynamic clustering and chemotactic collapse of self-phoretic active particles. *Physical review letters*, 112(23):238303, 2014.
- [190] Oliver Pohl and Holger Stark. Dynamic clustering and chemotactic collapse of self-phoretic active particles. *Phys. Rev. Lett.*, 112:238303, Jun 2014.
- [191] R. Pöhl, M. N. Popescu, and W. E. Uspal. Axisymmetric spheroidal squirmers and self-diffusiophoretic particles. *J. Phys.: Condens. Matter*, 32:164001, 2020.
- [192] M. N. Popescu, W. E. Uspal, C. Bechinger, and P. Fischer. Chemotaxis of active janus nanoparticles. *Nano Lett.*, 18:5345–5349, 2018.
- [193] M. N. Popescu, W. E. Uspal, Z. Eskandari, M. Tasinkevych, and S. Dietrich. Effective squirmer models for self-phoretic chemically active spherical colloids. *Eur. Phys. J. E*, 41:145, 2018.

- [194] M. N. Popescu, W. E. Uspal, Z. Eskandari, M. Tasinkevych, and S. Dietrich. Effective squirmer models for self-phoretic chemically active spherical colloids. *European Physical Journal E*, 41:145, 2018.
- [195] Mihail N Popescu, William E Uspal, Clemens Bechinger, and Peer Fischer. Chemotaxis of active janus nanoparticles. *Nano letters*, 18(9):5345–5349, 2018.
- [196] M.N. Popescu, S. Dietrich, M. Tasinkevych, and J. Ralston. Phoretic motion of spheroidal particles due to self-generated solute gradients. *The European Physical Journal E*, 31(4):351–367, 2010.
- [197] C. Pozrikidis. *Boundary Integral and Singularity Methods for Linearized Viscous Flow*. Cambridge University Press, Cambridge, UK, 1992.
- [198] C. Pozrikidis. *A practical guide to boundary element methods with the software library BEMLIB*. CRC Press, 2002.
- [199] C. Pozrikidis. *A Practical Guide to Boundary Element Methods with the Software Library BEMLIB*. CRC Press, Boca Raton, 2002.
- [200] E. M. Purcell. Life at low reynolds number. *Am. J. Physics*, 45:3, 1977.
- [201] E. M. Purcell. The efficiency of propulsion by a rotating flagellum. *Proc. Natl. Acad. Sci.*, 94:11307–11311, 1997.
- [202] G. Redner, A. Baskaran, and M. Hagan. Reentrant phase behavior in active colloids with attraction. *Physical Review E*, 88(1):012305, 2013.
- [203] M. Reichert and H. Stark. Synchronization of rotating helices by hydrodynamic interactions. *Eur. Phys. J. E*, 17:493–500, 2005.
- [204] C Reichhardt and O. Reichhardt. Active matter transport and jamming on disordered landscapes. *Physical Review E*, 90(1):012701, 2014.
- [205] C. Reichhardt and O. Reichhardt. Active microrheology in active matter systems: Mobility, intermittency, and avalanches. *Physical Review E*, 91(3):032313, 2015.
- [206] L. Ren, D. Zhou, Z. Mao, P. Xu, T.J. Huang, and T.E. Mallouk. Rheotaxis of bimetallic micromotors driven by chemical–acoustic hybrid power. *American Chemical Society Nano*, 11(10):10591–10598, 2017.
- [207] B. Rodenborn, C.-H. Chen, H. L. Swinney, B. Liu, and H. P. Zhang. Propulsion of microorganisms by a helical flagellum. *Proc. Natl. Acad. Sci.*, 110:E338–E347, 2013.
- [208] L. Rothschild. Non-random distribution of bull spermatozoa in a drop of sperm suspension. *Nature*, 198(488):1221, 1963.
- [209] D. Saintillan. Rheology of active fluids. *Ann. Rev. Fluid Mech.*, 50:563–92, 2017.

- [210] D. Saintillan. Rheology of active fluids. *Annual Review of Fluid Mechanics*, 50:563–592, 2018.
- [211] D. Saintillan and M. Shelley. Active suspensions and their nonlinear models. *Comptes Rendus Physique*, 14:497, 2013.
- [212] D. Saintillan and M. J. Shelley. *Comptes Rendus Physique*, 14:497 – 517, 2013.
- [213] S. Sanchez, L. Soler, and J. Katuri. Chemically Powered Micro- and Nanomotors. *Angewandte Chemie International Edition*, 54(5):1414–1444, 2015.
- [214] T. Sanchez, D. Chen, S. DeCamp, M. Heymann, and Z. Dogic. Spontaneous motion in hierarchically assembled active matter. *Nature*, 491(7424):431–434, 2012.
- [215] Tim Sanchez, Daniel TN Chen, Stephen J DeCamp, Michael Heymann, and Zvonimir Dogic. Spontaneous motion in hierarchically assembled active matter. *Nature*, 491(7424):431–434, 2012.
- [216] L. Schmieding, E. Lauga, and T. Montenegro-Johnson. Autophoretic flow on a torus. *Physical Review Fluids*, 2(3):034201, 2017.
- [217] O. Schnitzer and E. Yariv. Osmotic self-propulsion of slender particles. *Phys. Fluids*, 27:031701, 2015.
- [218] Priyanka Sharan, Charlie Maslen, Berk Altunkeyik, Ivan Rehor, Juliane Simmchen, and Thomas D Montenegro-Johnson. Fundamental modes of swimming correspond to fundamental modes of shape: Engineering i-, u-, and s-shaped swimmers. *Advanced Intelligent Systems*, 3(11):2100068, 2021.
- [219] C. Shen, Z. Jiang, L. Li, J. Gilchrist, and D. Ou-Yang. Frequency response of induced-charge electrophoretic metallic janus particles. *Micromachines*, 11(3):334, 2020.
- [220] J. Simmchen, J. Katuri, W. Uspal, M. Popescu, M. Tasinkevych, and S. Sanchez. Topographical pathways guide chemical microswimmers. *Nat. Commun.*, 7:10598, 2016.
- [221] J. Simmchen, J. Katuri, W.E. Uspal, M.N. Popescu, M. Tasinkevych, and S. Sánchez. Topographical pathways guide chemical microswimmers. *Nature Communications*, 7:10598, 2016.
- [222] A. Sokolov and I. Aranson. Physical Properties of Collective Motion in Suspensions of Bacteria. *Physical Review Letters*, 109(24):248109, December 2012. Publisher: American Physical Society.
- [223] L. Soler and S. Sánchez. Catalytic nanomotors for environmental monitoring and water remediation. *Nanoscale*, 6(13):7175–7182, 2014.

- [224] T.M. Sonneborn. Methods in paramecium research. In *Methods in cell biology*, volume 4, pages 241–339. Elsevier, 1970.
- [225] S.E. Spagnolie and E. Lauga. Hydrodynamics of self-propulsion near a boundary: predictions and accuracy of far-field approximations. *Journal of Fluid Mechanics*, 700:105–147, 2012.
- [226] T. M. Squires and M. Z. Bazant. Breaking symmetries in induced-charge electro-osmosis and electrophoresis. *J. Fluid Mech.*, 560:65–101, 2006.
- [227] Howard A. Stone and Aravinthan D. T. Samuel. Propulsion of microorganisms by surface distortions. *Phys. Rev. Lett.*, 77:4102–4104, 1996.
- [228] S. Sundararajan, P. E. Lammert, A. W. Zudans, V. H. Crespi, and A. Sen. Catalytic motors for transport of colloidal cargo. *Nano letters*, 8(5):1271–1276, 2008.
- [229] J Tailleur and M Cates. Statistical mechanics of interacting run-and-tumble bacteria. *Physical review letters*, 100(21):218103, 2008.
- [230] B. ten Hagen, F. Kümmel, R. Wittkowski, D. Takagi, H. Löwen, and C. Bechinger. Gravitaxis of asymmetric self-propelled colloidal particles. *Nature Communications*, 5(1):1–7, September 2014. Number: 1 Publisher: Nature Publishing Group.
- [231] M. Theers, E. Westphal, G. Gompper, and R.G. Winkler. Modeling a spheroidal microswimmer and cooperative swimming in a narrow slit. *Soft Matter*, 12(35):7372–7385, 2016.
- [232] M. Theers, E. Westphal, K. Qi, R. G. Winkler, and G. Gompper. Clustering of microswimmers: interplay of shape and hydrodynamics. *Soft Matter*, 14:8590–8603, 2018.
- [233] Mario Theers, Elmar Westphal, Gerhard Gompper, and Roland G. Winkler. Modeling a spheroidal microswimmer and cooperative swimming in a narrow slit. *Soft Matter*, 12:7372–7385, 2016.
- [234] I. Theurkauff, C. Cottin-Bizonne, J. Palacci, C. Ybert, and L. Bocquet. Dynamic clustering in active colloidal suspensions with chemical signaling. *Physical review letters*, 108(26):268303, 2012.
- [235] B.J. Trevelyan and S.G. Mason. Particle motions in sheared suspensions. i. rotations. *Journal of Colloid Science*, 6(4):354–367, 1951.
- [236] W. E. Usual. The boundary element method for fluctuating active colloids. In A. S. Kim, editor, *Non-Equilibrium Particle Dynamics*. InTechOpen, 2019.
- [237] W. E. Usual. Theory of light-activated catalytic janus particles. *J. Chem. Phys.*, 150:114903, 2019.

- [238] W. E. Uspal, H. B. Eral, and P. S. Doyle. Engineering particle trajectories in microfluidic flows using particle shape. *Nature Communications*, 4:2666, 2013.
- [239] W. E. Uspal, M. N. Popescu, S. Dietrich, and M. Tasinkevych. Self-propulsion of a catalytically active particle near a planar wall: from reflection to sliding and hovering. *Soft Matter*, 11:434–438, 2015.
- [240] W.E. Uspal, M.N. Popescu, S. Dietrich, and M. Tasinkevych. Rheotaxis of spherical active particles near a planar wall. *Soft Matter*, 11(33):6613–6632, 2015.
- [241] W.E. Uspal, M.N. Popescu, S. Dietrich, and M. Tasinkevych. Self-propulsion of a catalytically active particle near a planar wall: from reflection to sliding and hovering. *Soft Matter*, 11:434–438, 2015.
- [242] W.E. Uspal, M.N. Popescu, S. Dietrich, and M. Tasinkevych. Self-propulsion of a catalytically active particle near a planar wall: from reflection to sliding and hovering. *Soft Matter*, 11:434–438, 2015.
- [243] P. J. Vach, D. Walker, P. Fischer, P. Fratzl, and D. Faivre. Pattern formation and collective effects in populations of magnetic microswimmers. *Journal of Physics D*, 50:11LT03, 2017.
- [244] T. Vicsek, A. Czirók, E. Ben-Jacob, I. Cohen, and O. Shochet. Novel Type of Phase Transition in a System of Self-Driven Particles. *Physical Review Letters*, 75(6):1226–1229, August 1995. Publisher: American Physical Society.
- [245] G. Volpe, I. Buttinoni, D. Vogt, H.J. Kümmerer, and C. Bechinger. Microswimmers in patterned environments. *Soft Matter*, 7(19):8810–8815, 2011.
- [246] S. Wang and A. Ardekani. Inertial squirmer. *Physics of Fluids*, 24(10):101902, 2012.
- [247] Yang Wang, Rose M Hernandez, David J Bartlett, Julia M Bingham, Timothy R Kline, Ayusman Sen, and Thomas E Mallouk. Bipolar electrochemical mechanism for the propulsion of catalytic nanomotors in hydrogen peroxide solutions. *Langmuir*, 22(25):10451–10456, 2006.
- [248] Z. Wang, Z. Wang, J. Li, C. Tian, and Y. Wang. Active colloidal molecules assembled via selective and directional bonds. *Nature communications*, 11(1):1–12, 2020.
- [249] H. H. Wensink, J. Dunkel, S. Heidenreich, K. Drescher, R. E. Goldstein, H. Löwen, and J. M. Yeomans. Meso-scale turbulence in living fluids. *Proceedings of the National Academy of Sciences of the United States of America*, 109(36):14308–14313, 2012.
- [250] H.H. Wensink, J. Dunkel, S. Heidenreich, K. Drescher, R.E. Goldstein, H. Löwen, and J.M. Yeomans. Meso-scale turbulence in living fluids. *Proceedings of the National Academy of Sciences*, 109(36):14308–14313, 2012.

- [251] H. Wioland, E. Lushi, and R. E. Goldstein. Directed collective motion of bacteria under channel confinement. *New Journal of Physics*, 18:075002, 2016.
- [252] R. Wittkowski and H. Löwen. Self-propelled brownian spinning top: Dynamics of a biaxial swimmer at low reynolds numbers. *Phys. Rev. E*, 85:021406, 2012.
- [253] F. G. Woodhouse and R. E. Goldstein. Spontaneous circulation of confined active suspensions. *Physical Review Letters*, 109:168105, 2012.
- [254] K.-T. Wu, J. B. Hishamunda, D. T. N. Chen, S. J. DeCamp, Y.-W. Chang, A. Fernández-Nieves, S. Fraden, and Z. Dogic. Transition from turbulent to coherent flows in confined three-dimensional active fluids. *Science*, 355, 2017.
- [255] J. Yan, M. Han, J. Zhang, C. Xu, E. Luijten, and S. Granick. Reconfiguring active particles by electrostatic imbalance. *Nature Materials*, 15(10):1095–1099, October 2016. Number: 10 Publisher: Nature Publishing Group.
- [256] Jing Yan, Ming Han, Jie Zhang, Cong Xu, Erik Luijten, and Steve Granick. Reconfiguring active particles by electrostatic imbalance. *Nature materials*, 15(10):1095–1099, 2016.
- [257] E. Yariv. Self-diffusiophoresis of slender catalytic colloids. *Langmuir*, 36:6903–6915, 2020.
- [258] Ehud Yariv. Self-diffusiophoresis of slender catalytic colloids. *Langmuir*, 36(25):6903–6915, 2019.
- [259] Y. R. Yu, F. F. Fu, L. R. Shang, Y. Cheng, Z. Z. Gu, and Y. J. Zhao. Bioinspired helical microfibers from microfluidics. *Adv. Mater.*, 29:1605765, 2017.
- [260] Arne W Zantop and Holger Stark. Emergent collective dynamics of pusher and puller squirmer rods: swarming, clustering, and turbulence. *Soft Matter*, 18(33):6179–6191, 2022.
- [261] B. Zhang, A. Sokolov, and A. Snezhko. Reconfigurable emergent patterns in active chiral fluids. *Nature Communications*, 11(1):1–9, September 2020. Number: 1 Publisher: Nature Publishing Group.
- [262] J. Zhang, R. Alert, J. Yan, N. Wingreen, and S. Granick. Active phase separation by turning towards regions of higher density. *Nat. Phys.*, 17, 2021.
- [263] P. Zhang, S. Jana, M. Giarra, PP. Vlachos, and S. Jung. Paramecia swimming in viscous flow. *The European Physical Journal Special Topics*, 224(17-18):3199–3210, 2015.
- [264] L. Zhu, E. Lauga, and L. Brandt. Self-propulsion in viscoelastic fluids: Pushers vs. pullers. *Physics of Fluids*, 24(5):051902, 2012.

- [265] A. Zöttl and H. Stark. Hydrodynamics determines collective motion and phase behavior of active colloids in quasi-two-dimensional confinement. *Physical Review Letters*, 112(11):118101, 2014.